VIBRATION-BASED DAMAGE DETECTION FOR TIMBER BRIDGES

A Thesis Submitted to the College of

Graduate Studies and Research

in Partial Fulfillment of the Requirements

for the Degree of Master of Science

in the Department of Civil Engineering

University of Saskatchewan

Saskatoon, Canada

By

Cameron Jonathan Beauregard

PERMISSION TO USE

In presenting this thesis/dissertation in partial fulfillment of the requirements for a Postgraduate degree from the University of Saskatchewan, I agree that the Libraries of this University may make it freely available for inspection. I further agree that permission for copying of this thesis/dissertation in any manner, in whole or in part, for scholarly purposes may be granted by the professor or professors who supervised my thesis/dissertation work or, in their absence, by the Head of the Department or the Dean of the College in which my thesis work was done. It is understood that any copying or publication or use of this thesis/dissertation or parts thereof for financial gain shall not be allowed without my written permission. It is also understood that due recognition shall be given to me and to the University of Saskatchewan in any scholarly use which may be made of any material in my thesis/dissertation.

Requests for permission to copy or to make other uses of materials in this thesis/dissertation in whole or part should be addressed to:

Head of the Department of Civil Engineering

University of Saskatchewan

57 Campus Drive

Saskatoon, Saskatchewan, S7N 5A9

Canada

ABSTRACT

Vibration-based damage detection (VBDD) methods are global response-based methods that have the potential to provide valuable insight into the health of a structure. Dynamic characteristics obtained through vibration testing, such as the natural frequencies and their associated mode shapes, are directly related to both the stiffness and the mass of the structure, which are both good indicators of damage. In a typical application of VBDD methods, the vibration characteristics are obtained periodically to detect small changes in the response, indicating damage over time. However, this thesis considers using a snapshot of the vibration signature based on a single set of measurements to detect specific types of damage by comparing the response with that of other similar structures with known condition states.

Like many provinces, Saskatchewan currently has a large inventory of aging timber bridges that are at or nearing the end of their service life. Many of these bridges are experiencing decay of their substructure elements (piles, pile caps and abutments), yet these are not always accessible for the inspector to identify. Furthermore, current inspection methods require lengthy and thorough site visits to reliably assess the condition of the timber bridge. Given the length of the current inspection methods and the large inventory of timber bridges in the Saskatchewan road network, other assessment tools are being sought.

The objective of this thesis was to examine the feasibility of using vibration-based methods to assess the structural integrity of short-to-medium span timber bridges. Specifically, this thesis investigates the influence of realistic substructure stiffness on the dynamic properties of a timber bridge. Further research was conducted to determine if substructure deterioration could be detected reliably using the response from a single vibration test without the benefit of baseline (prior to damage condition) data.

Additional variables, such as superstructure damage, superimposed mass on the timber bridge (to simulate the wearing surface), and interactions between the substructure/superstructure, were considered in this thesis. Furthermore, practical applications were studied, which included using limited sensors and impact excitation, as well as a study that used pattern recognition techniques in conjunction with a database of vibration signatures from various substructure condition states to assess the health of a timber bridge's substructure.

It was concluded that the first flexural mode shape could be described by deconstructing the mode shape into superstructure and substructure components. Based on the relative amplitudes of these components, differential and uniform support movements were used to describe the stiffness of the substructure. Additionally, a limited pattern recognition study, using neural networks, classified the integrity of timber bridge substructures on the basis of a single measurement of the bridge's vibration signature.

Variables such as superstructure damage, superimposed mass, and excitation type had relatively little influence on the results reported in this thesis. Furthermore, it was found

that substructure and superstructure damage could be detected independently; however, superstructure damage detection required a baseline response.

ACKNOWLEDGEMENTS

I would like to express my gratitude to my supervisors, Dr. Bruce Sparling and Dr. Leon Wegner, for their continual encouragement and guidance throughout the assembly of my thesis. Your support and feedback have, undoubtedly, given me the motivation to overcome the struggles of this undertaking.

I would also like to thank Saskatchewan Ministry of Highways and Infrastructure, as well as the Natural Sciences and Engineering Research Council of Canada for their financial support to complete this thesis. Additionally, I would like to thank the University of Saskatchewan and Dr. Mel Hosain for their support through scholarships.

I acknowledge the help provided by my committee members, Drs. Jit Sharma, Doug Milne, Lisa Feldman, and Mohamed Boulfiza, as well as the external examiner, Mark Gress. Their feedback has greatly helped in the assembly of the thesis.

I would also like to acknowledge the assistance of Brennan Pokoyoway and Dale Pavier, University of Saskatchewan Structures Laboratory technicians. I am also thankful for all the other graduate students that helped me with my project, either directly with the research, or indirectly with much needed distractions.

Finally, I would like to extend my gratitude to my family, friends, and my wife, Danae, for the constant love and support. I am continuously grateful that I have been surrounded by such amazing people.

TABLE OF CONTENTS

PERMISSION TO USE i

ABSTRACT ii

ACKNOWLEDGEMENTS v

TABLE OF CONTENTS vi

LIST OF TABLES xii

LIST OF FIGURES xvi

LIST OF SYMBOLS xxii

LIST OF ABBREVIATIONS xxiv

1. INTRODUCTION 1

1.1. BACKGROUND 1

1.2. OBJECTIVES 3

1.3. SCOPE AND METHODOLOGY 4

1.4. LAYOUT OF THESIS 5

2. LITERATURE REVIEW 7

2.1. INTRODUCTION 7

2.2. TIMBER BRIDGES 7

2.2.1. Timber Characteristics 7
2.2.2. Saskatchewan Timber Bridges 10
2.3. VIBRATION-BASED DAMAGE DETECTION 11
2.3.1. Overview 11
2.3.2. VBDD Techniques 12
2.3.3. VBDD Research at the University of Saskatchewan 15
2.3.4. VBDD with Timber 16
2.3.5. Further VBDD on Substructures 20
3. DESCRIPTION OF EXPERIMENTAL STUDY 21
3.1. INTRODUCTION 21
3.2. TIMBER BRIDGE 21
3.3. EXCITATION 24
3.3.1. Overview 24
3.3.2. Impact 24
3.3.3. Hydraulic Shaker 25
3.3.4. Summary 26
3.4. ACCELEROMETERS 26
3.5. DATA PROCESSING AND TESTING PROTOCOL 29
3.5.1. Overview 29
3.5.2. Data Acquisition 29

3.5.3. Signal Processing 30
3.6. PRELIMINARY TESTS TO DEFINE TEST PROTOCOLS 34
3.6.1. Overview 34
3.6.2. Interference Between Lower Modes 34
3.6.3. Methods for Accentuating the First Flexural Mode 36
3.7. DAMAGE CASES CONSIDERED 38
3.7.1. Overview 38
3.7.2. Determination of Substructure Stiffness 39
3.7.3. Substructure Damage Cases 47
3.7.4. Weight Cases 48
3.7.5. Superstructure Damage Cases 50
3.8. SUMMARY OF THE EXPERIMENTAL PROGRAM 51
3.8.1. Overview 51
3.8.2. Substructure Damage Program 53
3.8.3. Weight Case program 53
3.8.4. Substructure and Superstructure Interaction Program 53
4. TIMBER BRIDGE DAMAGE DECTECTION RESULTS 54
4.1. INTRODUCTION 54
4.2. BRIDGE BEHAVIOUR 54
4.2.1. Overview 54

4.2.2. Dynamic Response 55
4.2.3. Normalization 59
4.2.4. Mode Shape Variability 63
4.2.5. Mode Shape Components 65
4.2.6. Summary 68
4.3. DETECTION OF SUBSTRUCTURE DAMAGE TO A SINGLE SUPPORT 68
4.3.1. Overview 68
4.3.2. Uniform Substructure Deterioration 69
4.3.3. Local Substructure Deterioration 72
4.3.4. Quantitative Analysis with Mode Shape Components 74
4.3.5. Effect of Excitation 77
4.3.6. Natural Frequency 80
4.3.7. Summary 82
4.4. SUBSTRUCTURE DAMAGE DETECTION ON BOTH SUPPORTS 82
4.4.1. Overview 82
4.4.2. Results and Discussion 83
4.4.3. Summary 85
4.5. INFLUENCE OF SUPERIMPOSED MASS 85
4.5.1. Overview 85
4.5.2. Results and Discussion 86

4.5.3. Summary 88
4.6. SUPERSTRUCTURE DAMAGE DETECTION 89
4.6.1. Overview 89
4.6.2. Superstructure Damage Detection 89
4.6.3. Substructure and Superstructure Interactions 92
4.6.4. Summary 99
4.7. PRACTICAL APPLICATION 99
4.7.1. Overview 99
4.7.2. Results and Discussion 100
4.7.3. Summary 104
5. PATTERN RECOGNITION USING NEURAL NETWORKS 105
5.1. OVERVIEW 105
5.2. BACKGROUND 105
5.3. EXPERIMENTAL PROGRAM 107
5.4. RESULTS 110
5.5. CONCLUSION 112
6. CONCLUSIONS AND RECOMMENDATIONS 113
6.1. SUMMARY 113
6.2. CONCLUSIONS 114
6.3. RECOMMENDATIONS AND FUTURE RESEARCH 117

REFERENCES 118

APPENDIX A. SIGNAL PROCESSING 125

APPENDIX B. OBTAINING SUBSTRUCTURE STIFFNESS 129

APPENDIX C. NORMALIZED MODE SHAPES 131

APPENDIX D. MODE SHAPE COMPONENTS 139

APPENDIX E. NATURAL FREQUENCIES 146

APPENDIX F. VIBRATION-BASED DAMAGE DETECTION 148

APPENDIX G. STATISTICAL ANALYSIS 154

LIST OF TABLES

Table 3.1. Excitation methods 26

Table 3.2. Definition of the three accelerometer configurations 28

Table 3.3. Foundation stiffness window (per pile) 44

Table 3.4. Substructure condition states 47

Table 3.5. Summary of the weight cases considered 50

Table 3.6. Superstructure condition states 51

Table 4.1. Change in mode shape components relative to the base foundation case ($D0S0W1_a$) for multiple foundation cases, using two excitation methods 79

Table 4.2. Fundamental frequency of the bridge for different softening cases under a single support. 81

Table 4.3. Fundamental frequency of the bridge for cases with damage to both supports 84

Table 4.4. Effect of weight on the fundamental frequency 88

Table 4.5. Change in mode shape components relative to the base foundation case (D0S0W1a), for impact loading considering 22 sensors vs. 12 sensors 103

Table 5.1. Mode shape component data used to train the model 109

Table 5.2. Mode shape component data used to test the model 109

Table A.1. Acceleration calibration factors from different dates 126

Table B.1. Summary of stiffness of pile below ground stiffness, k_s 130

Table C.1. Unit-norm mode shape for D0S0W1$_a$ from harmonic and impact excitation 132
Table C.2. Unit-norm mode shape for D1S0W1 from harmonic and impact excitation 132
Table C.3. Unit-norm mode shape for D2S0W1 from harmonic and impact excitation 132
Table C.4. Unit-norm mode shape for D3S0W1 from harmonic and impact excitation 133
Table C.5. Unit-norm mode shape for D0S0W1$_b$ from harmonic and impact excitation 133
Table C.6. Unit-norm mode shape for D0S0W2 from harmonic and impact excitation 133
Table C.7. Unit-norm mode shape for D4S0W1$_a$ from harmonic and impact excitation 134
Table C.8. Unit-norm mode shape for D4S0W2 from harmonic and impact excitation 134
Table C.9. Unit-norm mode shape for D0S0W1$_c$ from harmonic and impact excitation 134
Table C.10. Unit-norm mode shape for D4S0W1$_b$ from harmonic and impact excitation 135
Table C.11. Unit-norm mode shape for D5S0W1 from harmonic and impact excitation 135
Table C.12. Unit-norm mode shape for D6S0W1 from harmonic and impact excitation 135
Table C.13. Unit-norm mode shape for D0S1W1 from harmonic and impact excitation 136
Table C.14. Unit-norm mode shape for D4S1W1 from harmonic and impact excitation 136

Table C.15. Unit-norm mode shape for D5S1W1 from harmonic and impact excitation 136
Table C.16. Unit-norm mode shape for D6S1W1 from harmonic and impact excitation 137
Table C.17. Unit-norm mode shape for D0S2W1 from harmonic and impact excitation 137
Table C.18. Unit-norm mode shape for D4S2W1 from harmonic and impact excitation 137
Table C.19. Unit-norm mode shape for D5S2W1 from harmonic and impact excitation 138
Table C.20. Unit-norm mode shape for D6S2W1 from harmonic and impact excitation 138
Table D.1. Summary of average mode shape components from harmonic excitation 140
Table D.2. Summary of average mode shape components from impact excitation..... 143
Table E.1. Summary of all natural frequencies for timber bridge condition states..... 147
Table F.1. Area under the change in mode shape plots when comparing similar superstructure states to establish a threshold..... 153
Table F.2. Area under the change in curvature plots when comparing similar superstructure states to establish a threshold..... 153
Table G.1. T-test results considering bridge states with varying substructure stiffness under a single support 155
Table G.2. F-test on variance results considering bridge states with varying substructure stiffness under a single support 156

Table G.3. T-test results considering bridge states with varying substructure stiffness under both supports 157
Table G.4. T-test results considering bridge states with varying substructure stiffness and superimposed mass 158
Table G.5. T-test results considering bridge states with similar substructure stiffness (D0) and varying superstructure states 159
Table G.6. T-test results considering bridge states with similar substructure stiffness (D4) and varying superstructure states 159
Table G.7. T-test results considering bridge states with similar substructure stiffness (D5) and varying superstructure states 160
Table G.8. T-test results considering bridge states with similar substructure stiffness (D0) and varying superstructure states 160
Table G.9. T-test results considering bridge states with varying substructure stiffness and varying superstructure states 161
Table G.10. T-test results considering bridge states with varying substructure stiffness under a single support using the limited accelerometer configuration 162

LIST OF FIGURES

Figure 1.1. Timber bridge (courtesy of Yang Sun) 1

Figure 1.2. A timber substructure (courtesy of Stantec Inc.) 2

Figure 2.1. Diagram showing where decay is most likely to occur on a timber bridge (after Ritter 1990; RTA 2008; Muchmore 1986) 9

Figure 3.1. The timber bridge in the laboratory 22

Figure 3.2. Plan view and cross-section of the timber bridge (dimensions in mm) 23

Figure 3.3. The hydraulic shaker on the timber bridge 25

Figure 3.4. Accelerometer 27

Figure 3.5. Plan view of the bridge deck, showing the location of accelerometers and excitation (dimensions in mm) 28

Figure 3.6. Data processing flow chart 32

Figure 3.7. Comparison of the first torsional and first flexural mode shapes of the bare bridge 35

Figure 3.8. Partial frequency spectrum for the reference accelerometer obtained using impact excitation, showing the closely spaced flexural and torsional modes 36

Figure 3.9. Partial frequency spectrum for the reference accelerometer obtained using impact excitation after the torsional mode was suppressed 38

Figure 3.10. Effective stiffness model by considering the soil-pile interaction of an embedded timber pile 39

Figure 3.11 Typical applied load vs. average axial deflection behaviour for a timber pile with highlighted low and high load pile stiffness (after Donovan 2004) 41
Figure 3.12. Low load pile stiffness vs. high load pile stiffness, showing a range of above ground pile stiffness, k_p (data from Donavan 2004) 42
Figure 3.13. Range of soil-pile system stiffness below ground, k_s 43
Figure 3.14. Wood block support setup (front and side views) 44
Figure 3.15. Test setup to determine support stiffness 45
Figure 3.16. Pine and oak block foundation load deflection curve (per support) 46
Figure 3.17. Plan view of the deck, showing the distribution of concrete blocks used to produce the two weight cases 49
Figure 3.18. Timber bridge loaded with Weight Case 1 (W1) 50
Figure 3.19. Summary of experimental program 52
Figure 4.1. Frequency spectrum of the reference accelerometer for foundation case **D0**S0W1$_a$ using impact loading 55
Figure 4.2. First flexural mode shape for foundation case **D0**S0W1$_a$, obtained using impact loading 56
Figure 4.3. First flexural mode shape for foundation case **D1**S0W1, obtained using impact loading 57
Figure 4.4. First flexural mode shape for foundation case **D2**S0W1, obtained using impact loading 57
Figure 4.5. Acceleration spectra showing the first flexural and torsional natural frequencies under different damage states 58

Figure 4.6. Representations of the same mode shape using the (a) bridge- and (b) girder-normalization schemes (generated using pseudo data) 61
Figure 4.7. Bridge-normalized representation of the soft foundation case (**D2**S0W1)... 62
Figure 4.8. Girder-normalized representation of the soft foundation case (**D2**S0W1) ... 62
Figure 4.9. Variability of mode shape amplitudes for the base support case (D0) using harmonic excitation 64
Figure 4.10. Variability of mode shape amplitudes for the base support case (D0) using impact excitation 64
Figure 4.11. Mode shape of Girder 1 for foundation case **D0**S0W1 (harmonic excitation), subdivided into its three components 66
Figure 4.12. Mode shape of Girder 1 for foundation case **D1**S0W1 (harmonic excitation), subdivided into its three components 66
Figure 4.13. Mode shape of Girder 1 for foundation case **D2**S0W1 (harmonic excitation), subdivided into its three components 67
Figure 4.14. Mode shape components along each girder for girder-normalized data from harmonic excitation (rigid foundation case **D0**S0W1$_a$) 71
Figure 4.15. Mode shape components along each girder for girder-normalized data from harmonic excitation (hard foundation case **D1**S0W1) 71
Figure 4.16. Mode shape components along each girder for girder-normalized data from harmonic excitation (soft foundation case **D2**S0W1) 72
Figure 4.17. Partial frequency spectrum for the reference accelerometer for foundation case **D3**S0W1, showing the first torsional and flexural natural frequency separation 73

Figure 4.18. Mode shape components for girder-normalized data from harmonic excitation (D3) 73
Figure 4.19. Mode shape components for bridge-normalized data from harmonic excitation (D3) 74
Figure 4.20. Illustration of the standard chart used to summarize the mode shape component data (produced using pseudo data) 75
Figure 4.21. Mode shape components of girder-normalized data from harmonic loading (D0, D1, D2, & D3) 76
Figure 4.22. Mode shape components for girder-normalized data from impact excitation (D0, D1, D2, D3) 78
Figure 4.23. Mode shape components for girder-normalized data from harmonic excitation (D0, D4, D5, D6) 84
Figure 4.24. Mode shape components from harmonic excitation for different weight cases 87
Figure 4.25. Change in mode shape - D0S0W1$_c$ vs. D0S1W1 (harmonic) 90
Figure 4.26. Change in curvature – D0S0W1$_c$ vs. D0S1W1 (harmonic) 90
Figure 4.27. Change in mode shape - D0S1W1 vs. D0S2W1 (harmonic) 91
Figure 4.28. Change in curvature – D0S1W1 vs. D0S2W1 (harmonic) 91
Figure 4.29. Change in mode shape - D0S1W1 vs. D0S2W1 (impact) 92
Figure 4.30. Change in curvature – D0S1W1 vs. D0S2W1 (impact) 92
Figure 4.31. Change in mode shape - D0S1W1 vs. D4S2W1 (harmonic) 93
Figure 4.32. Change in curvature – D0S1W1 vs. D4S2W1 (harmonic) 93

Figure 4.33. Mode shape components for the bridge with a constant foundation case D6, but under various superstructure condition states 95
Figure 4.34. Area under the change in mode shape and change in curvature plots when comparing the base case (D0S1W1) to other superstructure and substructure damage states 97
Figure 4.35. Area under the change in mode shape and change in curvature plots when comparing the base case (D0S0W1) to other superstructure and substructure damage states 98
Figure 4.36. Plan view of the bridge, showing accelerometer locations for practical application (dimensions in mm) 101
Figure 4.37. First flexural mode shape produced using limited sensors 101
Figure 4.38. Mode shape components for substructure condition states using the limited accelerometer configuration 102
Figure 5.1. A simple artificial neural network (Gurney 1997) 106
Figure 5.2. A.I. Solver user interface displaying results from both training and testing of the neural network 110
Figure 5.3. Graphical representation of the hard and soft damage cases, and their relationship to mode shape components ‘A’ and ‘C’ 111
Figure D.1. Mode shape component amplitudes from harmonic excitation I 141
Figure D.2. Mode shape component amplitudes from harmonic excitation II 142
Figure D.3. Mode shape component amplitudes from impact excitation I 144
Figure D.4. Mode shape component amplitudes from impact excitation II 145
Figure F.1. Change in mode shape - D0S0W1$_c$ vs. D0S1W1 (harmonic) 149

Figure F.2. Change in curvature – D0S0W1$_c$ vs. D0S1W1 (harmonic) 149

Figure F.3. Change in mode shape - D0S0W1$_c$ vs. D4S1W1 (harmonic) 149

Figure F.4. Change in curvature – D0S0W1$_c$ vs. D4S1W1 (harmonic) 149

Figure F.5. Change in mode shape - D0S0W1$_c$ vs. D5S1W1 (harmonic) 150

Figure F.6. Change in curvature – D0S0W1$_c$ vs. D5S1W1 (harmonic) 150

Figure F.7. Change in mode shape - D0S0W1$_c$ vs. D6S1W1 (harmonic) 150

Figure F.8. Change in curvature – D0S0W1$_c$ vs. D6S1W1 (harmonic) 150

Figure F.9. Change in mode shape - D0S1W1 vs. D0S2W1 (harmonic)..... 151

Figure F.10. Change in curvature – D0S1W1 vs. D0S2W1 (harmonic)..... 151

Figure F.11. Change in mode shape - D0S1W1 vs. D4S2W1 (harmonic)..... 151

Figure F.12. Change in curvature – D0S1W1 vs. D4S2W1 (harmonic)..... 151

Figure F.13. Change in mode shape - D0S1W1 vs. D5S2W1 (harmonic)..... 152

Figure F.14. Change in curvature – D0S1W1 vs. D5S2W1 (harmonic)..... 152

Figure F.15. Change in mode shape - D0S1W1 vs. D6S2W1 (harmonic)..... 152

Figure F.16. Change in curvature – D0S1W1 vs. D6S2W1 (harmonic)..... 152

LIST OF SYMBOLS

A	=	Cross sectional area
d	=	Diameter
E	=	Modulus of Elasticity
EI	=	Bending stiffness
f_i	=	Fundamental natural frequency (Hz)
G	=	Modulus of Rigidity
g	=	Acceleration due to gravity
k	=	System parameter for beam support conditions
k	=	Stiffness
k_s	=	Stiffness of the portion of a pile located below ground
k_p	=	Stiffness of the portion of a pile located above ground
k_{eff}	=	Effective substructure stiffness
L	=	Length of pile above ground
L_s	=	Length of pile extending below ground
R^2	=	Coefficient of determination
W	=	Uniformly distributed weight
α	=	Alpha, probability of making a type II error (false positive)
ΔA_{ϕ}	=	Area under the change in mode shape vector
$\Delta A_{\phi''}$	=	Area under the change in curvature vector
ΔM	=	Added mass on the bridge

$\Delta\phi_n$ = Change in mode shape vector

$\Delta\phi_n''$ = Change in curvature vector

ζ = Radius of influence of pile

ν = Poisson's ratio

ω = Fundamental natural frequency (rad/s)

ϕ_o = Measured mode shape vector

ϕ_n^* = Mode shape vector after damage (normalized)

ϕ_n = Normalized mode shape vector

$\phi_n''^*$ = Curvature vector after damage

ϕ_n'' = Curvature vector

ϕ_{Bn} = Bridge-normalized mode shape vector

ϕ_{Gn} = Girder-normalized mode shape vector

LIST OF ABBREVIATIONS

A.I.	Artificial Intelligence
Fdn	Foundation
FFT	Fast Fourier Transform
Labview	Laboratory Virtual Instrumentation Engineering Workbench
NF	Natural frequency
NI	National Instruments
No.	Number
SARM	The Saskatchewan Association of Rural Municipalities
SHM	Structural health monitoring
SHT	Saskatchewan Highways and Transportation
Std Dev.	Standard deviation
TM	Trademark
Typ	Typical
Ref	Reference
VBDD	Vibration-based damage detection

1. INTRODUCTION

1.1. BACKGROUND

Saskatchewan currently has a large inventory of timber bridges that are nearing or are at the end of their service life. A typical timber bridge in Saskatchewan is short-to-medium span, featuring simply supported girders and a timber deck. In some cases only the substructure (consisting of piles, pile caps and abutments) is constructed out of timber. Figure 1.1 presents a multi-span timber bridge spanning a long creek, while Figure 1.2 presents a timber substructure under a bridge.

Figure 1.1. Timber bridge (courtesy of Yang Sun)

Figure 1.2. A timber substructure (courtesy of Stantec Inc.)

The structural health monitoring (SHM) program presently employed by transportation agencies typically consists of lengthy visual inspections and minor non-destructive testing. Visual inspections are limited to structural members that are directly accessible to the inspectors, meaning that hidden deficiencies can remain undetected. These deficiencies can be substantial and numerous due to a timber bridge's susceptibility to many forms of deterioration, including weathering, rot, insect attack, and mechanical damage. In many instances, the damage is inaccessible and is located at the foundation in the form of pile rot at, or below, the ground surface. Given the large number of timber bridges in Saskatchewan, and the difficulties associated with visual inspections, it would be beneficial to have a method that would be capable of quickly detecting damage on a timber bridge.

Vibration-based damage detection (VBDD) methods have the potential to offer great insight into a structure's integrity when implemented into a routine structural health monitoring program. The vibration-based methods measure the structure's dynamic response to an excitation source using sensors. The characteristics obtained from vibration measurements typically include natural frequencies and their corresponding mode shapes, which can be used to assess a structure's health. Damage to the structure presents itself in the form of changes in mass or stiffness, both of which affect the vibration characteristics. Typically, the vibration characteristics of a structure must be periodically measured to detect small changes in the response, indicating damage that is occurring over time. However, it may also be possible to use specific vibration signatures based on a single measurement to detect specific types of damage by comparing the response with that of other structures with known condition states. Specifically, preliminary studies have indicated that changes in the timber bridge substructure (piles, pile caps and abutments) through deterioration affect the basic character of the vibration mode shapes (Beauregard et al. 2010; Sun et al. 2007).

1.2. OBJECTIVES

The objective of this research project was to examine the feasibility of using vibration-based methods to assess the structural integrity of short-to-medium span timber bridges. Specific sub-objectives included the following:

- To investigate the influence of substructure stiffness on the dynamic properties of a timber bridge;

- To determine if substructure deterioration can be detected reliably using the response from a single vibration test without the benefit of baseline (prior to damage condition) data;
- To investigate the influence that the distributed mass supported by the bridge deck has on the dynamic response of the timber bridge, given the non-linear nature of timber;
- To investigate the potential for VBDD methods to detect and locate small-scale damage in the timber bridge superstructure;
- To explore the relationship between substructure and superstructure damage with particular attention paid to the ability to simultaneously detect damage to the substructure and superstructure; and
- To investigate the influence of various testing parameters that may be employed in future field testing studies on timber bridges; more specifically, to assess excitation sources and the degree of instrumentation required.

In addition to the sub-objectives above, this research also included a preliminary investigation on the feasibility of using pattern recognition software to aid in determining the condition state of a timber bridge given a database of vibration signatures of known condition states.

1.3. SCOPE AND METHODOLOGY

The focus of this thesis was on the vibration testing of an intact portion of a decommissioned timber bridge within a laboratory setting. The following variables were analyzed individually to assess their effect on the bridge's dynamic response:

i. changes in support stiffness that were uniform across the bridge width;

ii. changes in localized support stiffness;

iii. changes in mass supported by the deck (to simulate a gravel driving surface);

iv. a reduction in the flexural capacity of a girder; and

v. excitation methods.

Attempts were made to characterize the specific forms of damage using vibration-based damage detection methods on the timber bridge. The effects of the specific variables were assessed by analyzing the resulting natural frequencies and their associated mode shapes. In addition, common VBDD methods were used for local damage detection, including the change in mode shape method (Wegner et al. 2011) and the change in curvature method (Pandey et al. 1991).

Investigations of both superstructure and substructure damage detection were undertaken based on comparisons with the response using baseline measurements taken at the bridge's original condition before the introduction of damage. In addition, specific forms of substructure damage were thoroughly investigated to determine if they could be detected by analyzing the vibration signatures obtained using a single vibration measurement. Further details regarding the experimental program are provided in Chapter 3.

1.4. LAYOUT OF THESIS

This thesis describes an experimental program and is presented in six chapters, plus references and appendices. An overview of the chapters is presented below:

Chapter 1 served as an introduction that outlined the problem and the objectives of the research.

Chapter 2 presents a literature review that summarizes past studies and literature related to this research. Background relating to timber bridges and vibration based-damage detection is presented.

Chapter 3 describes the experimental program. The laboratory timber bridge is described, in addition to the excitation and data acquisition methods. Finally, Chapter 3 introduces the damage cases considered, which include the superstructure and substructure damage cases.

Chapter 4 presents the main results of the research and provides some discussion. The effect of substructure and superstructure damage, as well as distributed mass on the dynamic response is studied. In particular, specific patterns in the mode shape profile are identified.

Chapter 5 describes the results of a brief study that used pattern recognition techniques to aid in predicting the state of a bridge using dynamic measurements. Based on a database of timber bridge vibration signatures for known condition states, the condition states of timber bridges were predicted.

Finally, Chapter 6 presents the conclusions of this study and subsequently outlines recommendations for future research.

2. LITERATURE REVIEW

2.1. INTRODUCTION

This chapter is a summary of the past research relating to timber bridges and vibration-based damage detection. Timber as a building material is described, with special consideration of its use in bridge construction. An overview of the current state of Saskatchewan's timber bridge network is also included.

The literature review concludes by providing a summary of research related to structural health monitoring using vibration-based damage detection. Various vibration-based damage detection methods are introduced, and their applications are presented. In particular, the application of VBDD to bridge structures is presented, with a focus on timber bridges and substructures.

2.2. TIMBER BRIDGES

2.2.1. Timber Characteristics

Timber is a highly sought-after building material due to its abundance as a renewable resource. There are many benefits to using timber for construction purposes when a proper design is implemented (Ou et al. 1986):

- Construction can take place in any weather;

- Timber is not affected by freeze-thaw cycles, or de-icing agents;
- Timber has good energy-absorbing abilities;
- Its light weight nature makes for easier construction, repair, and rehabilitation; and
- Capital and maintenance costs are competitive with other building materials.

Timber, however, does have many limitations, making its use practical only for specific bridge applications. Timber can degrade due to fungi, insects, marine borers, discolorations, weathering, chemicals, and fire (Ou et al. 1986). Specifically, the biotic agents such as decay, fungi, bacteria, insects, and marine borers require four conditions for survival: (1) adequate moisture, (2) adequate oxygen, (3) favourable temperature, and (4) food - the wood (Ritter 1990; Ou et al. 1986; Muchmore 1986).

These four factors are impossible to manage in a natural environment. However, the wood may be treated by a chemical preservation that is toxic to organisms, thus removing the food. Chemical treatment, however, can only penetrate the outer timber shell, making the internal structure assessable to decay where moisture can enter. Areas near fasteners, checks, and mechanical damage are highly susceptible to damage as they provide paths where moisture can enter, especially when these are also high moisture regions (RTA 2008; Ritter 1990). Figure 2.1 graphically shows the areas most vulnerable to decay from moisture.

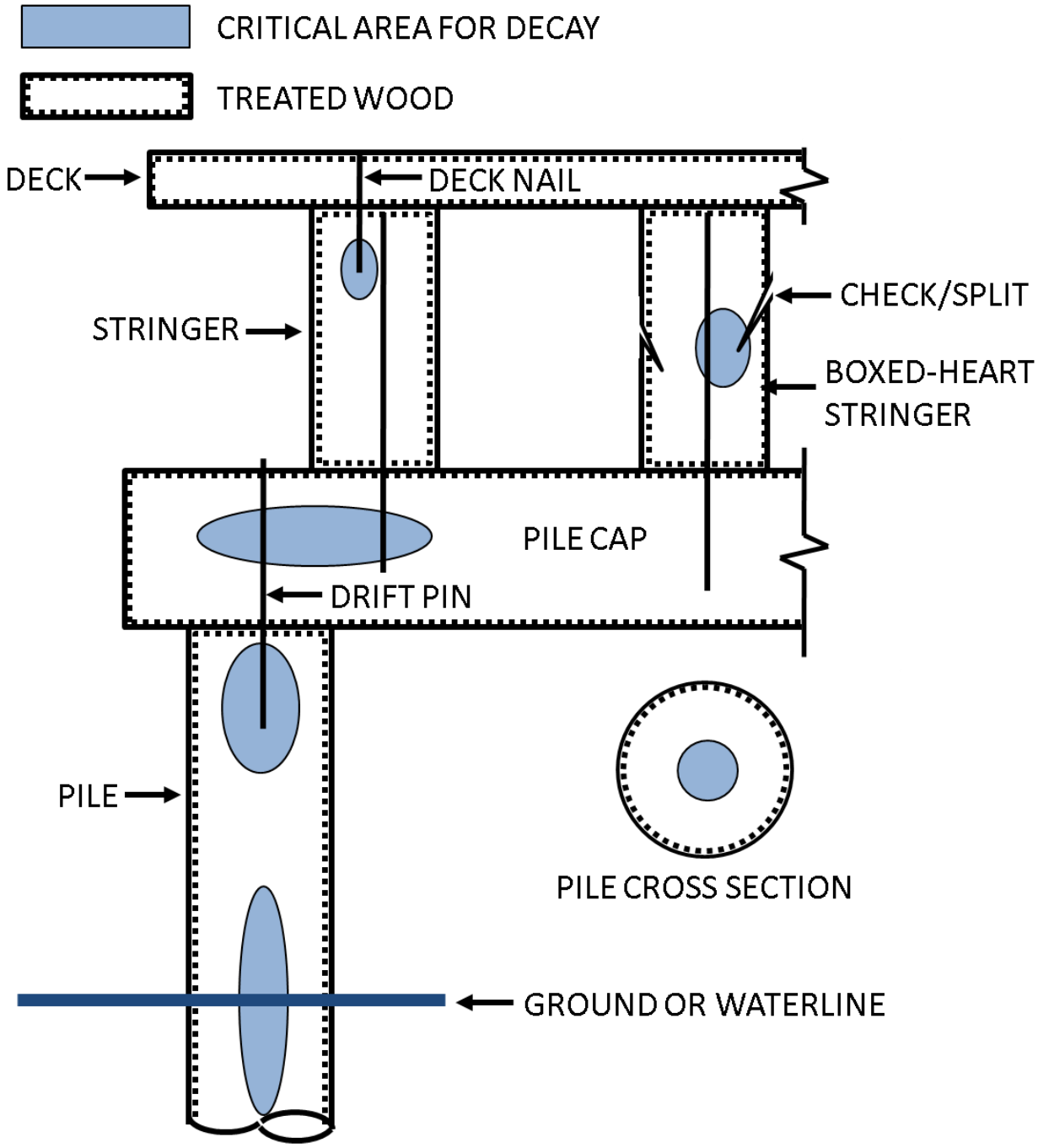

Figure 2.1. Diagram showing where decay is most likely to occur on a timber bridge (after Ritter 1990; RTA 2008; Muchmore 1986)

In addition to the decay presented in Figure 2.1, the substructure directly in contact with soil (the pilings and abutments) and wetting are the most susceptible to deterioration

(Ritter 1990). Unfortunately, the substructure can also be the most inaccessible, thus presenting the most difficulty during inspections.

2.2.2. Saskatchewan Timber Bridges

Saskatchewan's municipal bridge network consists mainly of short-to-medium span bridges constructed with some form of timber component. The Saskatchewan Association of Rural Municipalities (SARM) has approximately 1900 rural bridges in the Saskatchewan municipal bridge network, approximately 1700 of which have timber abutments (this does not include the infrastructure in the highway bridge network). The average construction date of these bridges was 1966. Additionally, the average expected lifespan for this bridge inventory is 60 years based on the experience of Saskatchewan Highways and Transportation (Watt et al. 2008).

The Saskatchewan Association of Rural Municipalities and Saskatchewan Highways and Transportation (SHT) retained Associated Engineering to do a strategic asset management plan of the rural municipal bridges (Watt et al. 2008). From this study, it was found that if all the bridges in Saskatchewan were replaced, very low importance bridges (likely the majority of the municipal bridge network) would account for 50% of the cost. This suggests that a very large portion of Saskatchewan's bridge network (in both value and quantity) is considered to be of low importance. Associated Engineering concluded that these low importance bridges, "by virtue of this examination and limited funding, should not be a priority in any capital replacement or repair program". These conclusions were made with consideration to the large bridge network and limited funding available, assuming the continued use of current expensive inspection

techniques. Therefore, the need for effective monitoring is evident to prolong the useful life of this large bridge network.

2.3. VIBRATION-BASED DAMAGE DETECTION

2.3.1. Overview

Vibration–based damage detection techniques have great potential to be used in a routine structural health monitoring program. However, much of the current research and existing techniques are limited to the use of periodic testing throughout the structure's service life to detect changes in response, thus indicating damage. A common classification system for damage detection was presented by Rytter (1993), which defines the different levels of structural health monitoring:

- Level 1 - Damage detection: determination that damage is present in the structure;
- Level 2 - Damage localization: determination of the geometric location of the damage;
- Level 3 - Quantification of the severity of the damage; and
- Level 4 - Prediction of the remaining service life of the structure.

The techniques and approaches taken in past research have mostly limited damage detection efforts to the first two levels. As well, in the case of bridges, superstructure damage detection has been the main focus and substructure condition has been largely neglected or ignored.

2.3.2. VBDD Techniques

Vibration-based damage detection (VBDD) methods make use of the dynamic characteristics of a structure, such as its mode shapes and their associated natural frequencies. A mode shape is the representation of a structure's deflected shape at a given mode (resonant vibration). The associated natural frequency is the characteristic rate at which the mode shape vibrates in cycles per second.

There have been numerous studies since 1970 that have developed the field of vibration monitoring. Doebling et al. (1998) and Sohn et al. (2004) have provided extensive summaries and reviews of many of the past studies. These summaries also provide an overview of many of the methods that have been studied.

Two of the most common VBDD methods employed in the literature are the change in mode shape method (Wegner et al. 2011) and the change in curvature method (Pandey et al. 1991). These are described below with consideration limited to the use of only the first flexural mode shape (the first flexural mode is further described in Section 3.6.2).

The change in mode shape method is a basic form of damage detection that compares two normalized (scaled) mode shapes. The change in mode shape can be calculated as

$$\Delta\phi_n = \phi_n^* - \phi_n \,, \qquad [2.1]$$

where ϕ_n and ϕ_n^* represent the normalized mode shapes before and after damage, respectively. The method is based on the premise that the greatest change in the mode shape is likely to occur at the damage location.

The change in curvature method is much the same conceptually as the change in mode shape, but considers the second derivative (or curvature) of the mode shape with respect to position rather than the mode shape directly. The change in curvature approach was first proposed by Pandey (1994) and can be calculated as follows:

$$\Delta\phi_n'' = |\phi_n''^* - \phi_n''| \,, \qquad [2.2]$$

where ϕ_n'' and $\phi_n''^*$ represent the normalized mode shape curvature vectors before and after damage, respectively. Damage is then indicated by large peaks in the plots of $\Delta\phi_n''$.

Zhou (2006) further refined the change in curvature method by taking the absolute value of each element in the vectors prior to calculating the difference. This can be calculated as follows:

$$\Delta\phi_n'' = |\phi_n''^*| - |\phi_n''| \,, \qquad [2.3]$$

which results in a change in curvature vector with fewer positive peaks, a feature that more clearly indicates the location of damage.

Prior to applying the VBDD methods, the mode shape amplitudes must be normalized to allow for direct comparison. Normalization removes the effect that excitation intensity has on the modal amplitudes. Since the excitation force is usually not measured, the resulting mode shape amplitudes are arbitrary and must be scaled to a similar basis before and after damage. In this study, the unit-area normalization scheme was used to limit the influence that the number and location of sensors has on the normalization process (Wang et al. 2009). To remove the effect of the vector length in this method, the

length of the element described by the mode shape was normalized to unity prior to unit-area normalization. The unit-area normalized mode shape, ϕ_n, could then be calculated as follows:

$$\phi_n = \frac{\phi_o}{\int_0^1 \phi_o \, dx} , \quad [2.4]$$

where ϕ_o is the measured mode shape, and the bridge span has been scaled to unity.

In addition to the Level 2 damage detection methods described above, some Level 1 methods have been developed that consider the statistical likelihood that damage has occurred on each girder. Wang et al. (2009) successfully used a method based on the area under the change in mode shape vector produced using Equation 2.1. This change in area can be calculated as:

$$\Delta A_\phi = \int_0^1 |\Delta \phi_n| dx , \quad [2.5]$$

where x defines the position along the girder, and $\Delta\phi_n$ is the change in mode shape vector calculated using the two mode shape vectors being compared, both of which have been unit-area normalized. A similar calculation can be carried out using the change in curvature vector, as shown below:

$$\Delta A_{\phi''} = \int_0^1 |\Delta \phi_n''| dx , \quad [2.6]$$

where x defines the position along the girder, and $\Delta\phi_n''$ is the change in curvature vector calculated using Equation 2.3. Based on the area under the change in mode shape and

the change in curvature vectors, a statistical threshold can be developed to provide an indication of whether damage is, in fact, present.

2.3.3. VBDD Research at the University of Saskatchewan

Researchers at the University of Saskatchewan have undertaken extensive research in the field of VBDD. The research has included numerical modelling, in addition to practical applications of these methods. Laboratory testing has been used to create proper testing protocols for the application of VBDD methods, and field testing has been conducted on actual bridge structures in Saskatoon and the surrounding area.

Zhou (2006) studied the use of accelerometers and strain gauges. It was found that mode shapes derived using accelerometers were better able to detect small degrees of damage. In addition, this study showed that harmonic excitation from a hydraulic shaker applied at the bridge's natural frequency could be used to detect small forms of damage with a greater degree of success compared to white noise excitation or impact. It was concluded that mode shapes produced using accelerometers and harmonic loading gave the most reliable and precise mode shapes.

Based on past studies at the University of Saskatchewan, it has been concluded that the fundamental vibration mode, obtained using resonant harmonic loading, was the most suitable for damage detection since this combination produced the most precise and accurate mode shapes and natural frequencies (Wang et al. 2008; Wang et al. 2009). Additionally, the use of higher modes was found to actually hinder damage detection, when compared to using only the fundamental mode shape (Zhou 2006).

Additional studies considered the effect of temperature changes on VBDD methods (Siddique 2008; Pham, 2009). It was found that temperature changes significantly alter the natural frequencies; however, the measured mode shapes were relatively insensitive to changes in temperature. Siddique (2008) completed field and numerical testing, and considered variables such as normalization, sensor spacing and damage parameters.

Further research at the University of Saskatchewan that considered substructure damage to timber bridges is presented in Section 2.3.4 (Sun et al. 2007; Beauregard et al. 2010).

2.3.4. VBDD with Timber

Several possible techniques exist that could be implemented in a routine structural health monitoring program of timber bridges to detect deficiencies. Available non-destructive techniques include visual inspection, stress wave, ultrasonic, drill resistance, radiography, microwave, and vibration (Emerson et al. 1998). Although many of these techniques detect damage locally, they are limited by the time and effort required to assess the entire structure, which is further complicated by inaccessible components. On the other hand, vibration methods are global techniques (i.e. based on the measurement of the overall structural response) that are capable of detecting local damage in the form of a change in stiffness and/or mass.

Vibration-based damage detection methods applied to timber bridge superstructures have been effectively implemented in the laboratory. The damage index method has been used to successfully locate damage on a simply supported three-girder bridge

tested in the lab (Peterson et al. 2003). The simulated damage cases consisted of a pocket of decay at the end of a girder, and a reduction in the bending moment capacity at the centre of one girder. In earlier tests, Peterson detected similar damage on a single timber beam (159 mm deep by 114 mm wide) spanning 4.83 m (Peterson et al. 2001). In another study, severe damage was detected simultaneously at multiple locations on a timber bridge in the laboratory using the damage index method for plate-like structures (Samali et al. 2007). A limitation of all of the studies mentioned above was that the timber girders tested were very flexible compared to those used typically in construction.

Tests have been done on timber bridges in the field to correlate the stiffness of the bridge to the bridge's structural integrity using the first flexural mode of vibration (Brashaw et al. 2008). The research proposed a formula from beam theory to calculate the bending stiffness of a bridge's superstructure:

$$EI = \frac{{f_i}^2 * W * L^3}{k * g} \qquad [2.7]$$

where f_i is the fundamental natural frequency, k is a system parameter (for example, k=2.46 for pin-pin end supports), W is the uniformly distributed weight, g is the acceleration due to gravity, and L is the span of the bridge. The research considered twelve spans (from eight different bridges) and found that Equation 2.7 had a statistical correlation coefficient (R^2) of 0.84, when compared to measured results for bending stiffness using static loading. Sources of error included the unknown weight of the bridges, and the means by which the first flexural natural frequency was gathered. The

researchers noted that the dynamic test results that varied most from the static load test results corresponded to bridges in which considerable substructure decay was noted, suggesting that the substructure damage affected the natural frequency of the structure. All substructure damage was detected using stress wave timing and resistance microdrilling.

In another study (Samali et al. 2003), stiffness values for several timber bridges in the field were determined using a frequency shift approach. The first natural frequency was established, and the frequency shift was recorded after a known uniform mass was added to the centre of the bridge. Given the change in mass and frequency shift, the stiffness of the bridge at mid-span could be calculated as (Li et al. 2004)

$$k = \frac{\omega_1^2 \omega_2^2}{\omega_1^2 - \omega_2^2} \Delta M \qquad [2.8]$$

where k is the stiffness of the bridge in N/m, ΔM is the added mass on the bridge in kilograms, and ω_1 and ω_2 are the fundamental natural frequency (in rad/s) of the bridge before and after the addition of mass, respectively.

Preliminary research has been carried out at the University of Saskatchewan using VBDD methods to detect substructure deterioration. A study found that it is possible to detect support softening under a single stringer (Sun et al. 2007). In this study, it was concluded that reduced support stiffness could be inferred through a simple observation of the fundamental mode shape without reference to data obtained prior to support softening (baseline measurement). The distinct sinusoidal mode shape for the rigid support case changed to a mode shape that featured increasingly linear rigid body

motion about the damaged support. In addition to the increased movement over the damaged support, the fundamental natural frequency decreased with increased substructure flexibility. The study was expanded to a full scale timber bridge in the laboratory (Beauregard et al. 2010). Uniform and non-uniform support softening was detected without a baseline case, based on an observation of the first flexural mode shape. In addition, it was proposed that the timber bridge's health could quantitatively be evaluated by comparing the distinctive response signature to those found in a database of bridges in various states of deterioration. A limitation of both of these studies was the unrealistic (highly flexible) supports that were considered to compare to the rigid case.

The limited research completed so far related to detecting substructure damage has focused on identifying distinct response signatures to overcome the difficulties associated with the requirement of a baseline (prior to damage) model, which would likely not be available for most bridges in practice. The proposed method uses specific patterns of foundation movement (over the supports) observed within mode shapes to infer the presence of damage to the supports (Beauregard et al. 2010). Considerable movement of the deck directly over the supports has also been observed due to the compressibility of the timber pile cap, even in the absence of support softening. Support movement has been observed in a healthy substructure (Beauregard et al. 2010), as well as for a girder with internal decay near the support (Peterson et al. 2001). Further work is required to accurately differentiate and separate this movement over the support due to the compression of superstructure members from that due to substructure deterioration.

2.3.5. Further VBDD on Substructures

Many VBDD methods have been applied successfully assuming simple rigid supports; however, very little work has been done considering the effect of an elastic foundation on testing. An experimental and numerical study was completed by Burkett (2005) that considered scour and settlement of the foundation using a two-span steel structure in the laboratory. Changes in mode shape, curvature and frequency were identified in damage cases that resulted in a considerable change in the support stiffness when compared to the baseline. Damage cases included pile loss and pile settlement. Fayyadh and Razak (2012) conducted a similar study considering the deterioration of elastic bearing pads under a reinforced concrete girder in the laboratory. In addition to observing symmetry changes to the fundamental mode shape when considering different support stiffness on either end of the girder, the researchers observed an increase in the third mode's natural frequency with decreased support stiffness. Of the first six modes studied, only the third mode featured this trend; all other modes (1,2,4,5 and 6) had a decreasing natural frequency with decreasing support stiffness.

Another study used dynamic testing before and after rehabilitating a concrete bridge that was affected by foundation scour damage (Foti et al. 2011). The bridge consisted of five simply supported spans in which one of the internal piers had begun to experience increased settlements due to scour caused by a flood. Prior to retrofitting the damaged pier, vibration testing revealed relatively large movements over the damaged pier and anomalies in the movement of the adjacent spans. Both of these observations were resolved after the damaged pier was retrofitted.

3. DESCRIPTION OF EXPERIMENTAL STUDY

3.1. INTRODUCTION

The experimental program for this study featured dynamic testing carried out on a timber bridge to detect substructure damage. All testing was carried out in a laboratory setting on a decommissioned timber bridge deck.

This chapter provides an overview of the timber bridge used in this study and the excitation methods used to vibrate the bridge. Also included is a description of the instrumentation, signal processing and data analysis methods.

In addition, this chapter presents the results of some preliminary testing and introduces the damage cases considered for the experimental program. For this study, condition states of primary interest featured damage to the substructure. Investigations of additional influences, such as the effect of varying superimposed mass on the bridge deck (ballast) and superstructure damage are also discussed.

3.2. TIMBER BRIDGE

All testing was done on a portion of a decommissioned timber bridge that was brought into the University of Saskatchewan Structures Laboratory, as shown in Figure 3.1. The timber bridge consisted of four girders that rested on pile caps; both the girders and pile caps had cross-section dimensions of 200 mm x 390 mm. The girders had a single

simply supported span of 5.45 m. The timber deck had dimensions of 2.44 m wide by 5.9 m long, and was constructed using a series of 45 mm x 90 mm timber planks. The timber planks were placed with the longer dimension oriented vertically and were fastened together and to the girders with nails to provide a continuous deck surface. It was assumed that the deck construction and its connection to the girders was typical of timber bridge construction in Saskatchewan. The girders and deck were initially not connected to the pile caps, and there was also a portion of the deck that had to be rebuilt (approximately 600 mm at one end of the bridge for the entire width). Prior to any testing, the girders were attached to the pile caps with No. 25 rebar dowels and new deck planks were added to match the existing. A plan view and cross-section of the bridge are shown in Figure 3.2.

Figure 3.1. The timber bridge in the laboratory

The pile caps were initially rigidly supported on the laboratory floor with steel blocks to simulate the perfectly rigid support case, as shown in Figure 3.1. The substructure damage that was later introduced to the supports is described in Section 3.7. Throughout this study, the “left support” (left pile cap) signifies the left support line shown in Figure 3.2; similar terminology is used with the right support.

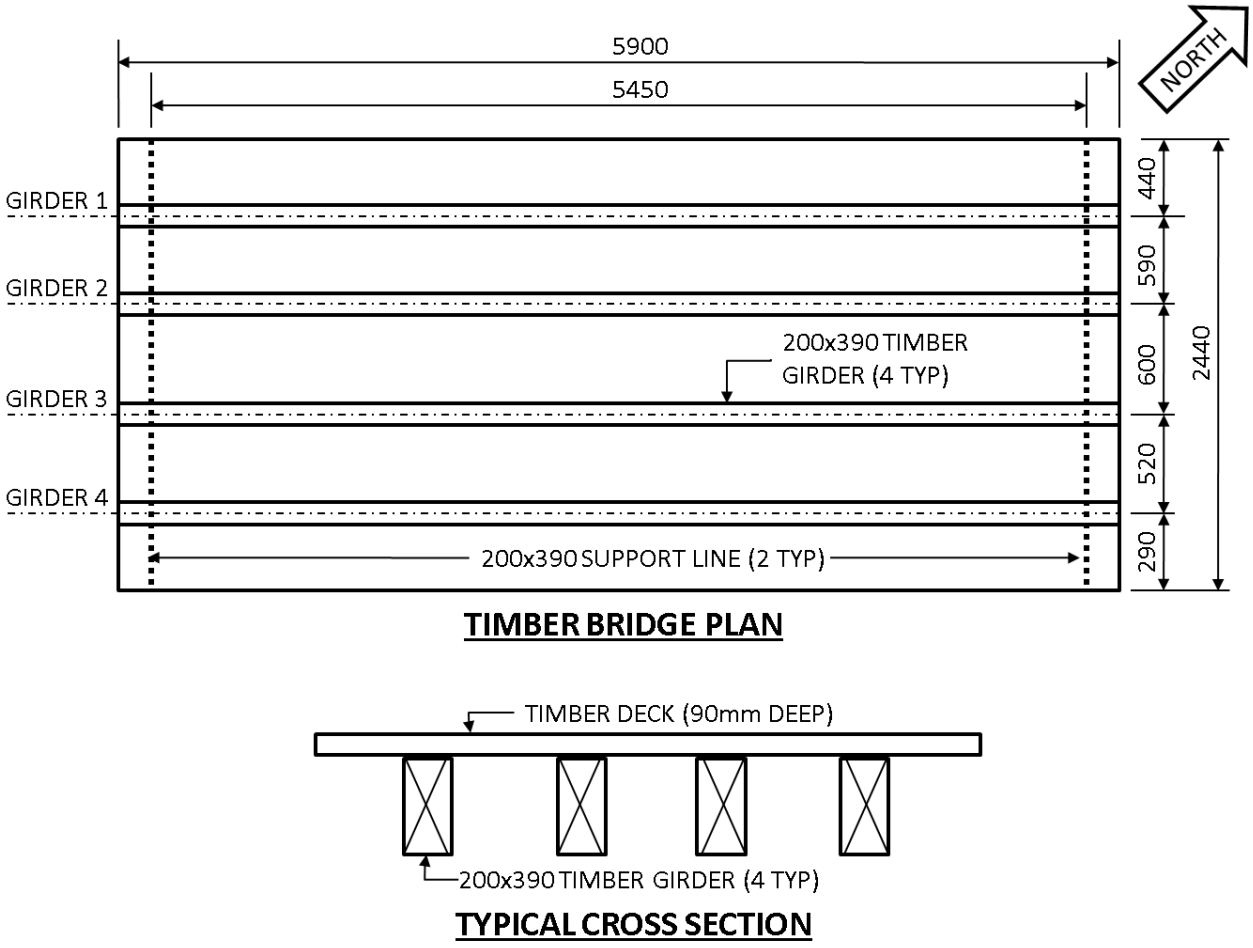

Figure 3.2. Plan view and cross-section of the timber bridge (dimensions in mm)

3.3. EXCITATION

3.3.1. Overview

This section covers the methods used to excite the timber bridge. The two methods considered in this study were an impact strike with a sledge hammer and harmonic loading with a hydraulic shaker. Both excitation methods were applied to the centre of the bridge to best stimulate the first flexural mode.

3.3.2. Impact

Two impact intensities were initially considered: impact produced by a sledge hammer, and a carpenter's hammer. Impact excitation was able to stimulate a wide range of frequencies simultaneously with a single strike; the effectiveness of the impact for a given mode depended on the excitation location on the bridge. Since the first flexural mode was of primary interest, it was found through preliminary testing that the sledge hammer blow to the centre of the bridge best excited the first natural frequency. No further testing was done with the carpenter's hammer.

In subsequent tests, the sledge hammer loading was induced by means of a small strike near the centre of the bridge, which was found to excite the first flexural mode without significant participation of other modes (however, prior to taking the steps listed in Section 3.6.3, there was energy transfer from the first flexural mode to other modes). A typical impact test used a 5.5 kg hammer with an approximate fall height of 100 mm. After impact, the bridge would vibrate freely until the vibrations were completely dampened.

3.3.3. Hydraulic Shaker

Harmonic loading was achieved using a hydraulic shaker, seen in Figure 3.3, as the excitation source. The shaker featured a steel frame, on which a hydraulic cylinder was mounted that supported a suspended mass, with a total combined mass of 86.2 kg. Forced oscillation of the 43.5 kg suspended mass was used to generate harmonic excitation at the desired forcing frequency, as controlled by Labview^{TM} 8.0 software.

Figure 3.3. The hydraulic shaker on the timber bridge

The shaker was used primarily to vibrate the bridge model at the first flexural frequency. The first flexural mode was also best excited with the shaker in the centre of the bridge. Other locations were considered, but they resulted in differential movement between the girders due to the relatively large mass of the shaker, which, when mounted eccentrically, produced torsional motion.

In addition to a single harmonic excitation, the hydraulic shaker could sweep progressively through a range of frequencies based on a control written using Labview^{TM} 8.0 software. The sine sweep was implemented to precisely identify the first natural frequency based on the largest bridge response observed during the sweep (described further in Section 3.5.2).

3.3.4. Summary

Two types of excitation were used for the experimental study: impact and harmonic loading. It should be noted that the hydraulic shaker was in place for the entire experimental program, resulting in the same mass on the bridge regardless of the excitation applied. A summary of the methods is shown in Table 3.1.

Table 3.1. Excitation methods

Excitation Method	Graphic	Description
Harmonic Loading	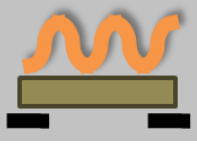	The hydraulic shaker vibrated the bridge at its first flexural natural frequency. It consisted of a steel frame with a 43.5 kg mass connected to a piston. The shaker was placed at the centre of the bridge.
Impact	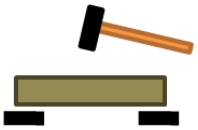	The timber bridge was excited by a 5.5 kg sledge hammer blow near the centre of the bridge. A single blow from the approximately 100 mm drop caused free vibration of the bridge for approximately 8 seconds.

3.4. ACCELEROMETERS

Accelerometers were used to capture the bridge's vertical response to excitation. A typical Kinemetrics EpiSensor FBA ES-U accelerometer is shown in Figure 3.4. The accelerometers were set to measure accelerations of ± 0.5g at a sampling rate of 500 Hz. The data were collected by LabView^{TM} using a 16-bit data acquisition system

consisting of an NI PCI-6024E data acquisition card and a model SCXI-1001 data acquisition chassis from National Instruments™.

Figure 3.4. Accelerometer

The accelerometers were used to measure the motion at 22 locations across the timber deck surface, as shown in Figure 3.5. The sensors were levelled and then secured to plywood pads with bolts that were secured to the deck along the girder lines at a spacing of 1.09 m. The placement of the accelerometers on the plywood pads ensured that the accelerometers were in the same location throughout the experimental program. Three accelerometer configurations were required to achieve the 22 point grid with the eight available accelerometers, as shown in Table 3.2. One accelerometer remained stationary through all tests (reference accelerometer #10) to provide a common basis to relate the data from the different configurations. Due to the number of possible nodes on the 1.09 m grid pattern and the eight available accelerometers, two potential accelerometer locations were not considered, one on Girder 2 and one on Girder 3. However, the accelerometer distribution over the timber bridge ensured a dense grid of data points at the supports, centre of the bridge, and outer girders.

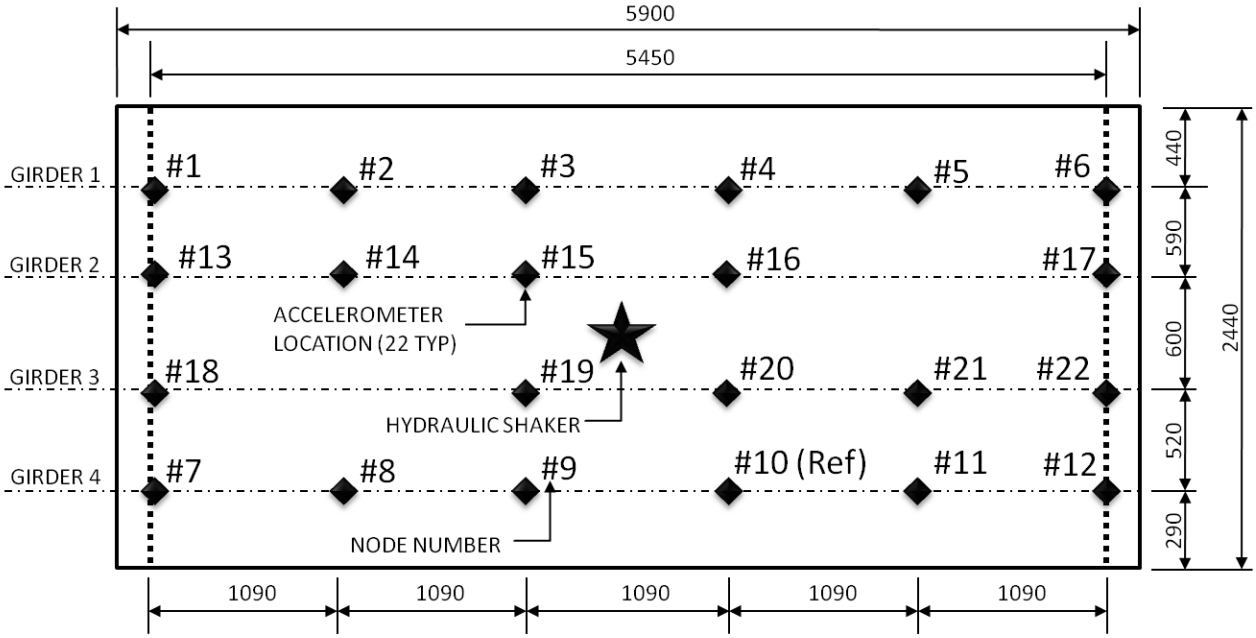

Figure 3.5. Plan view of the bridge deck, showing the location of accelerometers and excitation (dimensions in mm)

Table 3.2. Definition of the three accelerometer configurations

Accelerometer Configuration	Accelerometers Included[a]							
	A1	A2	A3	A4	A5	A6	A7	A8
1	#1	#2	#3	#4	#5	#6	#12	**#10**[b]
2	#13	#14	#15	#16	#21	#17	#9	**#10**[b]
3	#18	#8	#19	#20	#11	#22	#7	**#10**[b]

[a] See Figure 3.5 for locations referred to in this table

[b] Reference accelerometer

All the accelerometers were calibrated prior to testing by adjusting the sensor readings to ensure conformity between sensors. The calibration process was achieved by stacking the accelerometers in a tower and applying a harmonic vibration to the horizontal bridge surface on which the tower was placed. A sine wave that coincided with the first natural frequency of the bridge was applied using the hydraulic shaker. After the accelerometers were cycled through all possible positions within the tower, an accelerometer calibration factor was determined based on the relative reading from a

single accelerometer, averaged over all possible positions within the tower, compared to the average reading from all accelerometers. Cycling the accelerometers through different positions within the tower in the calibration process was required to remove the influence of potential differences due to rotation of the tower.

3.5. DATA PROCESSING AND TESTING PROTOCOL

3.5.1. Overview

Dynamic methods typically require a large amount of data processing to produce meaningful results, such as natural frequencies and their associated mode shapes. Another important reason for processing data is to remove random errors and noise that may cause spurious results. This section describes the methods used to process the raw accelerometer data gathered during the dynamic test to obtain the dynamic characteristics of the bridge.

3.5.2. Data Acquisition

As previously mentioned, the dynamic characteristics were established using two forms of excitation for the entire research program (impact and harmonic loading). The first flexural natural frequency was originally determined from five repeated trials using impact excitation and a single accelerometer configuration (Configuration 1, as shown in Table 3.2). Based on a sampling period of 8.2 seconds (at a sampling rate of 500 Hz), the resulting precision for the natural frequency from an impact was limited to ±0.12 Hz. Subsequently, a more precise (±0.05 Hz) first flexural natural frequency was determined using a sine sweep applied by the hydraulic shaker. The sweep excitation frequency

was incremented by 0.05 Hz every 5 seconds over a frequency range defined by ±0.3 Hz from the natural frequency obtained previously through impact loading. The sine sweep test was repeated for five trials, each having a duration of approximately 120 seconds. The natural frequency was selected based on the highest response amplitude indicated by spectral averaging using the Welch-Method (Welch 1969). It should be noted that the sine sweep test may not have had a constant energy input for each trial; however, the natural frequency presented itself quite clearly in the test results and the bridge response did not change considerably with minor shifts in excitation frequency.

Finally, the accelerometers were positioned in each of the three configurations shown in Table 3.2 while gathering data for both impact loading and harmonic loading. In both cases, each test consisted of five trials with a length of 8.2 seconds at a sampling rate of 500 Hz (4096 data points for each trial). The impact trials were performed first by measuring the response of the bridge to a hammer strike. The hydraulic shaker was then set to operate at the natural frequency identified using the sine sweep test, as described previously.

3.5.3. Signal Processing

The purpose of signal processing was to remove any error associated with signal drift, random instrument variability and electrically induced noise. In addition, signal processing converted the raw accelerometer data to useful dynamic characteristics such as natural frequencies and mode shapes. This study focused primarily on the first

flexural mode; as such, steps were taken to isolate and excite only this mode. However, the first torsional mode could also be extracted when impact loading was used.

Figure 3.6 summarizes the data processing methods in a flow chart; the individual steps are discussed in detail in the following paragraphs. The processed accelerometer data were used to produce natural frequencies and their associated mode shapes. The accelerometer data were not converted to displacements since the mode shapes could be generated directly from accelerations.

The protocol used to gather the raw accelerometer data for both harmonic and impact loading was described in the previous section (3.5.2). The following paragraphs describe the steps taken to process the data, which were implemented using a customized MATLAB routine. A further description of the MATLAB routine and the functions used can be found in Appendix A.

The accelerometer calibration factor was first applied to scale the raw accelerometer data to correct for individual sensor differences. A high-pass and low-pass Butterworth filter (Butterworth 1930) was then applied to remove accelerometer drift and high frequency interference, respectively. The filter had a low-pass cut-off frequency of 50 Hz and a high-pass cut-off frequency of 1 Hz. A moving window average of five data points was then applied to remove some additional random noise in the signal. Finally, prior to converting the data to the frequency domain using a Fast Fourier Transform (FFT), a Parzen window function (Ramirez 1985) was applied to the accelerometer data to limit spectral leakage by smoothing the data at the start and end of the sampling period to zero.

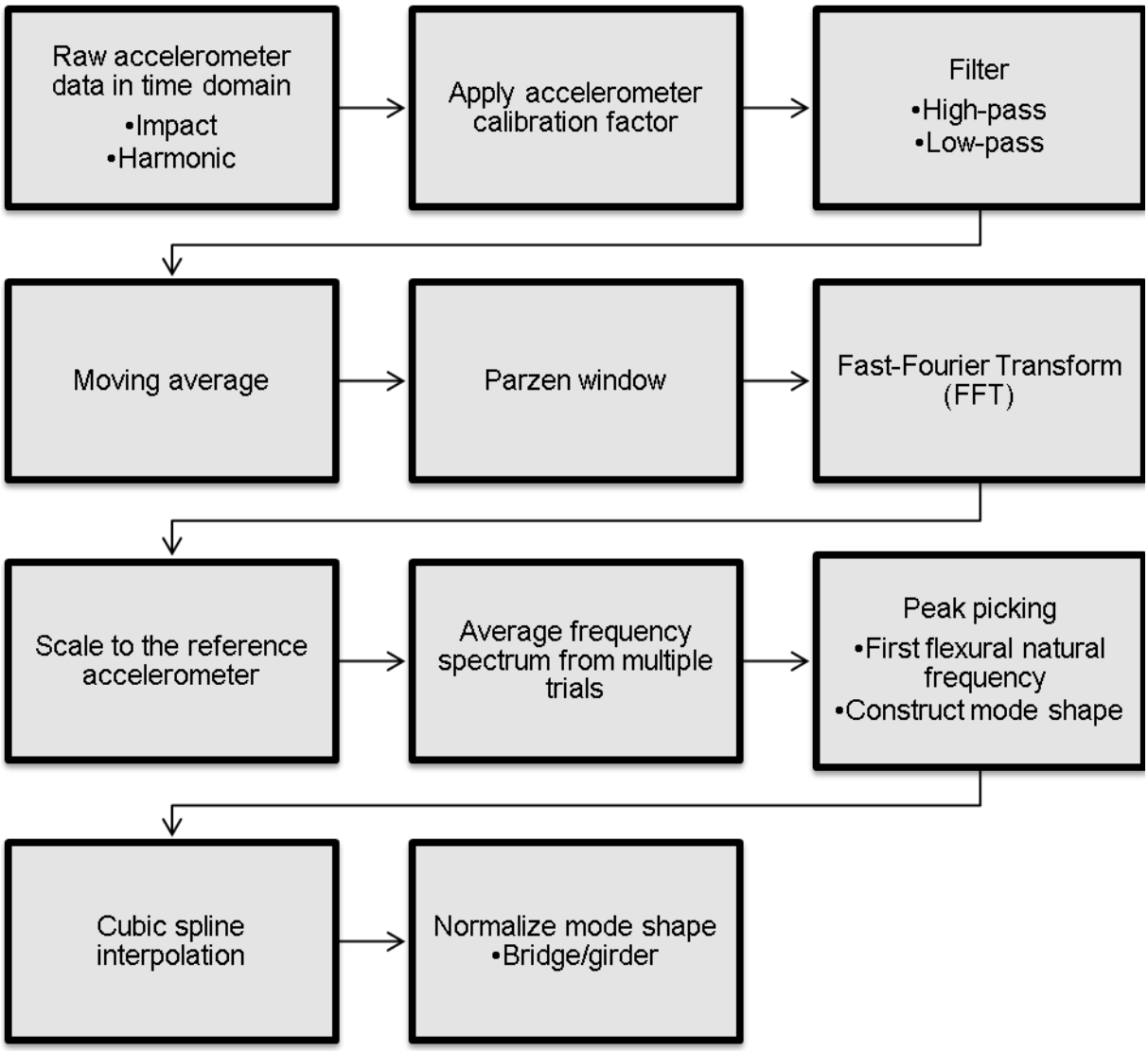

Figure 3.6. Data processing flow chart

The FFT was then applied to the modified acceleration time histories to produce a frequency domain representation. The spectra was scaled by a constant factor for each test so that the fundamental frequency for the reference accelerometer had a magnitude of unity for each of the three accelerometer configurations; this was done to ensure that the responses from each spectrum could be directly compared and merged. To further remove random errors present in individual trials, the frequency spectra from the five

trials were averaged. Using the peak picking method, the first flexural natural frequency and associated mode shape were then extracted. Specifically, to construct the mode shape using the peak picking method, the amplitude of the peak at the first flexural frequency was used to quantify the magnitude of motion for a location on the mode shape. After the responses for all of the accelerometer locations were compiled together, the mode shape could be plotted. For the harmonic loading, the spectra featured a single response peak at the forcing frequency; however, impact excited modes over a wide frequency band.

Once the mode shape was constructed, a cubic spline function was fit through the points representing the measured mode shape amplitude along each individual girder (22 points over four girders). The interpolation function ensured that the mode shapes could be described as a smooth vector defined at a larger number of points (10 mm increments along each girder), giving the possibility of more precise results when VBDD methods were implemented. The cubic spline used (Luong 2009) had boundary conditions of zero curvature at the supports to model the assumed beam behaviour.

Since the mode shape amplitude scaling was arbitrary, normalization was required to appropriately scale and compare the mode shapes directly. Prior to normalization, the length of the bridge for each individual girder was scaled to a unit length to limit the influence of bridge length and sensor configuration on the normalization process (Wang et al. 2009). Subsequently, two normalization schemes were considered: bridge-normalization and girder-normalization. For bridge-normalization, the area under the mode shape for the entire bridge (under all four girders) was scaled to a unit area. In the girder-normalization method, the mode shape curve representing each individual girder

was scaled to enclose an area of unity. As such, the relative mode shape amplitudes between girders were maintained in the bridge-normalized method, and lost in the girder-normalized method. Further equations and figures describing the two normalization schemes are presented in Section 4.2.3.

3.6. PRELIMINARY TESTS TO DEFINE TEST PROTOCOLS

3.6.1. Overview

This section briefly summarizes some of the preliminary testing that was done to understand the bridge behaviour prior to undertaking the main experimental program. Based on these findings, specific decisions were made regarding the testing conditions for the remainder of the testing program. Specifically, this section covers issues related to the energy transfer between the closely spaced lower modes.

3.6.2. Interference Between Lower Modes

Initial dynamic testing was applied considering an unloaded bridge and the hydraulic shaker located over node #15 (Figure 3.5). These initial tests revealed that two lower vibration modes were spaced very close together on the frequency spectrum (i.e., had similar natural frequencies). This resulted in problems with exciting the first flexural mode using either harmonic or impact excitation without also generating interference from the first torsional mode. Instead of extracting pure mode shapes, peak picking methods resulted in “operational deflection shapes” containing more than one mode, with each having a different shape and phase angle (time lag). It should be noted that the “operational deflection shapes” could be misinterpreted as actual mode shapes for

structures with closely spaced natural frequencies. In addition, typical impact tests with excitation to the centre of the bridge resulted in initial excitations to the fundamental frequency with subsequent energy transfer to the torsional modes (outer girders).

Figure 3.7 shows the two lower mode shapes, including the first flexural and first torsional modes. These mode shapes were produced using impact loading on the unloaded timber bridge deck; however, the hydraulic shaker was located at node #15. Theoretically (and also in Figure 3.7), the first flexural mode shape should result in girder motion that is synchronized (in-phase) and has similar amplitudes at corresponding locations on all the girders. On the other hand, the first torsional mode should result in differential movement across the girders, with the two halves of the bridge being 180^{o} out of phase with each other. In many of the preliminary tests, it was found that it was difficult to discern between the two mode shapes, since the frequencies were closely spaced, as shown on the spectrum in Figure 3.8.

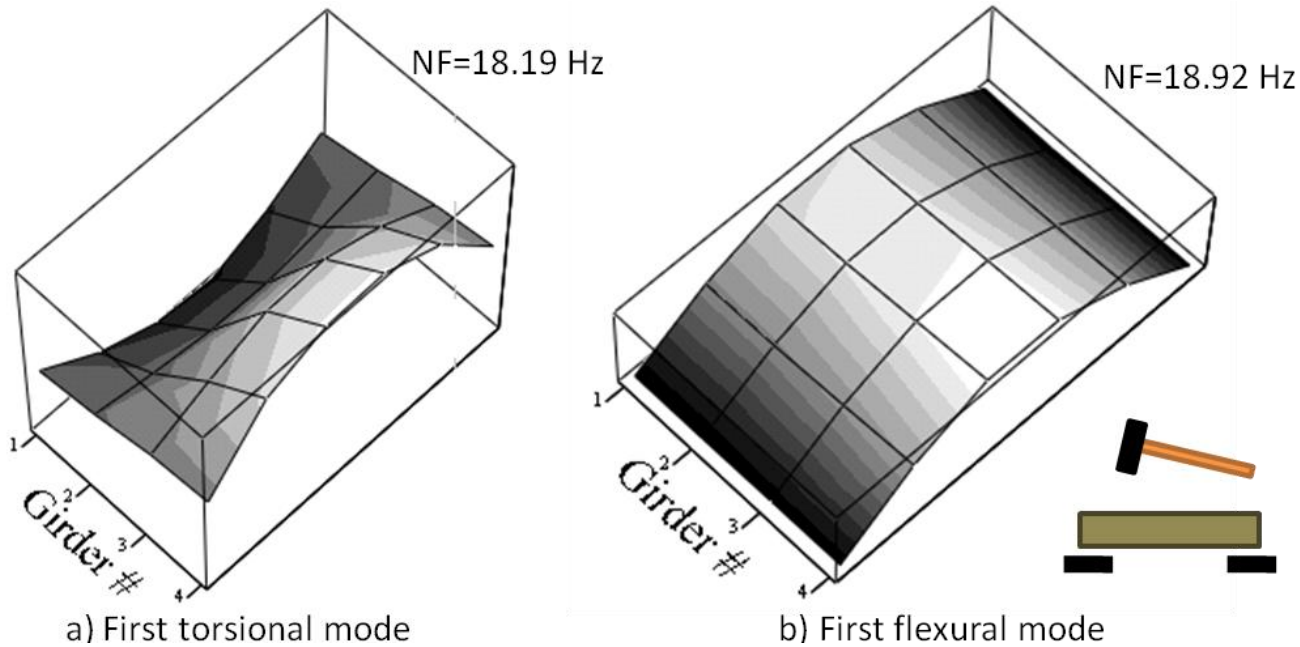

Figure 3.7. Comparison of the first torsional and first flexural mode shapes of the bare bridge

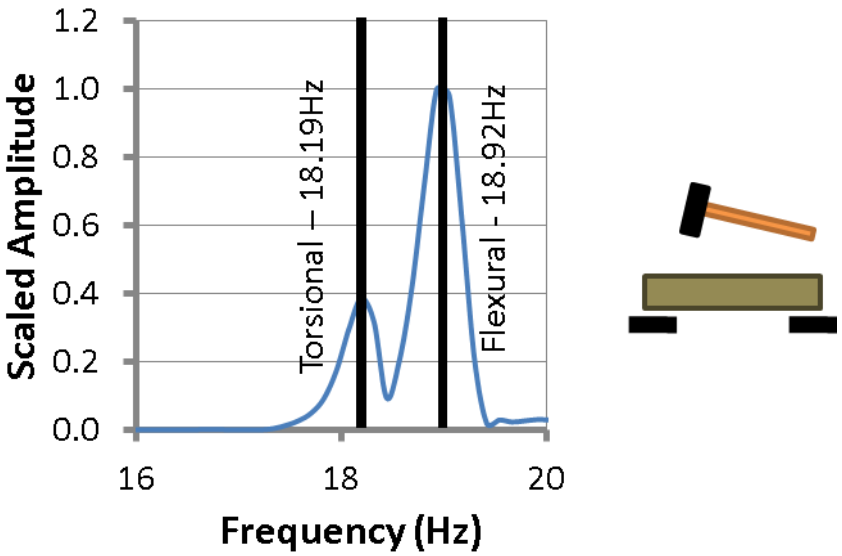

Figure 3.8. Partial frequency spectrum for the reference accelerometer obtained using impact excitation, showing the closely spaced flexural and torsional modes

The closely spaced lower modes resulted in the extraction of apparent mode shapes that were actually a combination of the first flexural and torsional modes. Since the individual modes could not be adequately distinguished from each other (especially using harmonic loading), the first flexural mode was selected as being of primary importance. Steps were taken to suppress the effects of the first torsional mode, and magnify those of the first flexural mode, as described in Section 3.6.3.

3.6.3. Methods for Accentuating the First Flexural Mode

Two methods were used to amplify the response of the first flexural mode. First, the response of the first flexural mode was increased by exciting the bridge at its centre while using the hydraulic shaker. Since the centre of the bridge was a theoretical nodal point (point of zero displacement) for the first torsional mode, harmonic or impact excitation applied at the centre of the bridge would not be effective in exciting torsional motion. It should be noted that uniform weight was also added at this time (described in

Section 3.7.4) to model the effect of superimposed mass on the timber bridge, which was unrelated to accentuating the first flexural mode.

The placement of the hydraulic shaker mass at the centre of the bridge, in turn, also allowed for considerable energy transfer to the first torsional mode (alternatively, to the outer girders). In other words, the addition of the shaker mass made it relatively easier to excite the torsional mode since the flexural mode became more difficult to excite (the shaker mass was placed at a location with considerable movement for the first flexural mode). Consequently, additional mass was also added at mid-span of the outside girders to replicate the effect of the shaker mass on the middle of the outer girders, which further separated the natural frequencies by lowering the torsional natural frequency. The resulting change in the frequency response spectrum is shown in Figure 3.9, where the bridge was now subjected to superimposed mass (a more in-depth description of the mass on the bridge is provided in Section 3.7.4). Note the reduction of torsional amplitude, in addition to the increased separation of the modes, shown in Figure 3.9 as compared to Figure 3.8.

By amplifying the response of the first flexural mode relative to that of the lowest torsional mode, there was a considerable decrease in the quality of the first torsional mode shape results. Similar to “operational deflection shapes” described in Section 3.6.2, further attempts to plot the torsional mode shape resulted in anomalies in both the girder amplitudes and phase angles, thus resulting in a torsional mode shape that could not be used for further analysis. As a result, only the lowest flexural mode is considered in subsequent analyses.

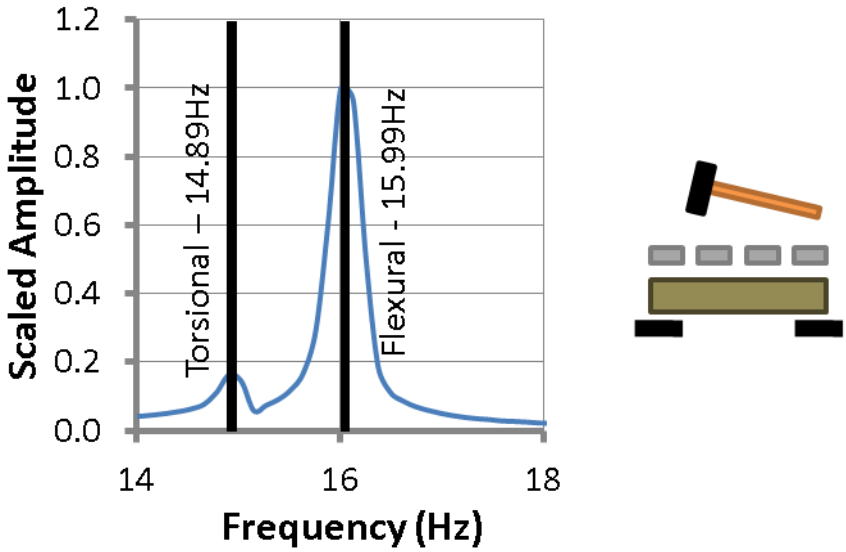

Figure 3.9. Partial frequency spectrum for the reference accelerometer obtained using impact excitation after the torsional mode was suppressed

3.7. DAMAGE CASES CONSIDERED

3.7.1. Overview

The primary purpose of this study was to determine the effect of changes in substructure stiffness on dynamic characteristics. As such, this section summarizes the work that was done to determine realistic pile head stiffness values, taking into account the soil-pile interaction. Upper and lower bounds on pile stiffness were considered, along with various soil stiffness values, to obtain a realistic range of effective foundation stiffness characteristics. Support conditions intended to reproduce this range of effective foundation stiffness were then applied under the timber bridge in the laboratory to allow for testing under a variety of substructure condition states.

In addition, it was of interest to determine the influence of superimposed mass (ballast) distributed over the timber deck, as well as superstructure damage. These variables and the cases considered are also presented in this section.

3.7.2. Determination of Substructure Stiffness

The effective substructure stiffness (k_{eff}) of a timber pile is a combination of the stiffness of the pile above ground (pile stiffness, k_p) arranged in series with the portion of pile located below ground, having a soil-pile stiffness of k_s. Equation 3.1 and Figure 3.10 show the field conditions that the supports used in the laboratory tests were intended to model:

$$\frac{1}{k_{eff}} = \frac{1}{k_p} + \frac{1}{k_s} \qquad [3.1]$$

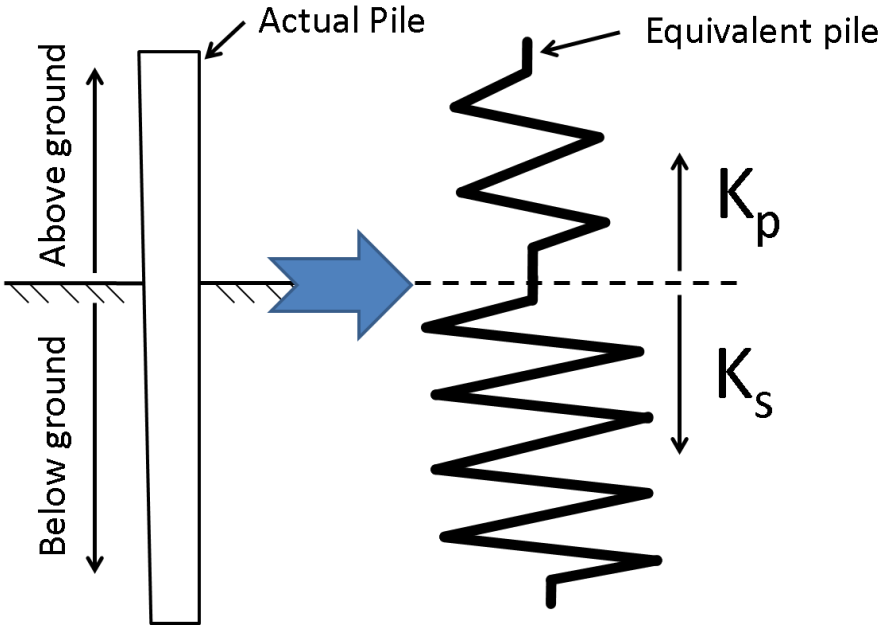

Figure 3.10. Effective stiffness model by considering the soil-pile interaction of an embedded timber pile

The pile stiffness above ground can be estimated as the stiffness of an axially loaded column, which can be expressed as

$$k_p = \frac{AE}{L} \quad [3.2]$$

where L is the length of pile above ground, E is the modulus of elasticity of the timber pile and A is the cross sectional area of the pile. However, Equation 3.2 assumes that a pile acts as a linear material, which is not likely the case, as shown in Figure 3.11. Timber, when exposed to the environment and service loads, is susceptible to reductions in strength and stiffness due to fatigue, increased moisture content and decay (Ritter 1990). For example, initial stiffness at low loads can decrease considerably with increased moisture content (Martenson 2003). During vibration testing, a bridge and its supporting piles are expected to be at low service loads, meaning that the pile stiffness may be considerably lower than that described in Equation 3.2 due to the increased timber flexibility caused by the variables listed above (fatigue, increased moisture content and decay). As such, to determine pile stiffness values at service level loading, data from a past study were used (Donovan 2004). In this study, 33 creosote treated timber piles gathered from across the United States were tested to failure and the load-deflection curves were tabulated. The researchers noted a typical non-linear behaviour, where the pile stiffness at higher loadings, prior to failure, was considerably higher than the service load stiffness, which is conceptually shown in Figure 3.11.

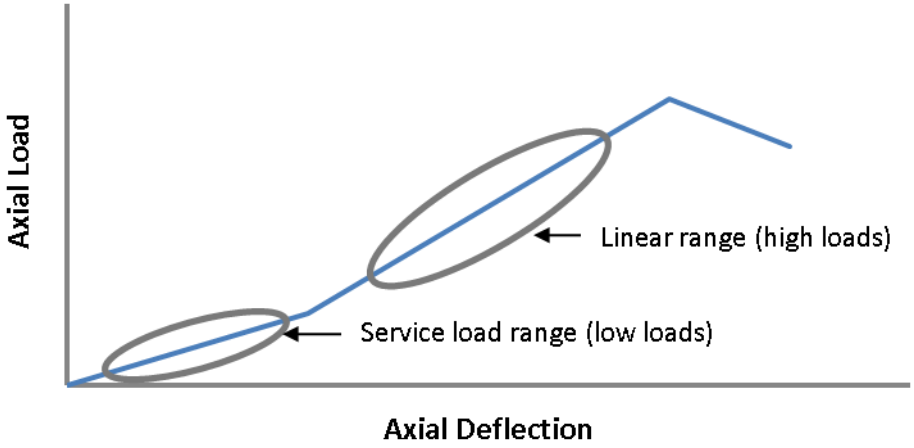

Figure 3.11 Typical applied load vs. average axial deflection behaviour for a timber pile with highlighted low and high load pile stiffness (after Donovan 2004)

A summary of the pile stiffness ranges are shown in Figure 3.12, where the x-axis represents the pile stiffness at high loadings (when a linear load-deflection curve is reached) and the y-axis represents the pile stiffness at a lower load (when the pile still behaves as a non-linear material). Note that the service level stiffness is approximately 0.22 that of the linear region at higher loadings, as indicated by the line of best fit through the data (the linear fit was set to have an intercept of zero). Figure 3.12 also provides upper and lower boundaries for expected above ground pile stiffness for piles in the field. A range of 20-90 kN/mm was selected to model realistic above ground pile stiffness in the field.

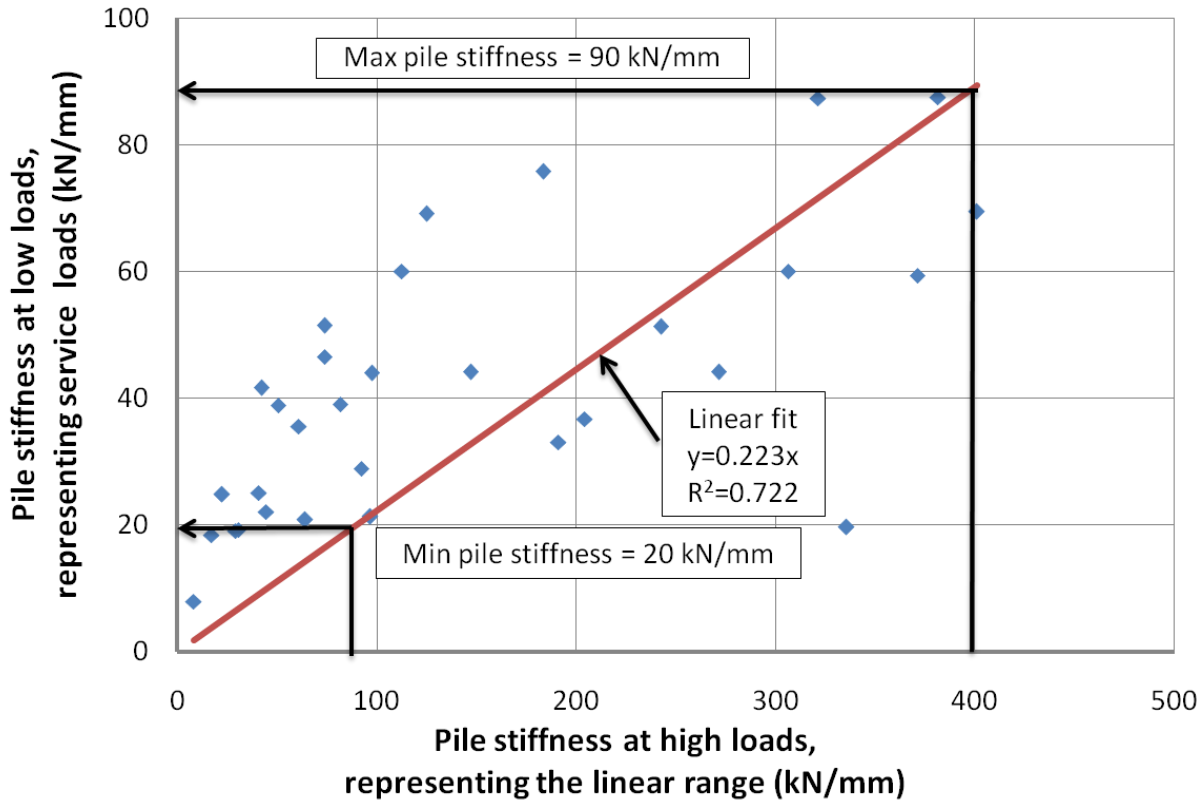

Figure 3.12. Low load pile stiffness vs. high load pile stiffness, showing a range of above ground pile stiffness, k_p (data from Donavan 2004)

To determine the deformation of a pile for the portion located below the ground, a method by Poulos and Davis (1980) was used, as outlined by Fleming et al. (2009). There are three types of settlement that were considered: (1) the base settlement, (2) the shaft settlement, and (3) pile compression. However, for service level loading, the shaft settlement governs, which is mainly a function of the modulus of rigidity of the soil. The stiffness of the pile-soil system below ground can then be solely attributed to shaft settlement and can be described as

$$k_s = \frac{2\pi L_s G}{\zeta} \qquad [3.3]$$

where L_s is the length of pile extending below ground, G is the shear modulus of the soil, and ζ describes the measure of radius of influence of pile (a function of the length of pile below ground and pile diameter, $\zeta \approx \ln[2L_s/d]$).

Considering Equation 3.3, common values for pile dimensions below ground, and a range of common soil elastic moduli (U.S Army Corps of Engineers 1990), the soil-pile system stiffness range is shown in Figure 3.13 (30-160 kN/mm). Note that the relationship between shear modulus and modulus of elasticity is $G = \frac{E}{2(1+\nu)}$.

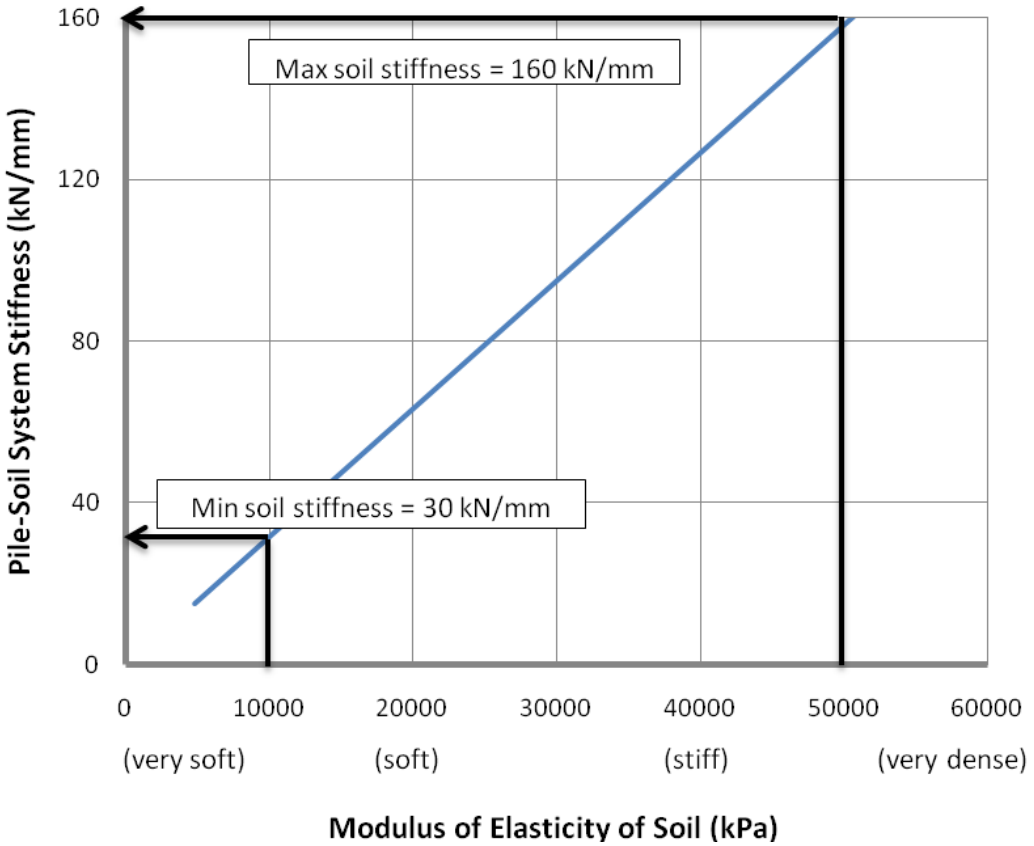

Figure 3.13. Range of soil-pile system stiffness below ground, k_s

Using the ranges of soil-pile system stiffness below ground (k_s), the above ground pile stiffness values (k_p) that were selected, and considering springs in series (Equation 3.1),

an effective stiffness for the soil-pile system could then be calculated. The results are shown in Table 3.3.

Table 3.3. Foundation stiffness window (per pile)

	Hard (kN/mm)	Soft (kN/mm)
k_s	160	30
k_p	90	20
k_{eff}	58	12

Once the upper and lower stiffness bounds were calculated, the range had to be implemented on the timber bridge substructure in the lab. The substructure setup used in the lab is shown in Figure 3.14. This figure illustrates how wood blocking was used to achieve the desired stiffness values. A steel block was fastened to the underside of the pile cap to uniform bearing for all condition states. Pine and oak blocks were then placed underneath the steel blocks to represent different substructure condition states.

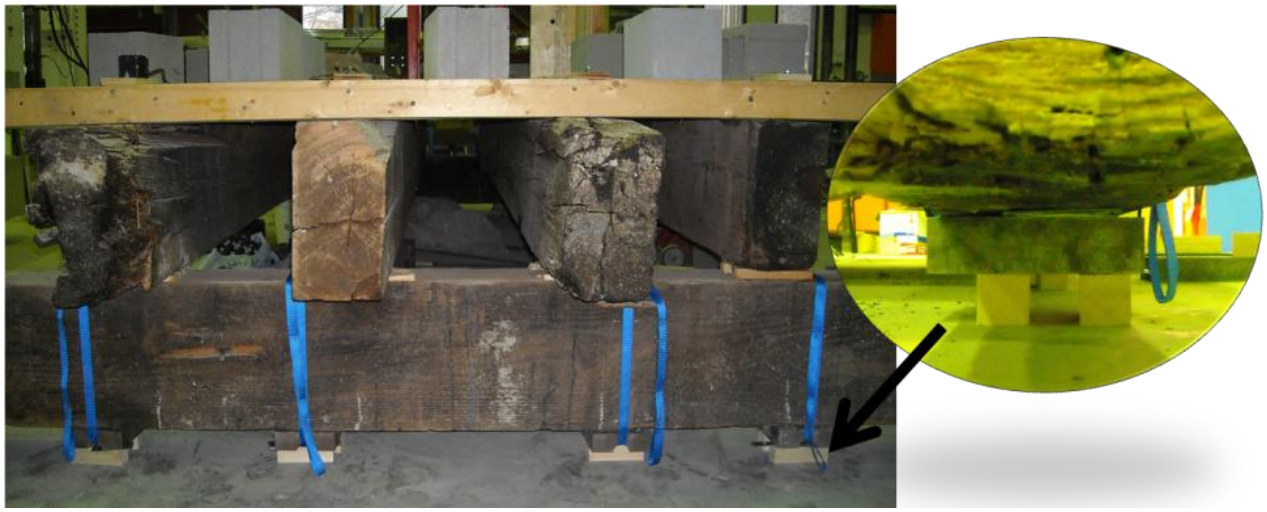

Figure 3.14. Wood block support setup (front and side views)

To ensure the effective stiffness values of the modelled supports were compatible with those shown in Table 3.3, stiffness testing was done on the wood block supports. Each pile was modelled as two wood blocks placed side by side, each with dimensions of 50 mm x 50 mm x 150 mm. Using a Universal Testing Machine (Instron 600DX), two wood blocks were compressed to a load of 5 kN with a loading rate of 5 kN/min. The test setup is shown in Figure 3.15. The wood blocks were sandwiched between two steel blocks to simulate their configuration under the pile cap in the laboratory. Two dial gauges were placed, one on either side of the specimen, to measure the small displacements (precision of ±0.0025 mm or 0.0001 in) and to ensure uniform distribution of the load.

Figure 3.15. Test setup to determine support stiffness

The load deflection curve was plotted using the load gauge (read to a precision of ±4.45 N) from the Universal Testing Machine and the deflection gathered with dial gauges. Readings were taken every 0.013 mm (0.0005 in) for the oak block tests, and

every 0.051 mm (0.002 in) for the pine tests. Each oak block and pine block configuration was repeated for three trials (each with different wood blocks), and the data points are plotted in Figure 3.16. A line of best fit was then applied to each test (using least squares and intercept of zero) to attain an overall stiffness for each trial. The stiffness values (slopes) produced for similar block cases were then averaged and are plotted in Figure 3.16, where the slope represents the stiffness of the block system. Also, a confidence interval (α=0.1) was calculated using the average and standard deviation of the slopes/stiffness from the three tests. It can be seen that the pine foundation closely models the "soft" foundation, and the oak models the "hard", as presented in Table 3.3.

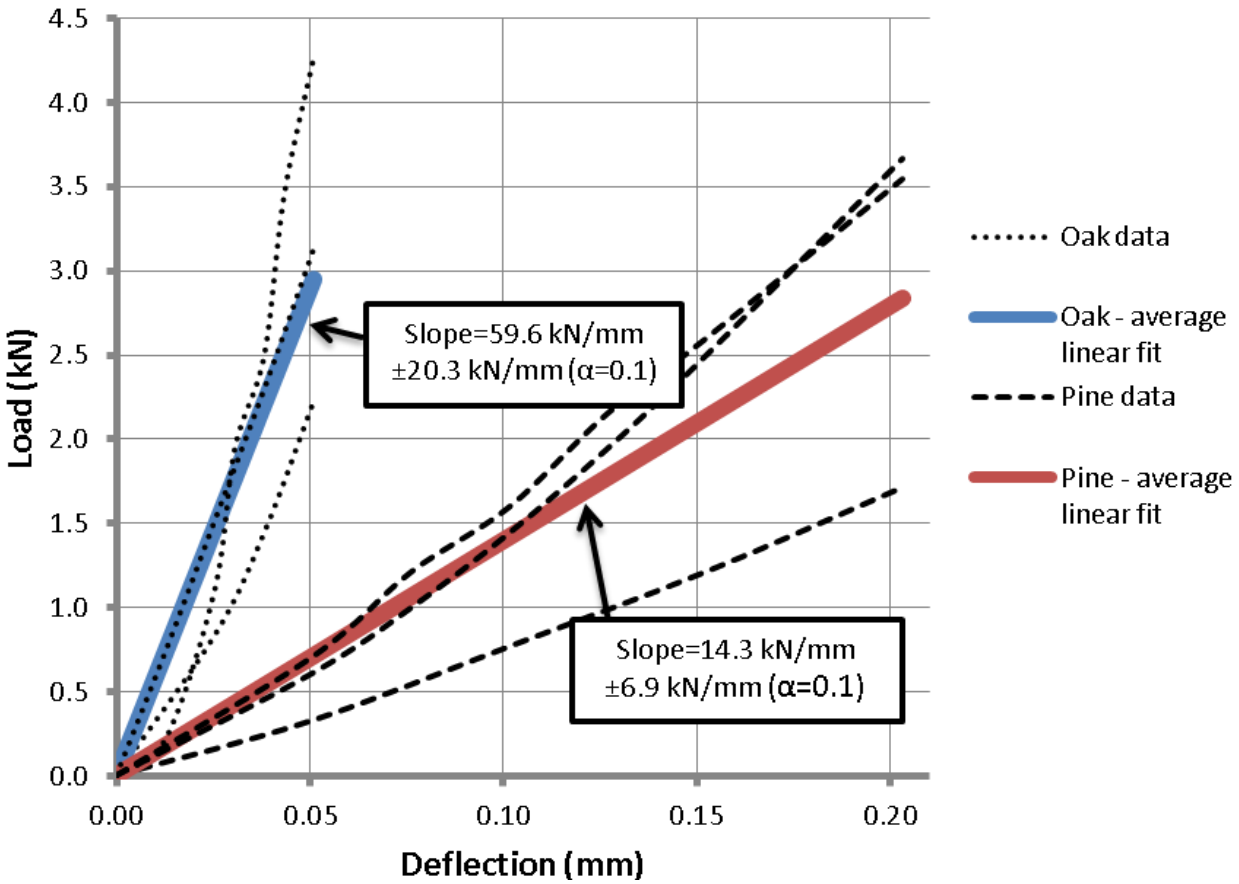

Figure 3.16. Pine and oak block foundation load deflection curve (per support)

Refer to Appendix B for more details on the calculations and data used to complete this section.

3.7.3. Substructure Damage Cases

A summary of the substructure condition states can be seen in Table 3.4.

Table 3.4. Substructure condition states

Condition State	Graphic	Description
D0		Rigid-Rigid Both ends of the bridge were supported by four sets of steel blocks.
D1		Hard-Rigid The left support was “hard” (four sets of oak blocks) and the right support was rigid.
D2		Soft-Rigid The left support was “soft” (four sets of pine blocks) and the right support was rigid.
D3		Non-Uniform-Rigid The left support was “soft” under Girders 3 and 4 (two sets of pine blocks) and rigid under Girders 1 and 2 (two sets of steel blocks), while the right support was rigid.
D4	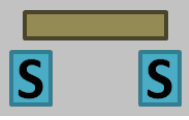	Soft- Soft Both sides of the bridge were uniform “soft” supports (four sets of pine blocks under each pile cap).
D5	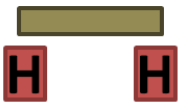	Hard- Hard Both sides of the bridge were uniform “hard” supports (four sets of oak blocks under each pile cap).
D6		Soft- Hard The left support was “soft” (four sets of pine blocks) and the right support was “hard” (four sets of oak blocks).

A “rigid” case was used as the base case, and exhibited a stiffness exceeding that which would be expected in the field. The “hard” foundation case represented the stiffness of a healthy pile in stiff soil, and the “soft” foundation case represented a deteriorating pile in soft soil. In all condition states, with the exception of D3, the

foundation had a uniform stiffness under either pile cap, meaning that each of the four supports under a pile cap were similar. There were a large number of foundation cases that could have been examined; however, the six foundation cases shown in Table 3.4 represent the scope of this study.

3.7.4. Weight Cases

The mass of a system can influence the dynamic response significantly. The weight cases considered in this study were meant to take into account the variability in the weight of the wearing surfaces that would occur in the field. The bare timber bridge in the laboratory had a total mass of 1630 kg, which corresponded to a uniform dead load of 1.11 kPa distributed over the surface area. To determine the mass of the timber bridge, the density was first calculated by weighing a 0.227 m^3 potion of the bridge (having a mass of 116 kg). The total mass of the bridge was then extrapolated using the calculated density of 510 kg/m^3 and an approximate volume of 3.2 m^3 (not including the pile caps).

To increase the weight of the bridge to account for a percentage of the wearing surface that would be present in the field, concrete blocks were placed on the deck surface. The blocks were approximately uniformly distributed; however, additional blocks were placed at the centre of the outer girders (Girders 1 and 4) for reasons described in Section 3.6.3. The distribution of the blocks and the two weight cases considered can be seen in Figure 3.17. Weight Case 1 (W1) provided an additional load of 0.27 kPa over the bare timber bridge deck. To attain Weight Case 2 (W2), a single concrete half block was placed on top of each of the concrete blocks shown in Figure 3.17. Weight Case 2

resulted in an additional 0.41 kPa over the bare timber bridge deck. The two weight cases presented were not intended to represent realistic weights that would be seen in the field, but it is possible that they reduced the effects of non-linear behaviour by pre-loading the structure. Furthermore, to realistically model the mass of a wearing surface that would be present in the field, significantly more blocks would be required, which would have introduced significant tripping hazards to the bridge surface.

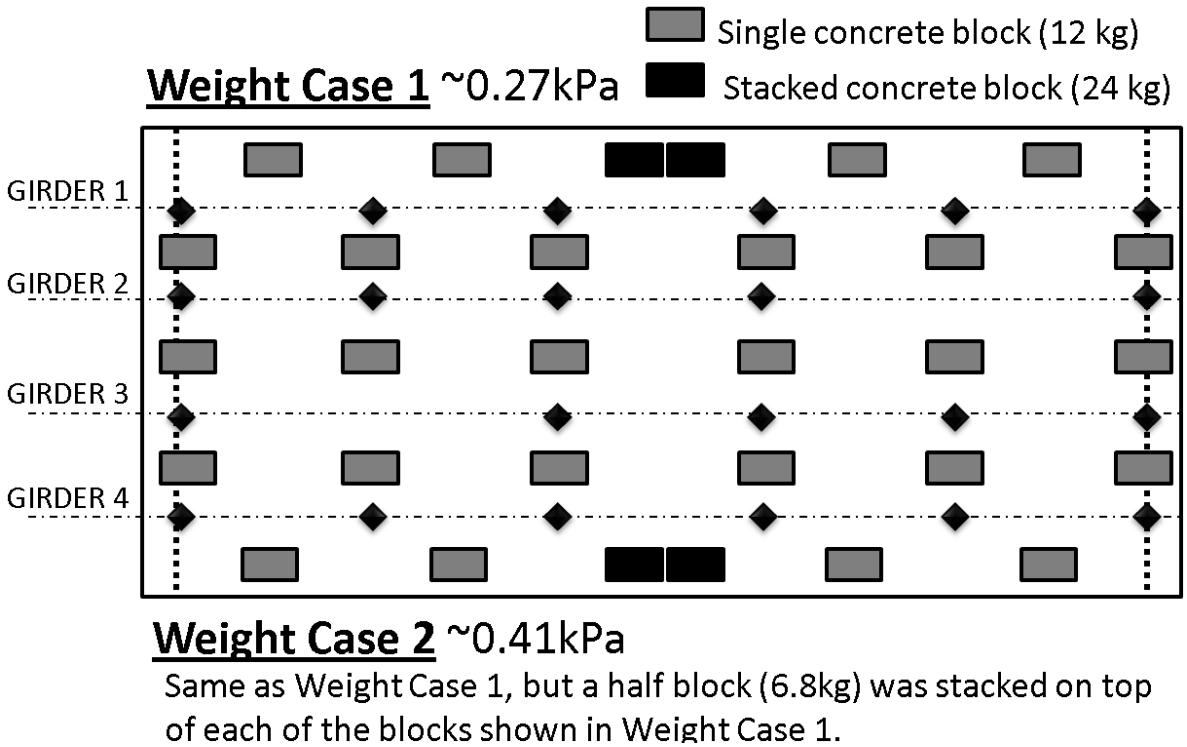

Figure 3.17. Plan view of the deck, showing the distribution of concrete blocks used to produce the two weight cases

Figure 3.18 shows the timber bridge in the laboratory loaded to Weight Case 1. The additional blocks over the outer girders can be seen clearly. These blocks were placed to offset the effects of the weight of the hydraulic shaker at the centre of the bridge, thereby suppressing the effects of the first torsional mode and accentuating a response at the first flexural mode shape (described in Section 3.6.3).

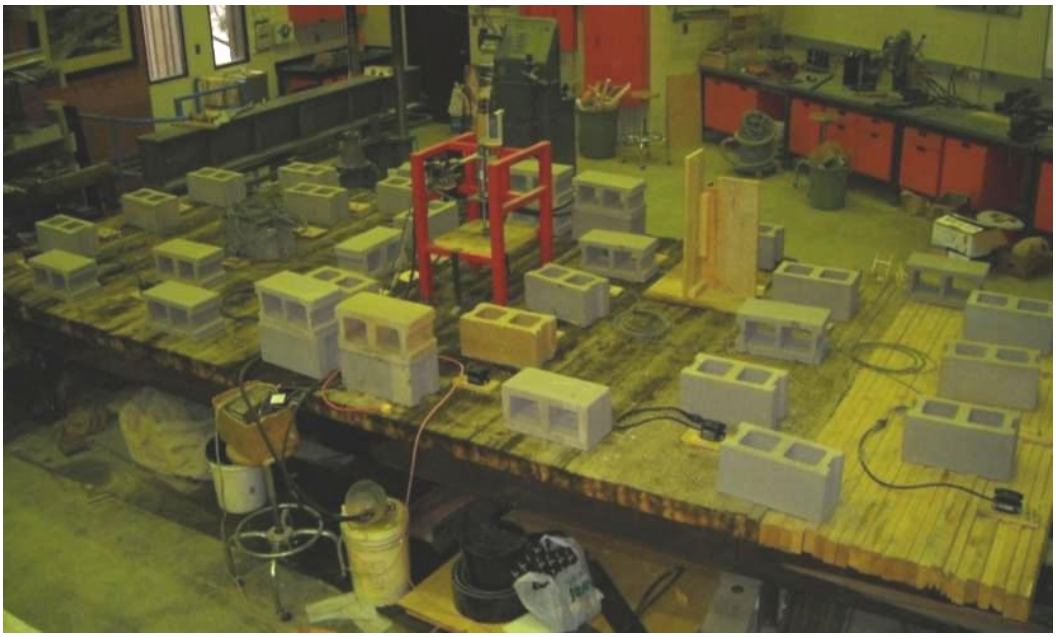

Figure 3.18. Timber bridge loaded with Weight Case 1 (W1)

A summary of the weight cases is provided in Table 3.5.

Table 3.5. Summary of the weight cases considered

Condition state	Graphic	Description
W1	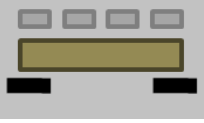	Weight Case 1 Represents ~10 mm gravel wearing surface. The mid-span of the two outside girders was more heavily loaded to separate the first torsional and flexural mode.
W2	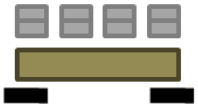	Weight Case 2 Represents ~15 mm gravel wearing surface. The mid-span of the two outside girders was more heavily loaded to separate the first torsional and flexural mode.

3.7.5. Superstructure Damage Cases

Superstructure damage cases were limited to reductions in flexural rigidity. A skill saw was used to make a 60 mm deep cut on the bottom of Girder 2 (Damage Case S1) and subsequently to Girder 4 (Damage Case S2). These condition states are shown in Table 3.6.

Table 3.6. Superstructure condition states

Condition state	Graphic	Description
S0	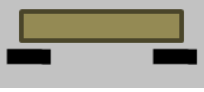	Baseline Condition This was the base case for the timber bridge in the laboratory.
S1	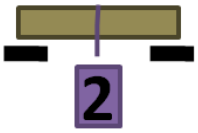	Flexural cut beneath Girder 2 60 mm deep cut beneath Girder 2 at mid span (2700 mm from the left support). The cut was made with a skill saw and reduced the girder moment of inertia to 62% of the original (not considering composite action with the deck).
S2		Flexural cut beneath Girder 4 60 mm deep cut beneath Girder 4 at 1/3 the span (1890 mm from the left support). The cut was made with a skill saw and reduced the girder moment of inertia to 62% of the original (not considering composite action with the deck). This cut was made after S1

3.8. SUMMARY OF THE EXPERIMENTAL PROGRAM

3.8.1. Overview

This section summarizes the specific damage states and tests that were completed for this experimental program. This includes the different combinations that were examined using two excitation sources and various condition states. A summary of the bridge setups that were tested is shown in graphic format in Figure 3.19, which presents the graphics and the text notation used to represent different bridge configurations and excitation sources that are used for the remainder of the thesis. The bridge state D0S0W1 represents an undamaged lightly loaded bridge on rigid supports, and was used as a baseline for comparison to all other damage states. In the notation adopted for this study, the first two characters (D0 to D6) denote the support condition state, the second two characters (S0 to S2) denote the superstructure condition state, and the final two characters (W1 to W2) denote the super-imposed mass on the timber bridge

deck. All tests were run using both harmonic loading and impact loading, using the average of five repeated tests.

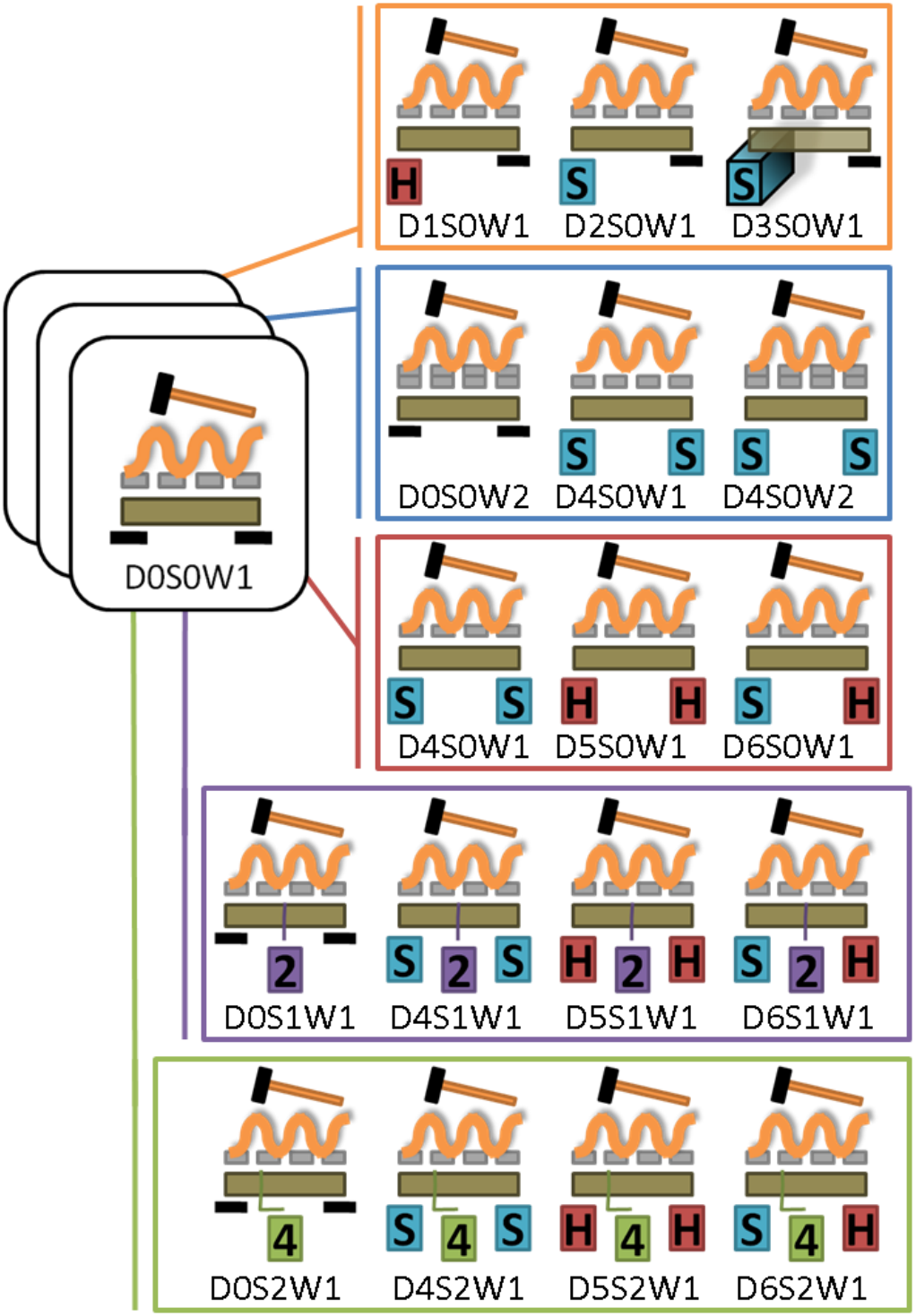

Figure 3.19. Summary of experimental program

3.8.2. Substructure Damage Program

The substructure damage program was completed to investigate the influence of the substructure stiffness alone on the dynamic response of the bridge. This phase consisted of four test setups, D0S1W1$_a$, D1S0W1, D2S0W1, and D3S0W1. The subscript ‘a’ signifies that this test setup was subsequently used again, but the supports were changed for other testing in-between.

3.8.3. Weight Case program

The weight case program considered changes to the weight on the timber bridge in conjunction with changes to the substructure stiffness. This was conducted to uncover the influence the super-imposed mass had on the dynamic response. This phase consisted of four bridge arrangements, D0S0W1$_b$, D0S0W2, D4S0W1$_a$, and D4S0W2. Note that base case, D0S0W1, had to be re-established to carry out this phase (signified by the subscript ‘b’).

3.8.4. Substructure and Superstructure Interaction Program

The final testing program was conducted to determine the effects of superstructure damage alone on the timber bridge response. Additionally, the interaction of superstructure damage with substructure damage to both supports was of interest. The testing program considered many damage states, which consisted of D0S0W1$_c$, D4S0W1$_b$, D5S0W1, D6S0W1, D0S1W1, D4S1W1, D5S1W1, D6S1W1, D0S2W1, D4S2W1, D5S2W1, and D6S2W1. The process for testing was to cycle through substructure states, then to introduce superstructure damage, and then re-establish the dynamic properties considering all substructure states again.

4. TIMBER BRIDGE DAMAGE DECTECTION RESULTS

4.1. INTRODUCTION

This chapter presents the results of the timber bridge damage detection program described in Chapter 3. Forms of damage investigated included both substructure and superstructure damage. As well, the influence of superimposed weight added on top of the bridge deck was considered to investigate possible nonlinear effects associated with the closing of cracks in the timber. Changes in dynamic response were studied primarily using comparisons of the first flexural mode shape, but changes in the fundamental natural frequency were also considered.

The primary objective of this study was to investigate the feasibility of detecting realistic changes in substructure stiffness using vibration-based methods, in addition to studying the interaction between the substructure and superstructure responses.

4.2. BRIDGE BEHAVIOUR

4.2.1. Overview

The overall bridge response to dynamic excitation is presented in this section. Characteristics of the first flexural mode are presented in the most detail, including its associated natural frequency and mode shape.

The data gathered using both harmonic and impact excitation methods are presented, and the advantages and disadvantages of both methods are considered. In addition, the two methods for normalizing the measured mode shape are compared and contrasted.

4.2.2. Dynamic Response

The modes that were most easily excited on the timber bridge were the lower modes, which included the first flexural and torsional modes. Figure 4.1 presents the acceleration spectrum produced by the reference accelerometer due to impact loading; here, the greatest spectral amplitude for the reference accelerometer has been scaled to unity. The bridge configuration for the data presented in Figure 4.1 was the initial bridge state after the steps were taken to separate the lower modes, as presented in Section 3.6.3. The first flexural mode was of particular interest for this study because of the ease with which it could be excited and the fact that the lowest mode has been proven in past studies to provide the most reliable indications of damage (Zhou 2006; Wang et al. 2009).

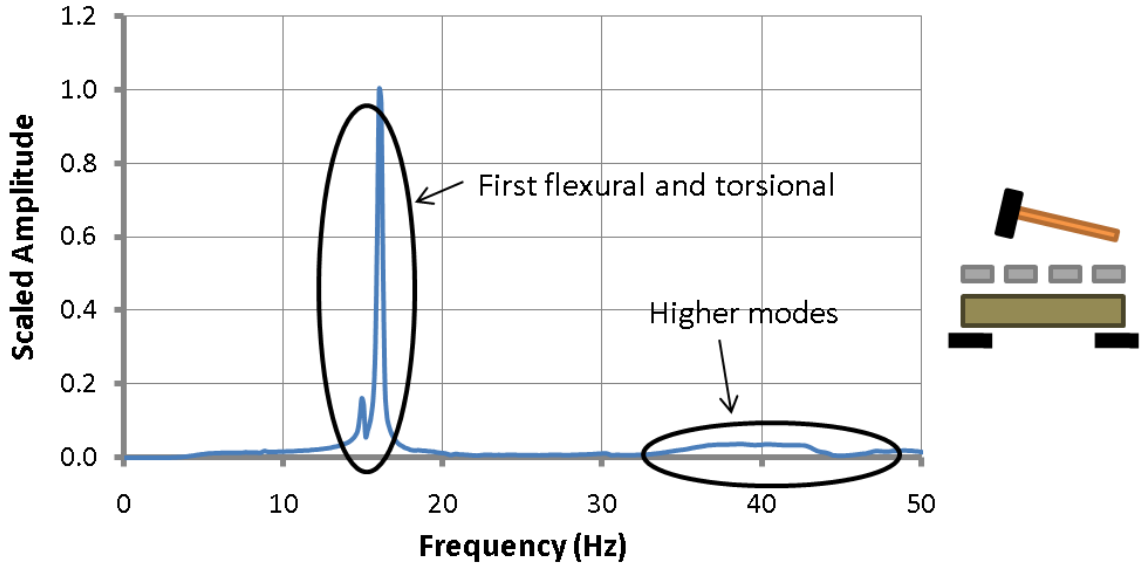

Figure 4.1. Frequency spectrum of the reference accelerometer for foundation case **D0**S0W1$_a$ using impact loading

Figure 4.2 presents the first flexural mode shape for the base condition state (D0S0W1$_a$) produced with impact loading. The mode shape has been bridge-normalized (see Equation 2.4 and Section 3.5.3), so the relative amplitudes of different girders could be preserved.

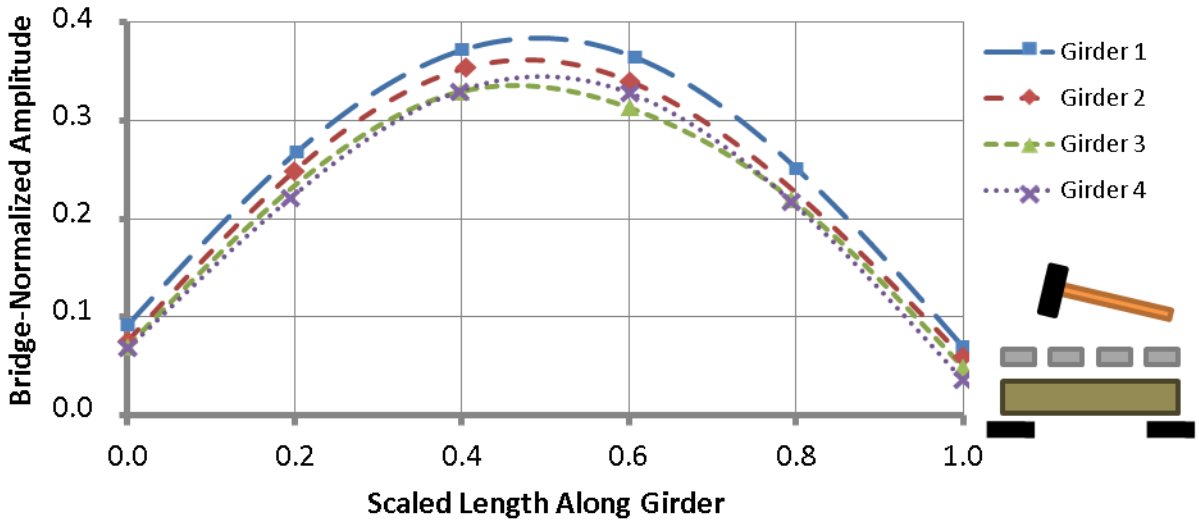

Figure 4.2. First flexural mode shape for foundation case **D0**S0W1$_a$, obtained using impact loading

The left support was then changed from rigid to the hard foundation case (D1S0W1); the mode shape for this case is presented in Figure 4.3. Again, the mode shape was bridge-normalized and was produced using impact excitation. It is important to note that, for the stiffer foundation cases presented in Figure 4.2 and Figure 4.3, the amplitude of girder movement across the bridge deck remained relatively constant.

Upon changing the left support to a “soft” condition, there was a definite change in the first flexural mode shape produced, as seen in Figure 4.4. A difference in the relative girder movement across the bridge is observed when the more flexible substructure was introduced. Girder 4 was found to have the largest deflections, with deflections

decreasing continuously to Girder 1. This change in the mode shape pattern may be attributed to either non-uniform substructure stiffness, resulting in local changes to the bridge movement, or to torsional influences in the first flexural mode shape.

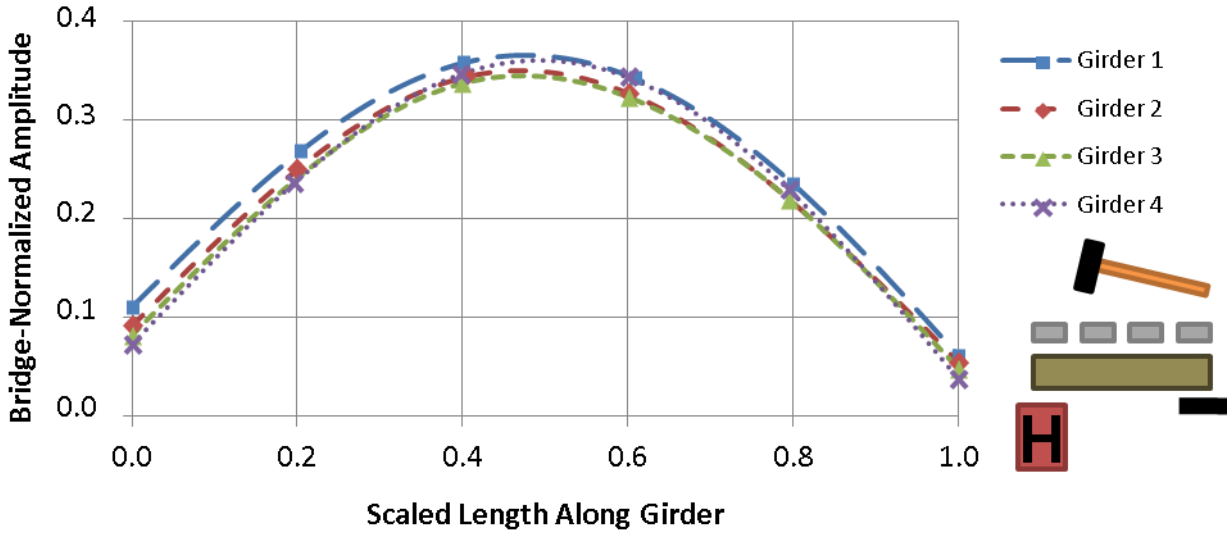

Figure 4.3. First flexural mode shape for foundation case **D1**S0W1, obtained using impact loading

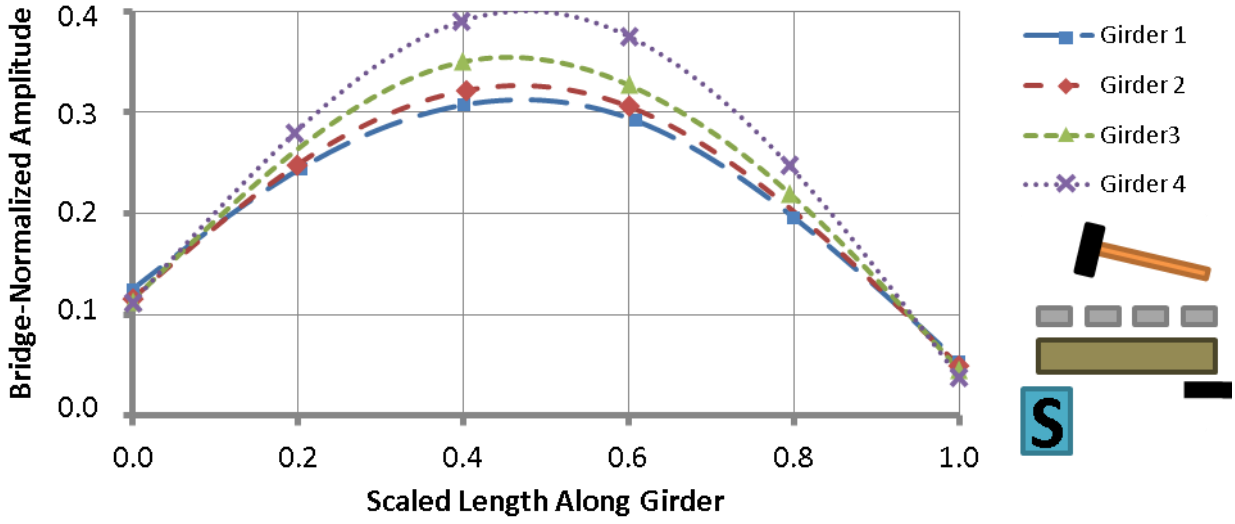

Figure 4.4. First flexural mode shape for foundation case **D2**S0W1, obtained using impact loading

The bridge behaviour that is seen Figure 4.4 is similar to the mode shapes that were produced in the preliminary work presented in Section 3.6.2 before measures were taken to separate the lowest flexural and torsional modes. Figure 4.5 shows the frequency spectrum over the frequency range covering the lowest two modes for the foundation cases presented in the above figures (D0S0W1$_a$, D1S0W1, and D2S0W1). It can be seen that, as the timber bridge substructure was incrementally softened, the separation between the lower modes became smaller. As such, the interaction between the two modes became greater, and the first flexural mode increasingly began to resemble the torsional mode, as seen in Figure 4.4.

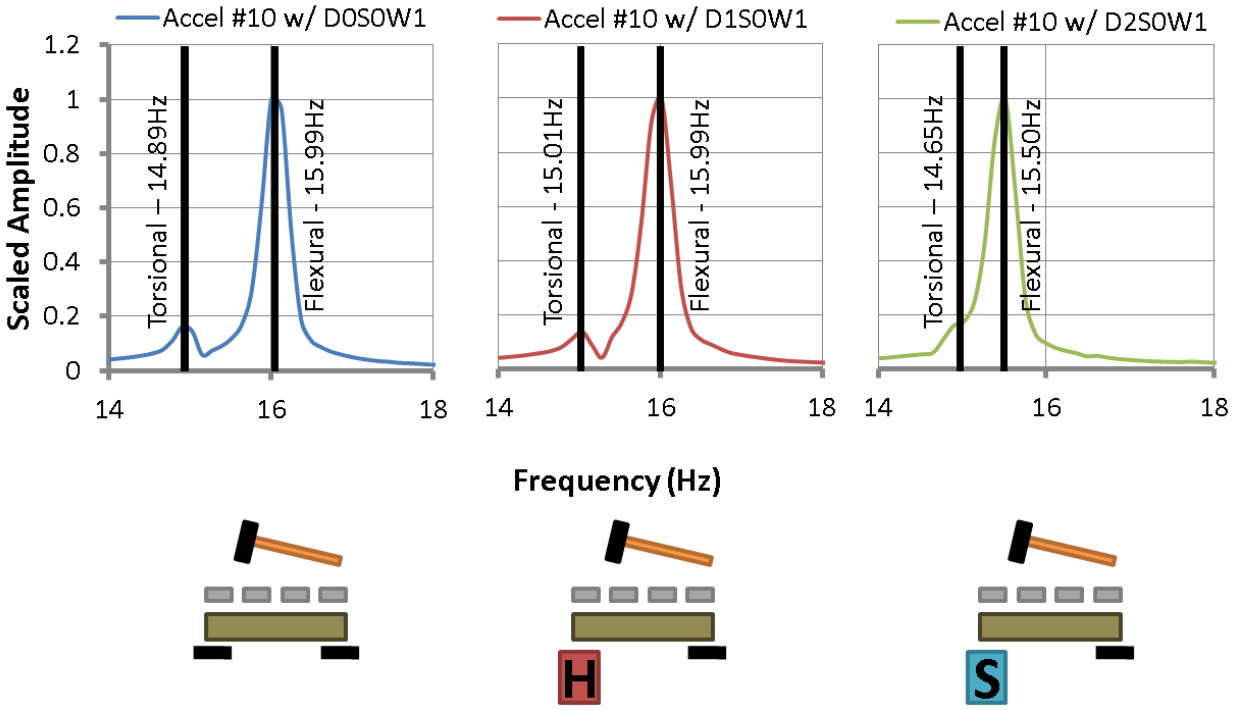

Figure 4.5. Acceleration spectra showing the first flexural and torsional natural frequencies under different damage states

The associated torsional mode shapes for the condition states presented could not be confidently identified due to their ambiguous nature. Rather, the girders on opposite sides of the bridge were neither fully in-phase nor completely out of phase, but rather somewhere in between. This suggests that the mode shape extracted was probably an "operational deflected shape" composed of the two lower modes.

4.2.3. Normalization

This section presents the rationale for the selection of the appropriate normalization method to use when presenting the various results in this study. Since mode shape amplitudes are arbitrary, the normalization process is required so that mode shapes can be directly compared. The two mode shape normalization methods that were considered for this study were bridge-normalization, and girder-normalization. The equations used to calculate the bridge-normalized mode shape (ϕ_{Bn}) and girder-normalized mode shape (ϕ_{Gn}) were as follows:

$$\phi_{Bn,i} = \frac{\phi_{o,i}}{\sum_{j=1}^{n} \int_0^1 \phi_{o,j}\, dx} \quad [4.1]$$

$$\phi_{Gn,i} = \frac{\phi_{o,i}}{\int_0^1 \phi_{o,i}\, dx} \quad [4.2]$$

where ϕ_o is the measured mode shape, for which the bridge span had already been scaled to one. The number of girders is represented by 'n', and 'i' represents a single girder on the bridge.

The bridge-normalization method produces a mode shape that encloses a unit-area under the entire bridge, while a girder-normalized mode shape encloses a unit-area under each individual girder. Furthermore, all girders in the bridge-normalization scheme have the same scaling factor, while each is different under girder-normalization, as shown in Equations 4.1 and 4.2.

Figure 4.6 illustrates the influence of the normalization scheme on a mode shape generated using pseudo data, which was fabricated to show the effects of normalization. It is clear that the bridge-normalization scheme maintains the relative girder amplitudes for the mode shape, so that each girder encloses a different area. The girder-normalization scheme, however, scales each individual girder to enclose an area of unity.

All figures presented in this chapter thus far were generated using the bridge-normalization method, where the relative girder amplitudes have been maintained to represent the actual motion of the bridge (see Figure 4.6a). To compare the two normalization schemes using measured data, Figure 4.7 presents the bridge-normalized mode shape for the soft foundation case (which is the same case as that plotted in Figure 4.4, but achieved through harmonic loading), while Figure 4.8 presents the same mode shape but generated using girder-normalization.

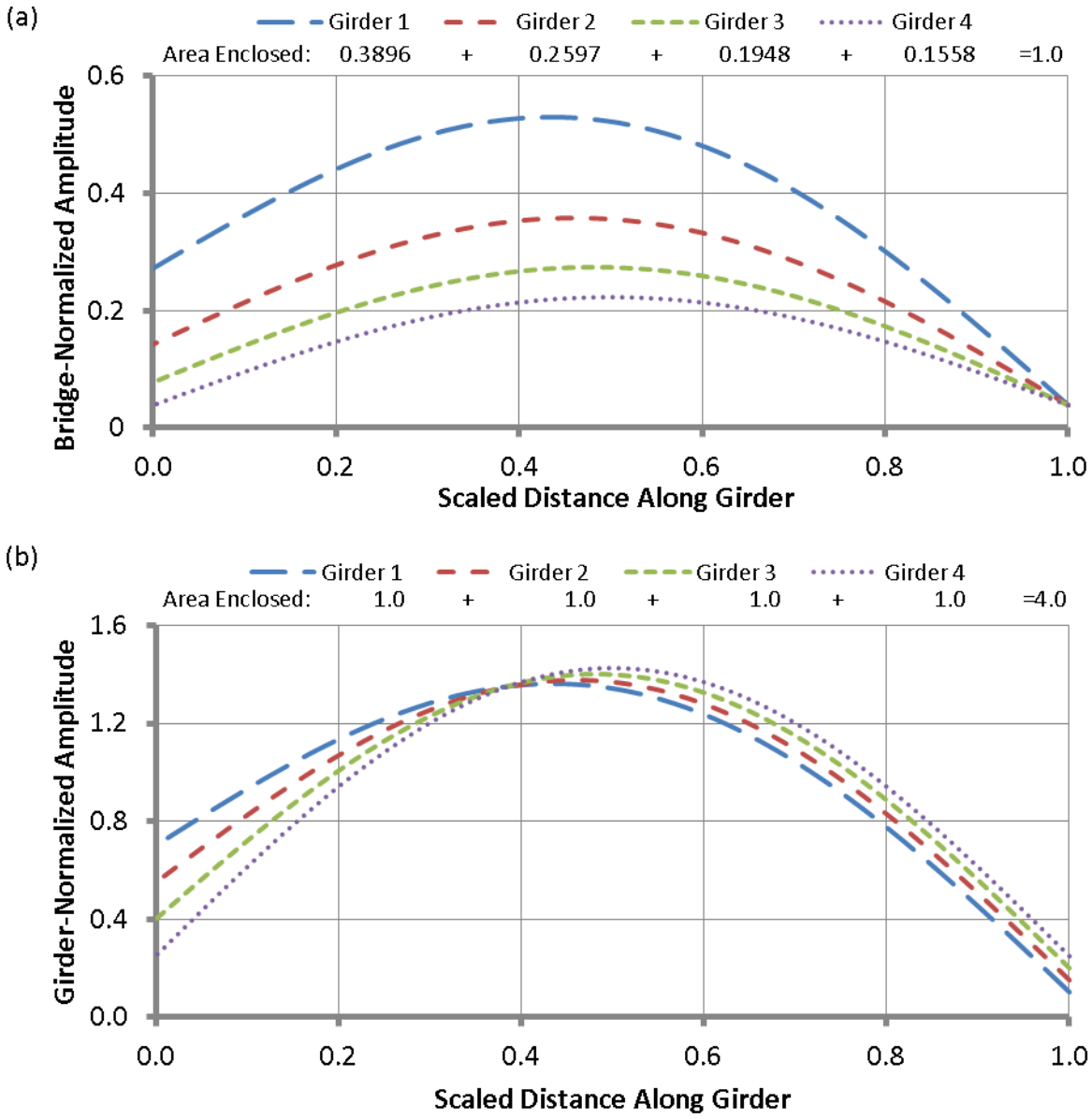

Figure 4.6. Representations of the same mode shape using the (a) bridge- and (b) girder-normalization schemes (generated using pseudo data)

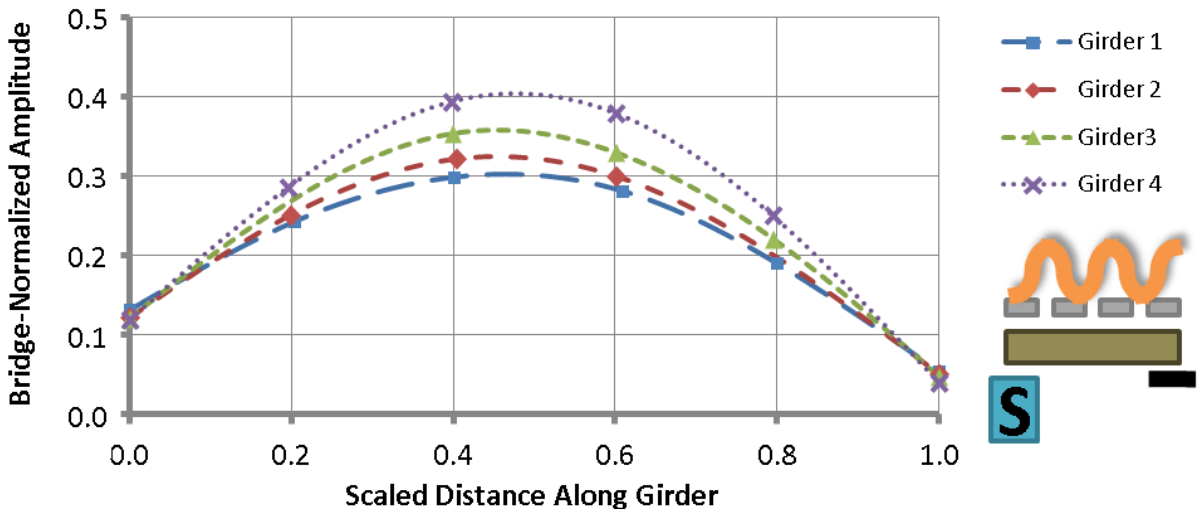

Figure 4.7. Bridge-normalized representation of the soft foundation case (**D2**S0W1)

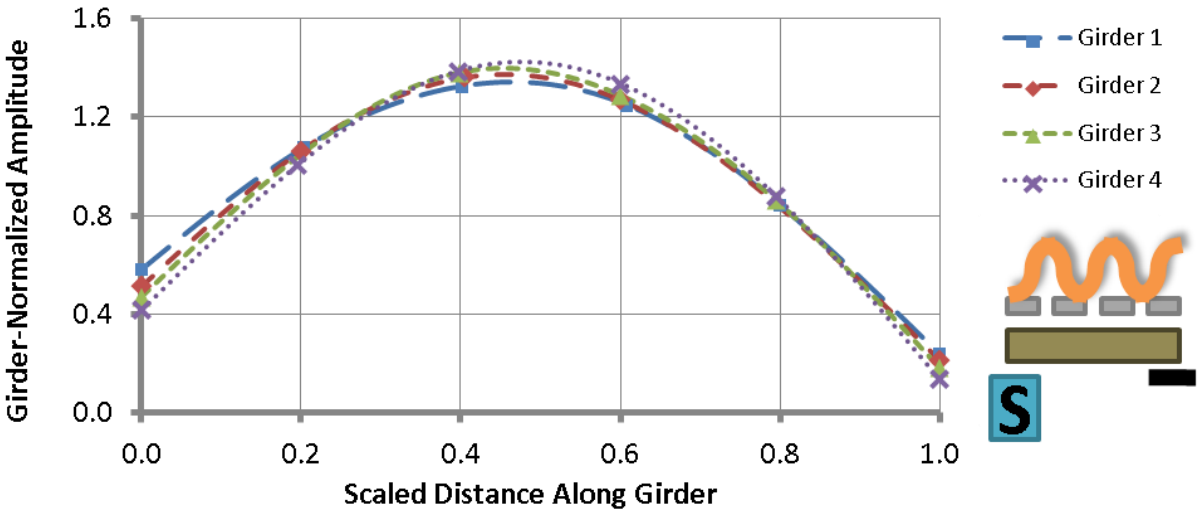

Figure 4.8. Girder-normalized representation of the soft foundation case (**D2**S0W1)

The girder-normalization method seems to attenuate the influence of torsional behaviour in the first flexural mode shape by scaling each individual girder mode shape to encompass a unit-area, thereby forcing the peak mode shape amplitude along each girder to be roughly equal and allowing for a more direct comparison between girders. Since this study focused on relative movements between the substructure and superstructure, rather than relative movement between girders, the girder-normalization

method was implemented for the remainder of the study. Consequently, the girder-normalization scheme also attenuated the influence of torsional behaviour.

4.2.4. Mode Shape Variability

The primary method of vibration-based damage detection used in this study was the comparison of the first flexural mode shapes for the bridge in different conditions. Damage was inferred using changes in the mode shape. Typically, small-scale damage results in minor changes to the mode shape. Consequently, the mode shapes need to be known to a high degree of certainty. Figure 4.9 shows the variability of the measured mode shape gathered by harmonic loading for the base case ($D0S0W1_a$). For this case, the resulting average coefficient of variation in mode shape amplitudes at various sensor locations was approximately 0.07% based on five repeated trials. This high degree of precision was found to be sufficient to enable the detection of small-scale damage.

The results for impact loading are shown in Figure 4.10. Here, there was considerably more variability, with an average coefficient of variation of approximately 0.69% in the mode shape amplitudes. As a result, it was more difficult to detect small-scale damage using impact loading due to the increased noise in the mode shape. However, impact loading is still considered to be of practical interest due to its ease of implementation in the field.

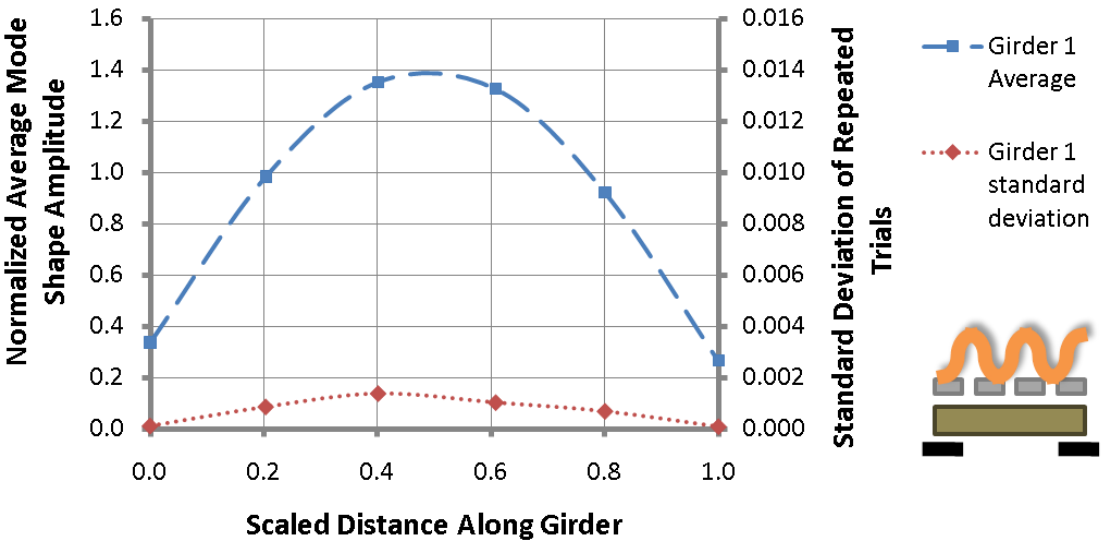

Figure 4.9. Variability of mode shape amplitudes for the base support case (D0) using harmonic excitation

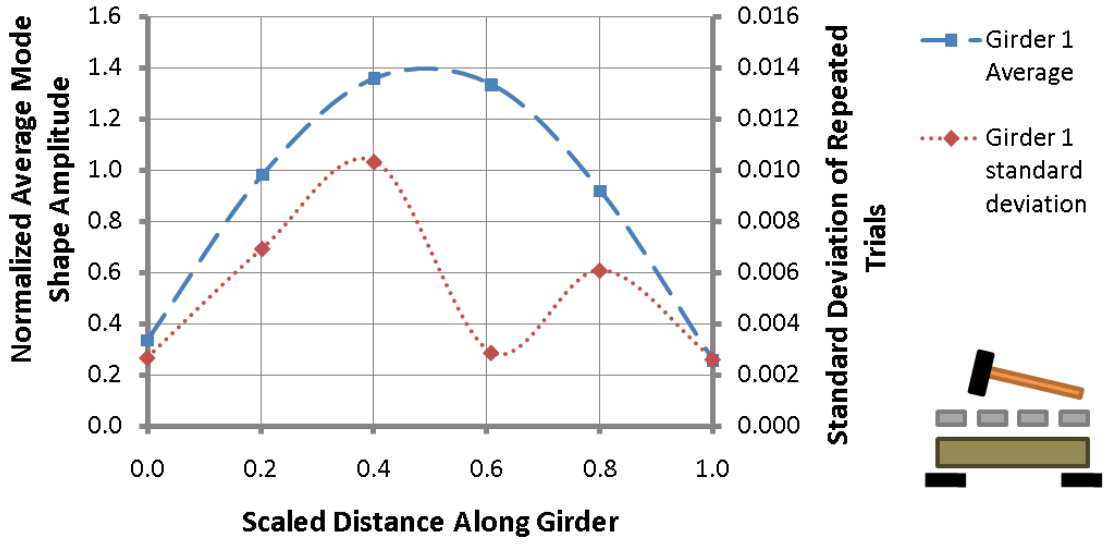

Figure 4.10. Variability of mode shape amplitudes for the base support case (D0) using impact excitation

Similarly, the natural frequencies produced using harmonic loading were found to a higher degree of certainty. In this study, the natural frequencies produced through harmonic loading were measured to a precision of ±0.05 Hz, while those measured using impact loading had lower precision at ±0.12 Hz.

4.2.5. Mode Shape Components

The mode shape of the bridge superstructure, supported on flexible supports, was broken down into the following three components, illustrated in Figures 4.11 to 4.13, to describe the bridge's response to vibration:

A. Flexural response: The flexural component (A) describes the area of the mode shape remaining once the substructure motion (components B and C) has been removed. This component corresponds to the movement of the superstructure when excited at its first flexural natural frequency.
B. Differential support movement: This component accounts for the portion of the substructure movement resulting from differential support stiffness. The contribution of this component can be described by the triangular area (B) representing the difference in support movement at the two ends of the girder. This component was defined as positive for cases where the left support had a greater amplitude and negative when the right support had a greater amplitude to ensure that the differential support movement was completely quantified with the differential component.
C. Uniform support movement: This component is defined by the smaller of the two mode shape amplitudes at either end of the girder (i.e., over the supports). Represented by area C, the uniform support movement may be caused either by the compressibility of the timber pile cap or by flexibility in the foundation below the cap.

The girder-normalized first flexural mode shape for the base case (Girder 1) is shown in Figure 4.11. The mode shape has been decomposed to separate the mode shape into

the three components. Similarly, Figure 4.12 and Figure 4.13 show the corresponding mode shape components for foundation cases with an incrementally softened left support. As the left support was incrementally softened, a definite change in the mode shape geometry may be noted. All figures were produced with harmonic excitation; however, impact loading gave similar results.

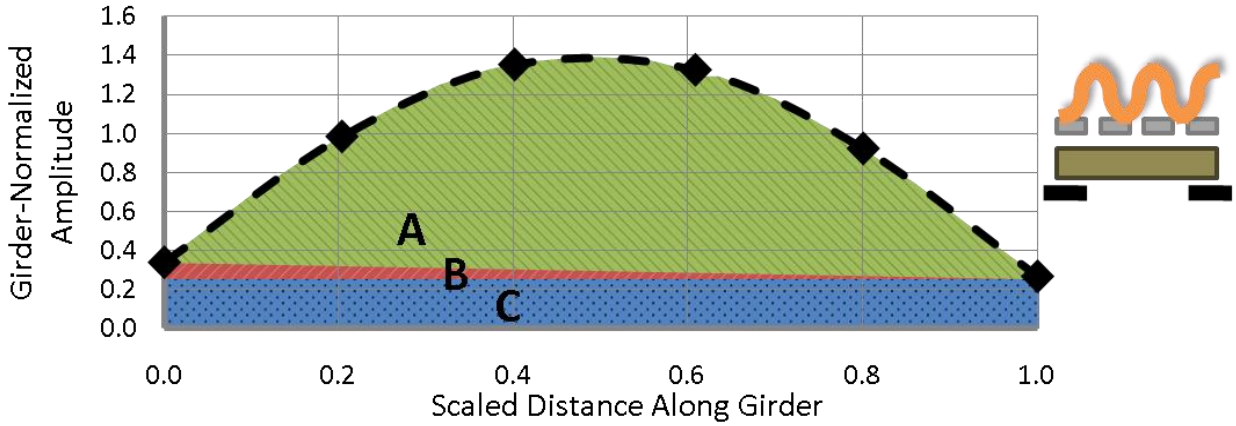

Figure 4.11. Mode shape of Girder 1 for foundation case **D0**S0W1 (harmonic excitation), subdivided into its three components

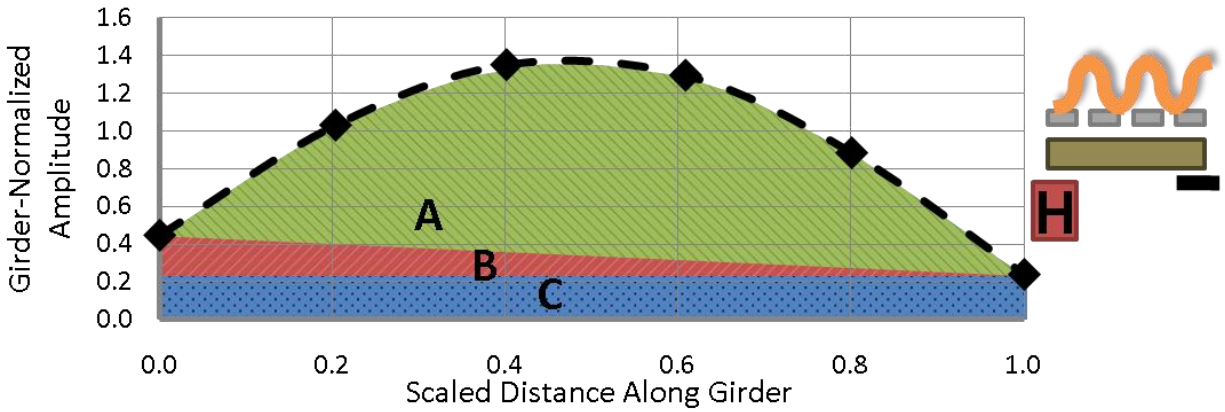

Figure 4.12. Mode shape of Girder 1 for foundation case **D1**S0W1 (harmonic excitation), subdivided into its three components

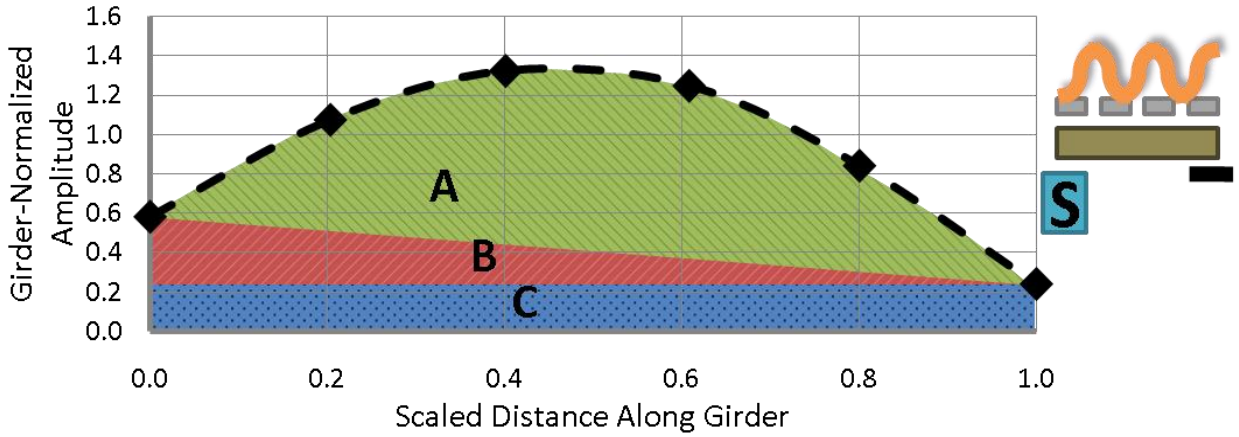

Figure 4.13. Mode shape of Girder 1 for foundation case **D2**S0W1 (harmonic excitation), subdivided into its three components

The mode shapes have been girder-normalized for the above figures and the remainder of the analysis for this study, unless otherwise noted. The girder-normalization ensured a unit-area under each girder, suggesting that the area under three components add to unity. In addition, the girder-normalization method allowed the contribution of each component for individual girders to be directly compared without regard to amplitude.

Figure 4.11 presents the mode shape of Girder 1 for the stiffest support case (base case); the mode shape is largely dominated by flexural deformations (A). Nevertheless, there is still considerable uniform support movement, C, which can be attributed to compression within the pile caps and the girder directly above the caps. As the left support is incrementally softened from Figure 4.11 to Figure 4.12 to Figure 4.13 it is apparent that the differential support movement, B, becomes relatively more prominent. This suggests that a simple observation of the relative contributions of the mode shape components can provide valuable insight into the condition of the substructure.

4.2.6. Summary

The bridge behaviour was governed by the first flexural mode shape; however, since the natural frequency of the torsional mode was close to that of the flexural mode there was some energy transfer to the torsional mode, resulting in difficulties extracting pure mode shapes. Steps were taken to force the response to occur at the first flexural mode by exciting the bridge at the centre and by distributing weight on the bridge surface to suppress the torsional mode.

The girder-normalization method was used exclusively for the analysis of the mode shapes for this study since it allowed for direct comparison of the mode shape components for different girders. The mode shape was deconstructed into two basic types of deformations; substructure and superstructure. The superstructure component exclusively comprised of flexural deformations, while the substructure components were described by differential and uniform support movement.

4.3. DETECTION OF SUBSTRUCTURE DAMAGE TO A SINGLE SUPPORT

4.3.1. Overview

This section presents the results for the substructure condition states featuring damage to the left support only. Foundation cases considered were the rigid base case (D0), the “hard” (D1) and the “soft” (D2) cases, in addition to a non-uniform soft case (D3). Damage was inferred using the deconstructed mode shape in conjunction with both a simple observation and a quantitative comparison of the areas enclosed by each component.

The relative efficiency of both impact and harmonic excitation methods were compared based on their success in inferring damage. Also, the natural frequency changes resulting from increasingly soft foundation cases were considered to investigate their potential contribution in VBDD methods.

4.3.2. Uniform Substructure Deterioration

This section discusses the same foundation cases as Section 4.2.5, but considers the mode shapes along all four girders. The foundation cases considered are the rigid case ($D0S0W1_a$), the hard foundation case (D1S0W1) and the soft foundation case (D2S0W1). All of the condition states had a right support that was rigid, while the left support was uniformly and incrementally softened.

The deconstructed girder-normalized mode shapes for all girders are shown in Figures 4.14, 4.15 and 4.16. All data for these figures were gathered using harmonic loading; however, impact loading yielded similar results. All the mode shapes gathered for this study are presented in Appendix C (based on the average of five repeated trials as presented in Chapter 3).

Figure 4.14 presents the results for the rigid support case, for which the fundamental flexural mode shapes along of all the girders have been deconstructed into the three components described in Section 4.2.5. The mode shape along each individual girder encloses an area of unity. Upon inspection of the mode shape along each individual girder, it is apparent that the flexural deformations (component A) account for a large portion of the movement. Again, there is also considerable uniform foundation movement (component C), with very little differential support movement (component B),

similar to Figure 4.11. There are, however, differences in the mode shape components among the girders, despite the fact that this represented a case featuring uniform support stiffness across the bridge width (also shown in the bridge-normalized mode shapes shown in Figures 4.2, 4.3, and 4.4). The differences across the girders are most apparent in the amount of uniform support movement, C, observed in each case. The same conclusion can also be drawn when observing the mode shapes for the other condition states, shown in Figure 4.15 and Figure 4.16. Differences in the mode shape component amplitudes across the bridge may be due to variations in the stiffness of the substructure or superstructure; however, there may also still be some torsional interference involved. Additionally, the differences in the mode shape amplitudes among girders could not confidently be described by the condition of the girders or pile caps.

As the foundation was incrementally softened relative to the base case, there was increasingly more differential foundation movement (B) in the girders (shown in Figure 4.15 and Figure 4.16). Stiffness changes to the substructure could therefore be inferred simply by comparing the relative amplitudes of the mode shape components in the figures. This suggests that the mode shape component method requires a comparison of response from other bridge states to the relative “health” of the substructure.

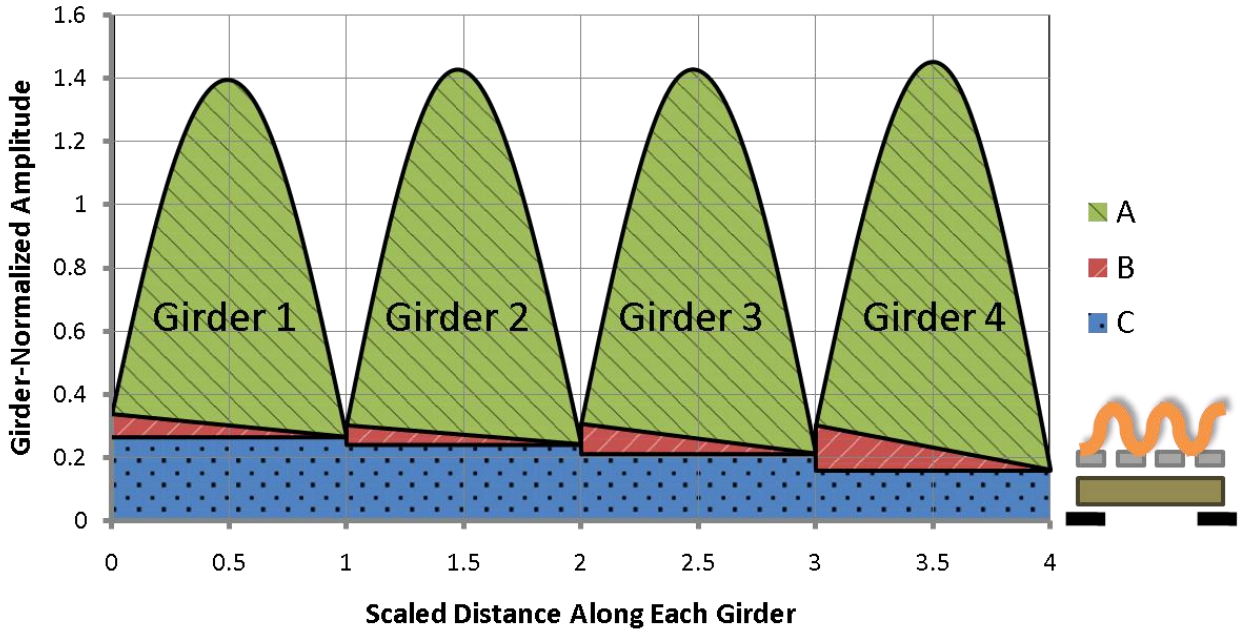

Figure 4.14. Mode shape components along each girder for girder-normalized data from harmonic excitation (rigid foundation case **D0**S0W1$_a$)

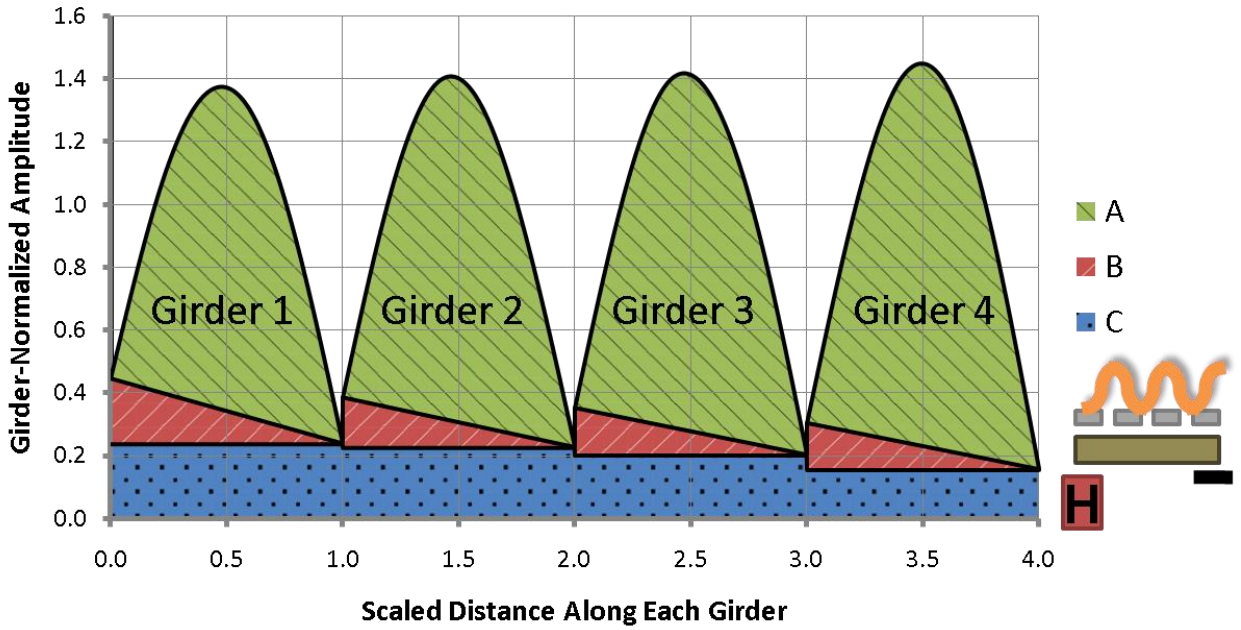

Figure 4.15. Mode shape components along each girder for girder-normalized data from harmonic excitation (hard foundation case **D1**S0W1)

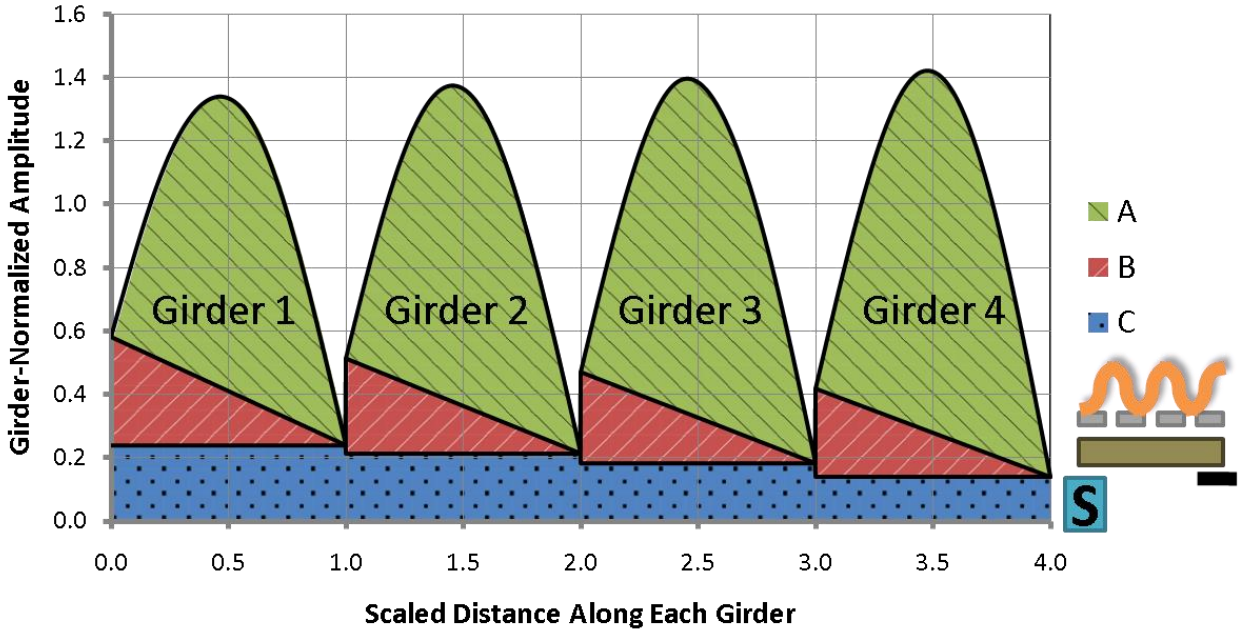

Figure 4.16. Mode shape components along each girder for girder-normalized data from harmonic excitation (soft foundation case **D2**S0W1)

4.3.3. Local Substructure Deterioration

The only foundation case featuring non-uniform local substructure damage had the left end of Girders 3 and 4 bearing on a soft support, while the other supports remained rigid. The frequency spectrum of the lower modes can be seen in Figure 4.17. Although the first flexural and torsional modes are closely spaced, there is a separation valley between the response peaks, making it possible to clearly identify the modes.

When the mode shape was girder-normalized and deconstructed into the three mode shape components, as shown in Figure 4.18, a large difference in the relative responses along the four girder lines is apparent. Considerable differential support movement (B) was observed under the soft supports (Girders 3 and 4), whereas this movement under Girders 1 and 2 was much less.

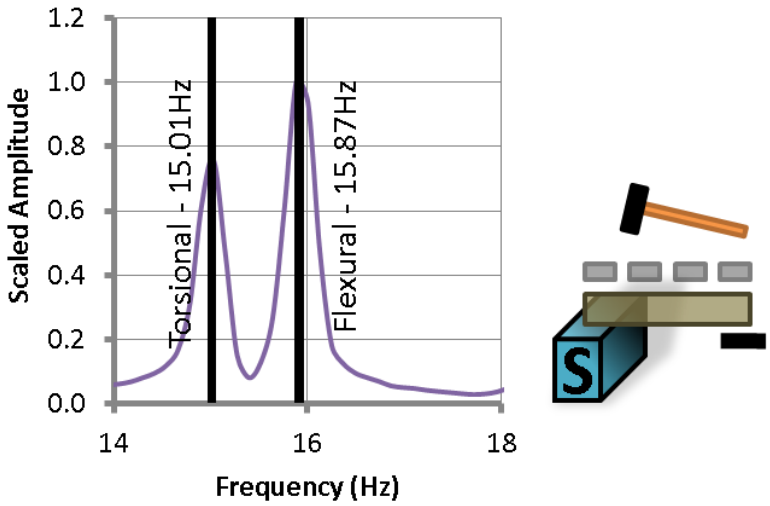

Figure 4.17. Partial frequency spectrum for the reference accelerometer for foundation case **D3**S0W1, showing the first torsional and flexural natural frequency separation

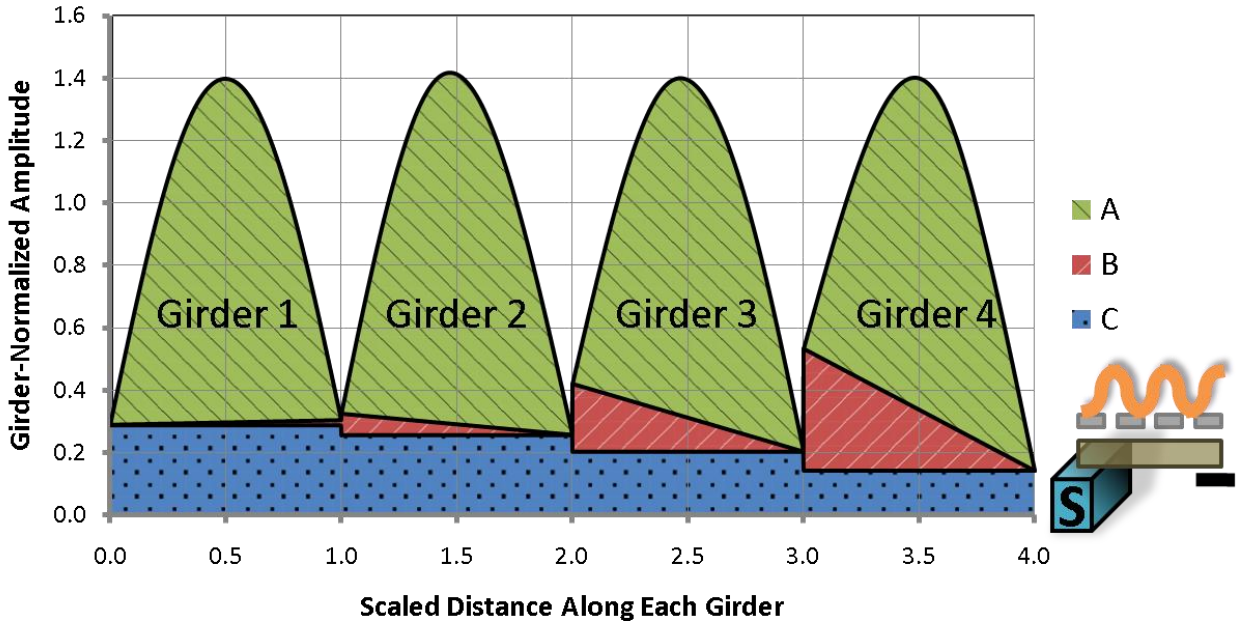

Figure 4.18. Mode shape components for girder-normalized data from harmonic excitation (D3)

It should be noted that the relative girder movement for the local substructure case, shown in Figure 4.18, is distorted from the actual bridge movement that would have been apparent using the bridge-normalization scheme. Figure 4.19 shows the bridge-normalized mode shape, where the actual relative girder movements are presented.

The girders above the soft supports (Girders 3 and 4) exhibited relatively little motion, when compared to the girders over the rigid supports. This is likely due to the fact that the energy over the softened supports was dissipated by compressing the foundation, rather than bending the relatively stiff superstructure.

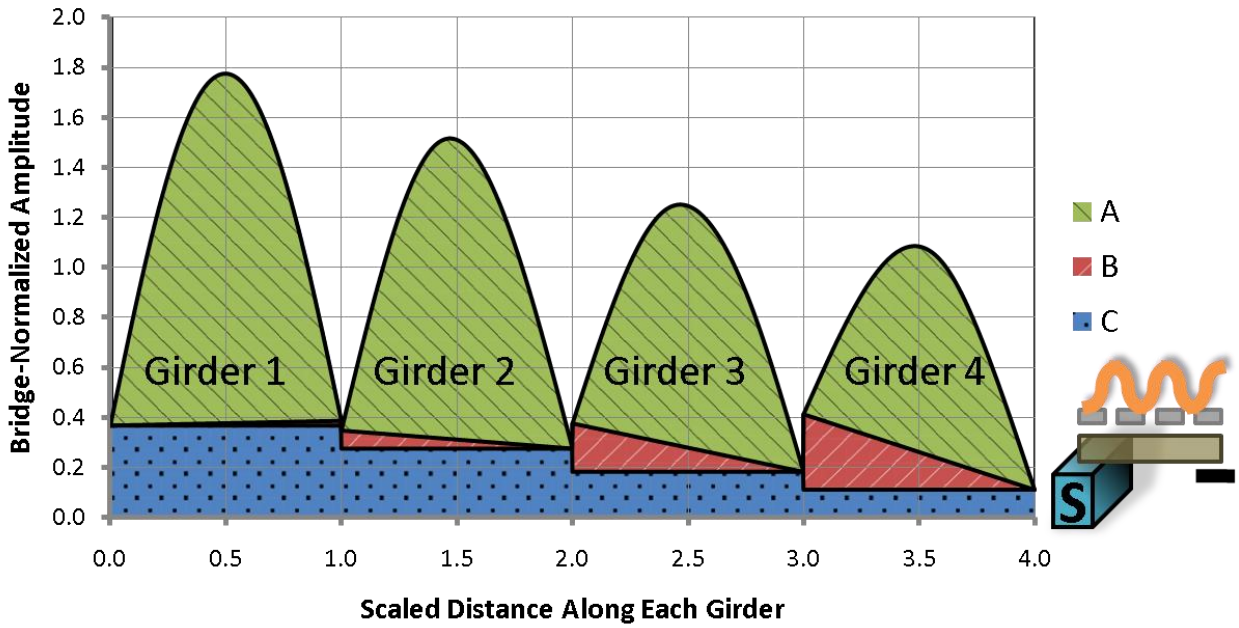

Figure 4.19. Mode shape components for bridge-normalized data from harmonic excitation (D3)

4.3.4. Quantitative Analysis with Mode Shape Components

Up to this point, substructure damage detection has been accomplished by a simple visual comparison of the mode shape components. A more thorough method for direct comparison is to evaluate the amplitudes of areas enclosed by the mode shape components, to allow for a quantitative analysis. A summary of the mode shape components for multiple bridge condition states is shown in Appendix D.

The remainder of the study makes use of a standard chart to summarize the mode shape data produced through deconstructing mode shapes. A labelled summary of a

chart is shown in Figure 4.20 (produced using the same pseudo mode shapes presented in Figure 4.6). In the figure, and all that follow it, the mode shape components for individual girders are plotted separately. In addition, the averaged mode shape components over all four girders are plotted, and the standard deviations of the components are illustrated using horizontal error bars. Figure 4.20 also has an embedded table showing specific values for each mode shape component for reference purposes.

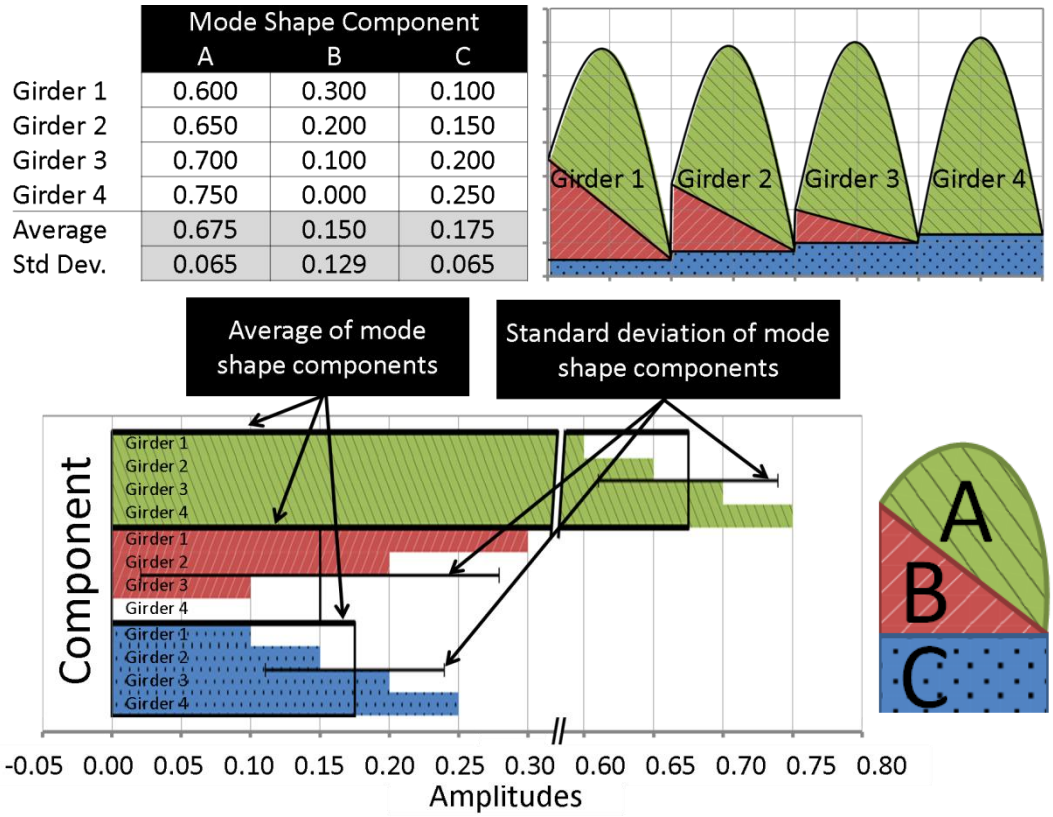

Figure 4.20. Illustration of the standard chart used to summarize the mode shape component data (produced using pseudo data)

Similar to Figure 4.20, Figure 4.21 presents a bar chart that summarizes the mode shape component analysis for the foundation cases already considered (D0, D1, D2, and D3). Once again, the relative differential support movement (B) is seen to

continuously increase as the left support was increasingly softened, while the uniform foundation movement (C) stayed relatively constant. Consequently, the relative contribution of the flexural deformations, A, decreased with continued softening, suggesting that a healthy bridge state will feature significant flexural deformations, and exhibit less substructure movement. Once again, it may be that the mode shape components from other similar bridges with known condition states are required for a comparative analysis to interpret specific patterns in the bridge response.

A further Student's t-test analysis (provided in Appendix G) confirmed the statistical significance (α=0.1) of the variations in the differential support movement as the left support was incrementally softened.

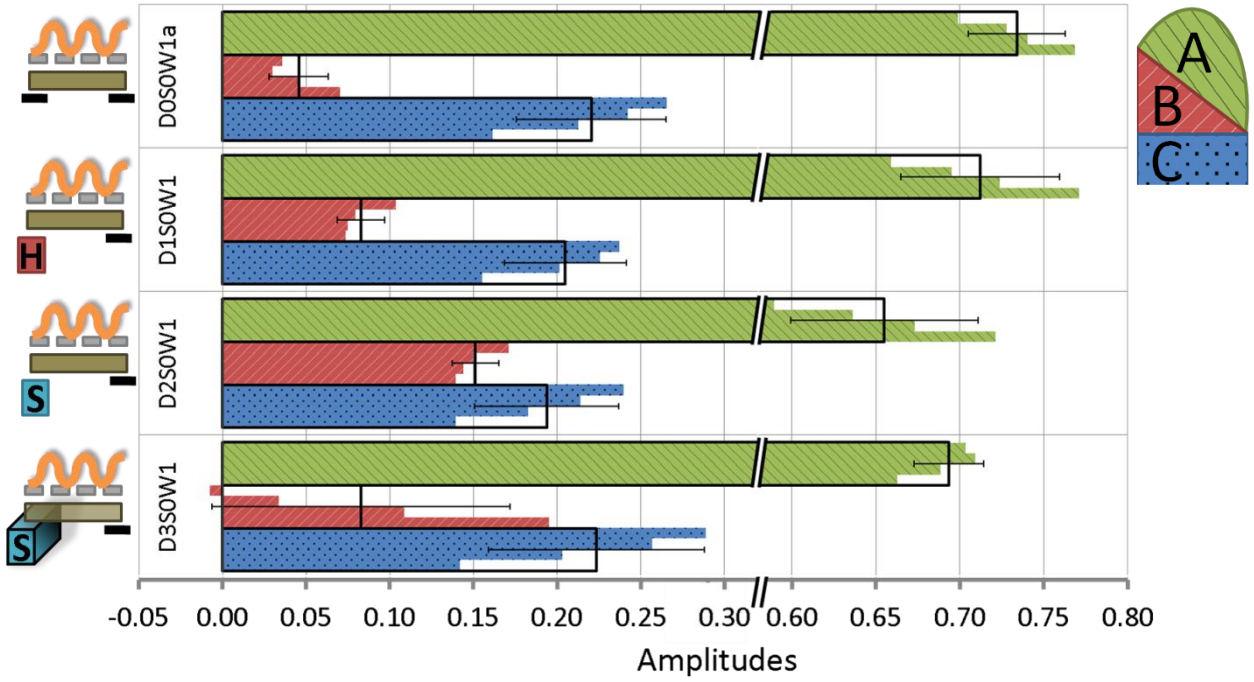

Figure 4.21. Mode shape components of girder-normalized data from harmonic loading (D0, D1, D2, & D3)

Based on the error bars, it is evident that relatively large variations are present among mode shape components along the four girders; this degree of variation was typical of all tests. Consequently, it was concluded that results were best interpreted using averaged mode shape components considering all girders. However, for the non-uniform support case, D3, the between-girder variations in the mode shape components were considerably larger. This suggests that such large variations could be indicative of local damage that should be looked at more closely. A further statistical analysis is presented in Appendix G that uses an F-test on variance to verify that the variance present in the differential support movement on the non-uniform damage case (D3) was statistically significant in relation to the uniform damage cases.

4.3.5. Effect of Excitation

Due to the ease of implementation, damage detection using impact applied to the structure is likely the most efficient excitation method for field application. In this way, VBDD could be made more practical by avoiding the need for using a hydraulic shaker to assess damage. In this section, the mode shapes associated with various substructure condition states are re-analyzed using data obtained when a hammer strike was used as the excitation source.

Figure 4.22 is similar to Figure 4.21, but is plotted to feature data obtained through impact loading. Similar to the results discussed in Section 4.3.4 (and Figure 4.21), the data produced using impact loading suggests that changes in the substructure stiffness may be inferred based on an observation of the deconstructed mode shape. As the left support was incrementally softened, the relative differential support movement became increasingly more prevalent. Likewise, the relative contribution of flexural deformations

decreased as the bridge state deteriorated. Also, the local substructure damage in state D3 was evident in the large standard deviation given by differential substructure movement component across the four girders, indicating that the individual girder conditions differed.

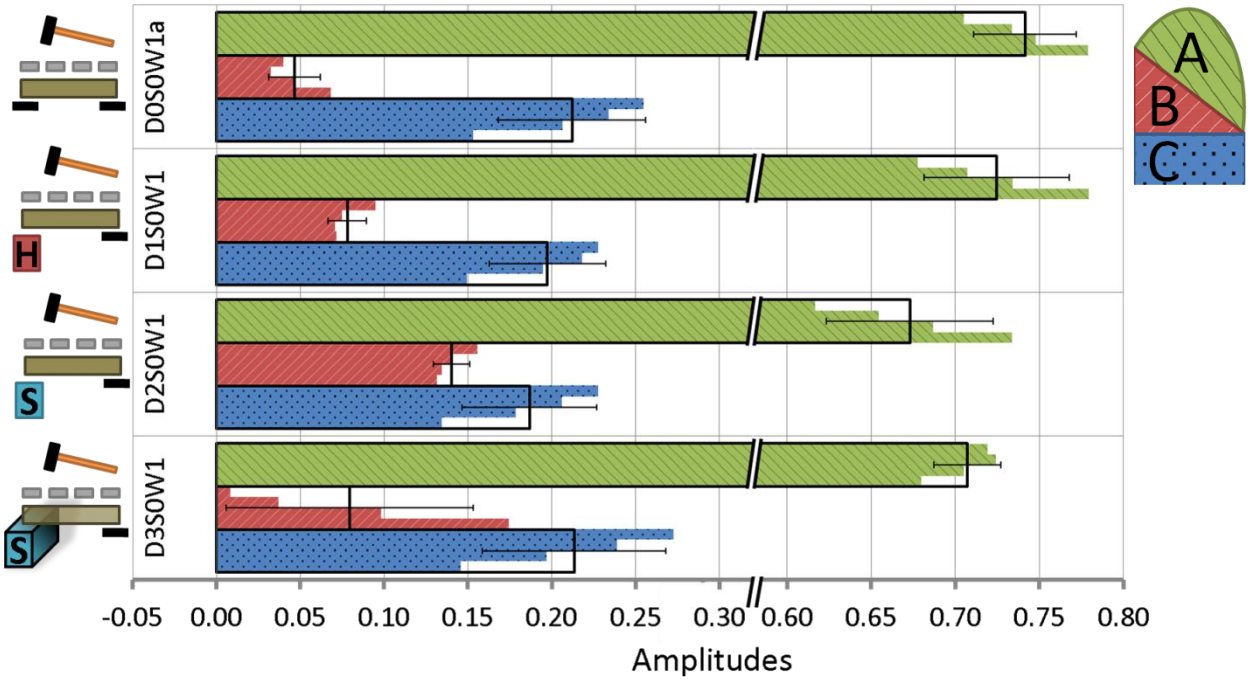

Figure 4.22. Mode shape components for girder-normalized data from impact excitation (D0, D1, D2, D3)

To implement impact testing in the field, no other form of excitation would be needed. Although the test results in this study indicated that the hydraulic shaker achieved less variable results (presented is Section 4.2.4), the mode shapes attained through impact loading were capable of inferring the types of damage considered for this study. Table 4.1 presents the change in mode shape components from the base case ($D0S0W1_a$) for three condition states, considering both impact and harmonic loading. The base case is compared with two foundation cases that were incrementally more flexible on the left

support (D1 and D2), in addition to a repeated trial of the base case ($D0S0W1_b$), which provides a means for assessing changes due solely due to repeated test setups. The change in differential support movement (ΔB) was higher for the tests conducted with harmonic loading, suggesting that harmonic loading may be able to detect smaller changes in the substructure stiffness. Harmonic loading resulted in a change in differential substructure response that was, on average, 14.2% more compared to the values produced using impact loading. However, impact loading did produce significant changes with changing substructure stiffness.

Further comparisons of the two excitation methods are presented in Appendix G using the Student's t-test.

Table 4.1. Change in mode shape components relative to the base foundation case ($D0S0W1_a$) for multiple foundation cases, using two excitation methods

Harmonic	Change in mode shape component			Impact	Change in mode shape component		
D0S0W1a	ΔA	ΔB	ΔC	D0S0W1a	ΔA	ΔB	ΔC
D0S0W1b	-0.008	-0.017	0.003	D0S0W1b	0.000	-0.016	0.011
D1S0W1	-0.022	0.037*	-0.015	D1S0W1	-0.017	0.032*	-0.015
D2S0W1	-0.079*	0.106*	-0.027	D2S0W1	-0.068*	0.094*	-0.025

*Change is statistically significant (α=0.1)

4.3.6. Natural Frequency

Comparisons of natural frequencies can play an important role in VBDD methods. Mode shape analysis alone will limit analysis to bridge deflections, where the stiffness of superstructure can only be inferred in relation to the substructure (and vice versa). However, including natural frequencies in the analysis may provide a means to assess an approximate absolute stiffness of the entire structure, with which the relative stiffness obtained from mode shape analysis may be of more value. Equation 2.7 gave a relationship of natural frequency, bridge length, and bridge weight to the stiffness of the bridge; such a relationship (or Equation 2.8) may provide an approximation of a bridge's overall stiffness (Brashaw et al. 2008; Samali et al. 2003). Specifically, such interactions may be used to assess the serviceability limit state, assuming the superstructure stiffness (EI) can be calculated with some degree of confidence. A limitation of this type of method is that it does not consider the effect that substructure flexibility has on the global stiffness of a bridge.

Superstructure flexibility and substructure softness interact to reduce the natural frequency. Mode shape components will only reveal relative stiffness; natural frequency may be an indicator of the absolute stiffness of the entire structure. In this way, the first flexural frequencies could be compared with that of other bridges (considering bridge weight and length) as an indication of whether the bridge system meets serviceability limit states requirements. Methods utilizing the natural frequency, possibly including a relationship similar to Equation 2.7, could be implemented in the field to complement the mode shape analysis.

The natural frequencies of the bridge structure for the foundation cases already considered are listed in Table 4.2. The natural frequencies were obtained using harmonic loading, in addition to impact loading. In general, the natural frequencies obtained using impact loading were greater than that for harmonic, despite the bridge configurations being equal in both tests (i.e., the mass from the shaker was present during both excitation methods). Thus, it would appear that the timber bridge is stiffer in the impact tests, which would suggest that different excitation methods and amplitudes could introduce some non-linear behaviour. However, it is also likely that the observed differences in natural frequency were due mainly to the precision with which they could be measured using harmonic loading (using a sine sweep, as described in Section 3.5.2) as compared to impact loading (0.05 Hz versus 0.12 Hz).

Table 4.2. Fundamental frequency of the bridge for different softening cases under a single support.

Condition State	Natural frequency (Hz)	
	Harmonic ±0.05Hz	Impact ±0.12Hz
 D0S0W1a	15.91	15.99
 D1S0W1	15.82	15.99
 D2S0W1	15.33	15.50
 D3S0W1	15.65	15.87

The trends observed in the first flexural natural frequencies for the various condition states were as expected. The natural frequency was found to be higher for a stiffer

substructure condition state, and lower for a softer substructure. The natural frequencies for all bridge condition states are shown in Appendix E.

4.3.7. Summary

This section introduced a method to infer substructure damage by deconstructing the first flexural mode shape into components. Bridge condition states with various substructure stiffness values were considered to understand specific mode shape patterns related to substructure damage. Changes in substructure stiffness could be detected using an observation of a single vibration test without reference to a baseline. However, mode shape components from other known bridge states were required for a comparative analysis to interpret specific patterns. Uniform damage to a single support, in addition to a simple local damage case, all provided results that indicated the presence of damage. Harmonic and impact loading gave similar results; however, the results produced with harmonic loading did appear to be slightly more conclusive.

Changes in the first natural frequency were also analyzed. The observed changes in the natural frequency were as expected; stiffer substructure cases had the highest natural frequencies, and more flexible cases had incrementally smaller frequencies.

4.4. SUBSTRUCTURE DAMAGE DETECTION ON BOTH SUPPORTS

4.4.1. Overview

This section extends the work from Section 4.3 to include realistic substructure stiffness conditions under both pile caps. A rigid support case was also included to act as a base case.

4.4.2. Results and Discussion

The results for tests considering stiffness changes to both supports are shown in Figure 4.23 (produced using harmonic loading). The figure shows distinct patterns in the mode shape components for specific damage states. It can be seen that the flexural component (A) was relatively greater for stiffer supports, and the relative differential support movement (B) was at a maximum for the differential (soft-hard) support case (D6). The uniform support component (C) varied as the supports under both pile caps were uniformly softened. There appears to be relatively more uniform support movement for the hard-hard case (D5) when compared to the rigid-rigid case (D0). Similarly the soft-soft case (D4) featured the maximum degree of uniform support movement, as expected. This analysis is extended in Appendix G using a student's t-test that verifies the statistical significance (α=0.1) of changes in the mode shape components as the substructure stiffness was varied.

The natural frequencies associated with these tests are shown in Table 4.3. As expected, the natural frequencies were lowest for the soft support case, and got larger as the substructure was stiffened. As noted in previous sections, the natural frequencies extracted from impact test data were slightly higher than corresponding values from harmonic tests.

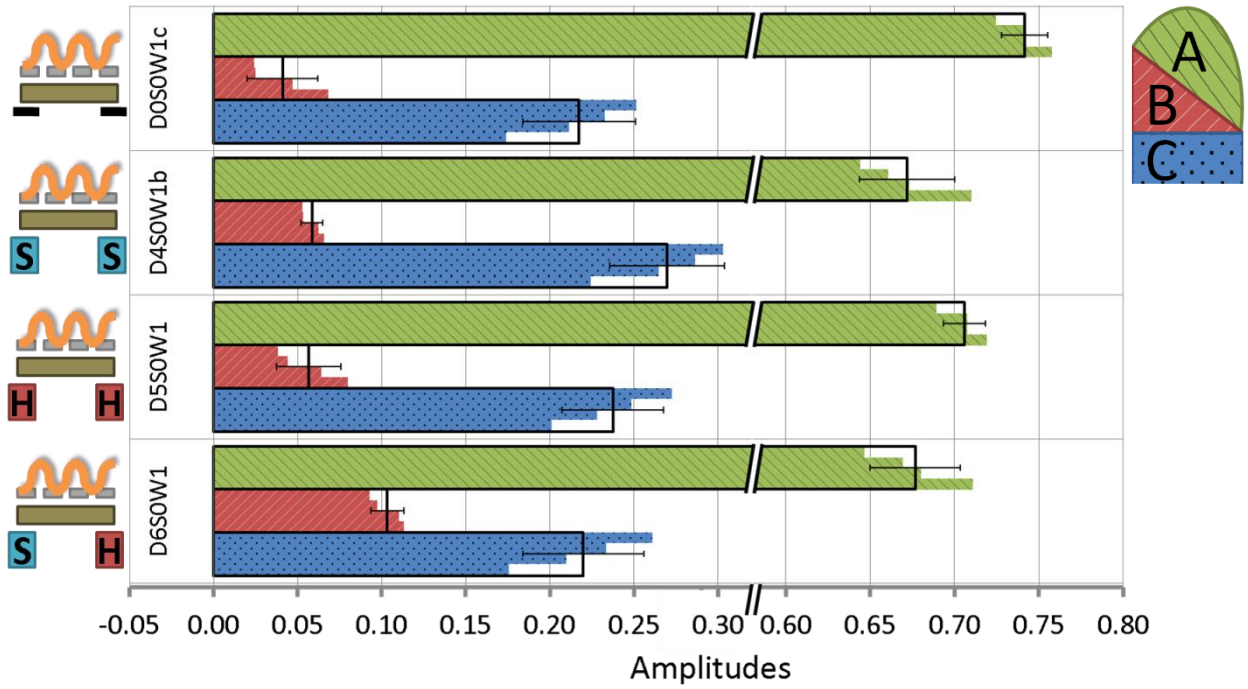

Figure 4.23. Mode shape components for girder-normalized data from harmonic excitation (D0, D4, D5, D6)

Table 4.3. Fundamental frequency of the bridge for cases with damage to both supports

Condition State	Natural frequency (Hz) Harmonic ±0.05Hz	Natural frequency (Hz) Impact ±0.12Hz
D0S0W1b	16.00	16.24
D4S0W1b	15.44	15.63
D5S0W1	15.77	15.99
D6S0W1	15.44	15.69

4.4.3. Summary

In Section 4.3, it was shown that the differential support movement (B) continued to become more prominent as the differences between the stiffness at the left and right supports became larger. This section showed that the uniform support movement (C) increased significantly in relative terms as the entire bridge substructure became more flexible. Nevertheless, in both this and the previous section, it was apparent that the healthy bridge states featured relatively higher proportions of flexural deformations (A).

4.5. INFLUENCE OF SUPERIMPOSED MASS

4.5.1. Overview

Most timber bridges in the field have some form of wearing surface. These can include asphalt or gravel of different thicknesses. As such, for this damage detection method to be feasible, different levels of superimposed mass should not significantly change the character of the mode shape. It is possible that since the mass is directly related to the natural frequency of the bridge, it may also have an effect on the mode shape. Another issue that may emerge when introducing a change in mass is the fact that timber can have a non-linear load-deflection curve. As such, the stiffness of the system could be affected with varying superimposed mass values.

Two weight cases were considered for this study, both having a symmetric distribution, as described in Section 3.7.4 (non-symmetric mass distribution was not considered, which would likely change the character of the mode shape).

4.5.2. Results and Discussion

Figure 4.24 shows the results of the tests that consider changes in super-imposed mass for harmonic loading. The values presented are averaged over the four girders, and the black error bars show the standard deviation over the four girders. The figure shows a definite similarity in the responses for the same substructure condition state (D0S0W1$_b$ & D0S0W2), with different weight cases. The difference between the responses at different weight cases is negligible when compared to the difference in response due to substructure damage (D0S0W1$_b$ vs. D4S0W1$_a$ or D0S0W2 vs. D4S0W2). While these differences are apparent in all three mode shape components, they were only found to be statistically significant for component A (see Appendix G). Based on two weight cases comparing the stiffest and softest foundation, it can be concluded that the substructure state has a more significant effect on the magnitude of the mode shape components than the added weight on the timber bridge deck does as long as the added weight is distributed uniformly (a statistical analysis is provided in Appendix G). This conclusion suggests that the bridge weight range considered for this study does not play a significant role in influencing the relative proportions of the mode shape components. Therefore, bridges in the field with varying wearing surface weights should be able to be tested and compared without consideration given to weight as a variable (as long as the relative distribution of the mass doesn't change substantially).

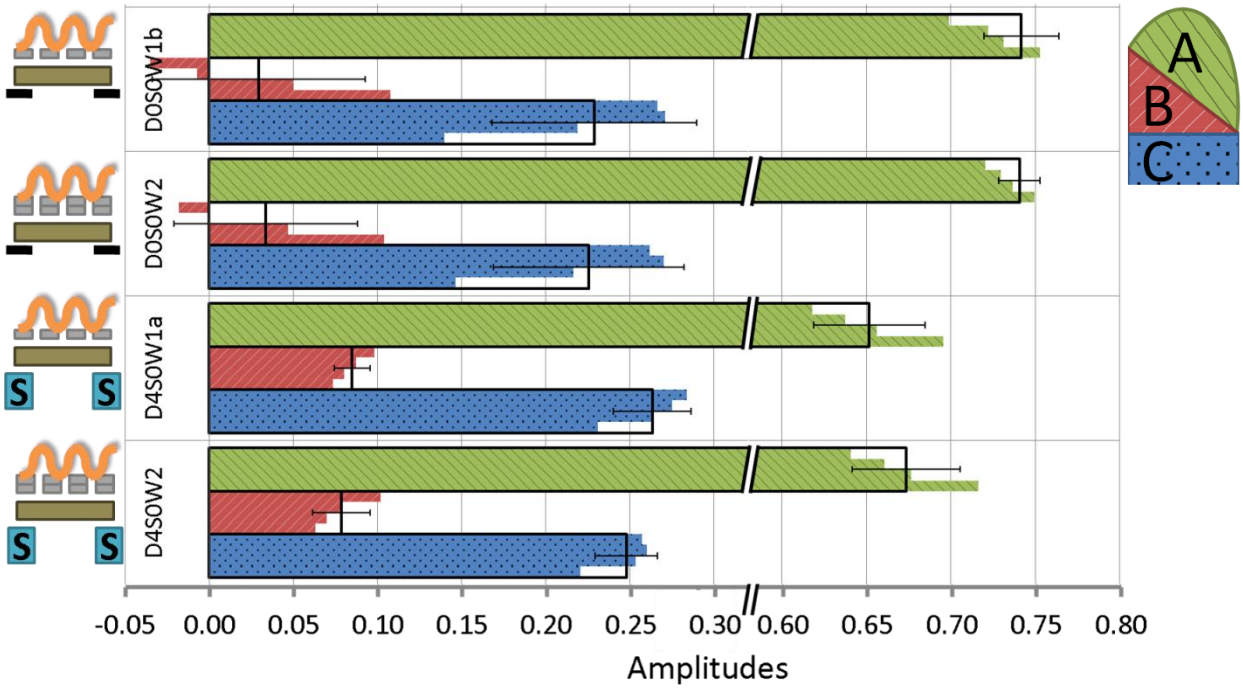

Figure 4.24. Mode shape components from harmonic excitation for different weight cases

Table 4.4 shows the effect of the bridge weight on the first natural frequency. A softer foundation and a heavier structure both reduce the natural frequency. It is unclear from the data which has a greater effect; however, it is important to note that both are key variables determining the natural frequency. This suggests that natural frequency alone cannot be used as an indication of superstructure stiffness, as the substructure and bridge weight both play large roles. Weight and substructure stiffness must both be considered if the natural frequency is to be used as an indication of superstructure stiffness.

Table 4.4. Effect of weight on the fundamental frequency

Condition State	Natural frequency (Hz) Harmonic ±0.05Hz	Impact ±0.12Hz
 D0S0W1b	15.85	16.08
 D0S0W2	15.02	15.30
 D4S0W1a	15.22	15.48
 D4S0W2	14.61	14.77

4.5.3. Summary

The results presented here suggest that different levels of superimposed weight on the bridge have little influence on the relative contributions of mode shape components. The bridge weight had a minor effect on the mode shape components; however, variations in the substructure stiffness changed the mode shape components to a much greater extent.

It should therefore be feasible to do vibration tests in the field on an assortment of simply supported bridge decks, regardless of the weight of the wearing surface. However, more field testing needs to be completed to better understand the potential influence of non-linear behaviour.

4.6. SUPERSTRUCTURE DAMAGE DETECTION

4.6.1. Overview

The VBDD methods presented in this study thus far have inferred damage considering a single vibration test, while comparing results from a range of substructure condition states. In this section, the application of more conventional VBDD methods is described; these rely on the direct comparison the mode shape of the bridge in a given state to that in a previous condition state. The methods employed were the change in mode shape (Equation 2.1) and the change in curvature methods (Equation 2.3), as these are among the most widely used approaches in the literature and relatively easy to implement. Damage considered in this phase of the study consisted of small-scale damage to the superstructure.

This section also describes the application of the change in mode shape and change in curvature methods to a bridge with both substructure damage and small-scale superstructure damage. The intent of this final analysis was to try to better understand the effect substructure damage has on detecting superstructure damage and vice versa.

4.6.2. Superstructure Damage Detection

The results for the superstructure damage detection tests are presented in this section, considering only the rigid-rigid (D0) support case. To apply VBDD methods to the superstructure, the substructure components, B and C, were removed and the flexural deformations (A) were re-normalized using girder-normalization enclose a unit-area.

Figure 4.25 and Figure 4.26 show the distribution of change in mode shape and change in curvature, respectively, for the condition state consisting of a cut at the centre of

Girder 2 (S1). It is apparent that the largest changes occurred in both parameters in Girder 2, suggesting that damage has been detected on Girder 2 (level 1 detection). However, the location along the girder was not successfully identified (level 2 detection), since the largest peaks in the damage parameter plots do not coincide with the known damage location. Although the data are not presented here, it was found that the damage could not be detected using impact excitation; mode shapes produced using an impact were found to exhibit substantially more variability (Section 4.2.4) and the effect of the damage was not great enough to make detection possible.

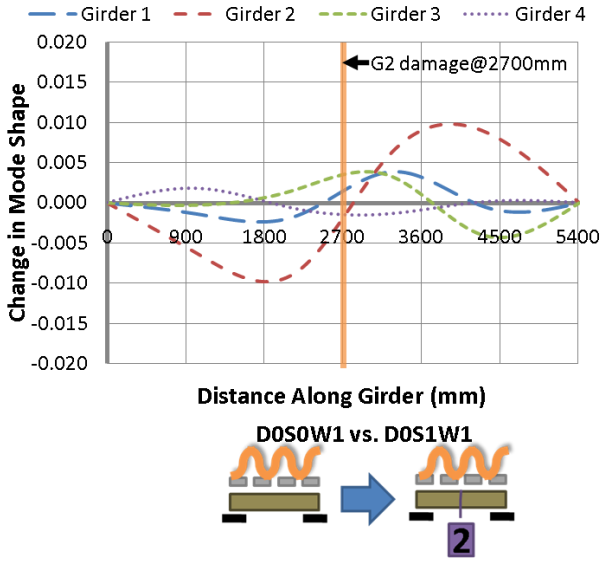

Figure 4.25. Change in mode shape - D0S0W1$_c$ vs. D0S1W1 (harmonic)

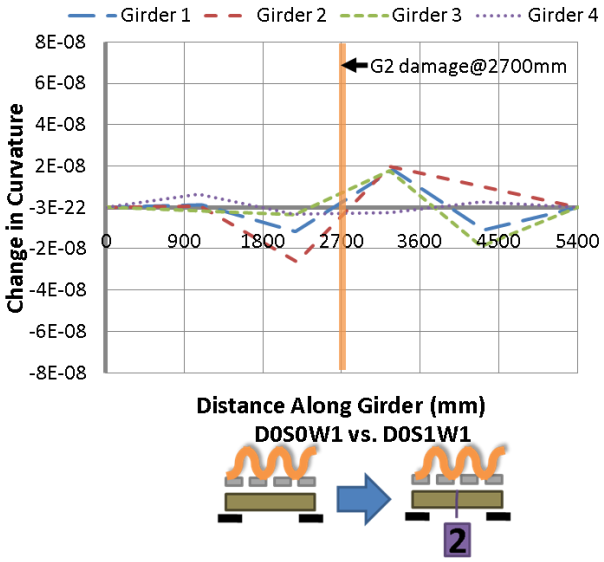

Figure 4.26. Change in curvature – D0S0W1$_c$ vs. D0S1W1 (harmonic)

Figure 4.27 and Figure 4.28 show the results of tests with damage to Girder 4 (S2) using Damage Case S1 as the base case. In both figures, it is clear that damage is most likely to have occurred on Girder 4, and the large positive peaks on the figures indicate that the damage was likely located approximately 2000 mm from the left

support. In this case, the damage was successfully located, as indicated by the peak in the distributions near the damaged location.

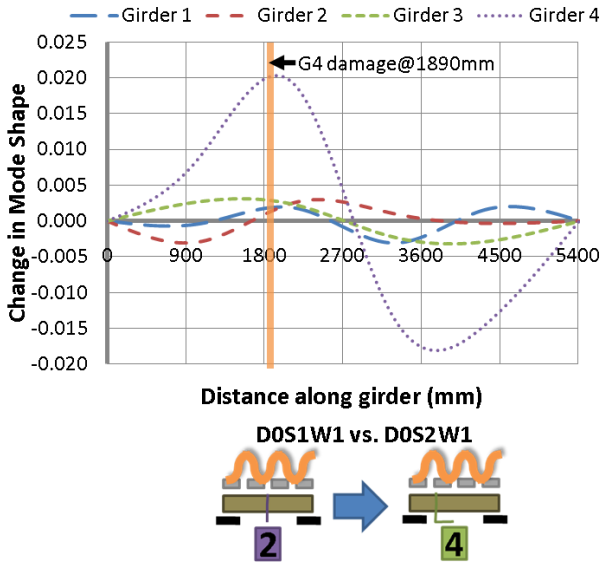

Figure 4.27. Change in mode shape - D0S1W1 vs. D0S2W1 (harmonic)

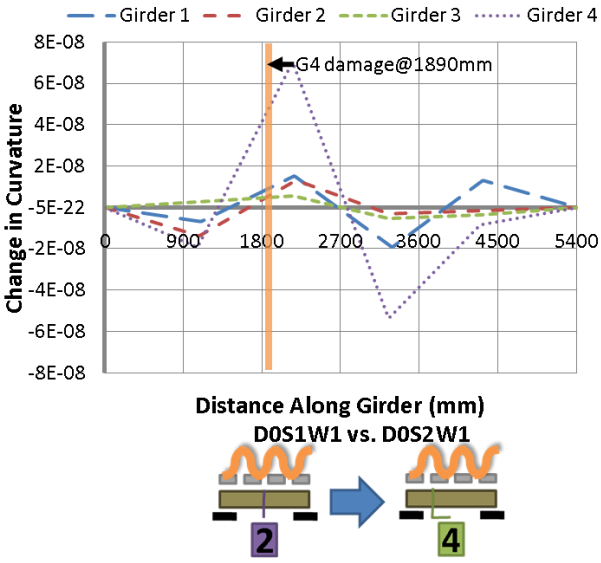

Figure 4.28. Change in curvature – D0S1W1 vs. D0S2W1 (harmonic)

It is interesting to note that localized damage detection on Girder 4 (S2) was successful, while it was not in the previous case (S1), despite similar reductions in the flexural rigidity. One possible reason for this may be that Girder 2 was located at the centre of the bridge, which may have encouraged a greater degree of load redistribution; in other words, the adjacent girders may have reduced the difference in observed response levels by supporting the damaged girder through load sharing.

The results obtained using impact excitation are presented in Figure 4.29 and Figure 4.30. Once again, impact loading did not provide conclusive results. In fact, the large variability of the mode shapes produced during impact tests (presented in Section 4.2.4) exceeded the changes produced by the small scale damage, thereby preventing superstructure damage detection using impact loading. This conclusion is evident when

comparing the multiple large peaks in Figures 4.29 and 4.30 compared to the single large peak featured in Figures 4.27 and 4.28.

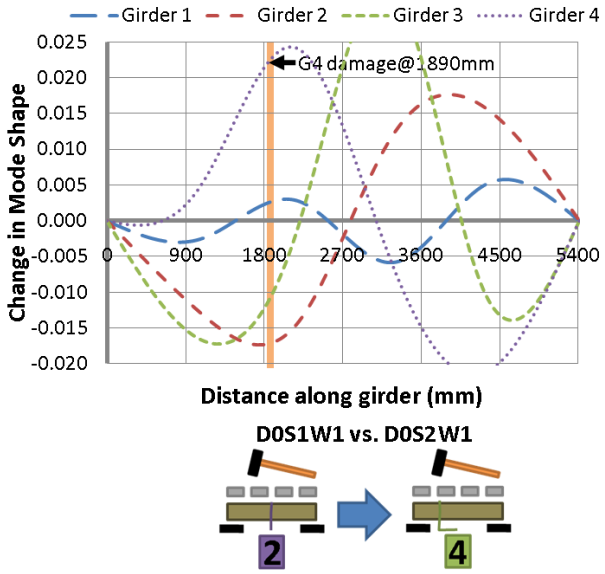

Figure 4.29. Change in mode shape - D0S1W1 vs. D0S2W1 (impact)

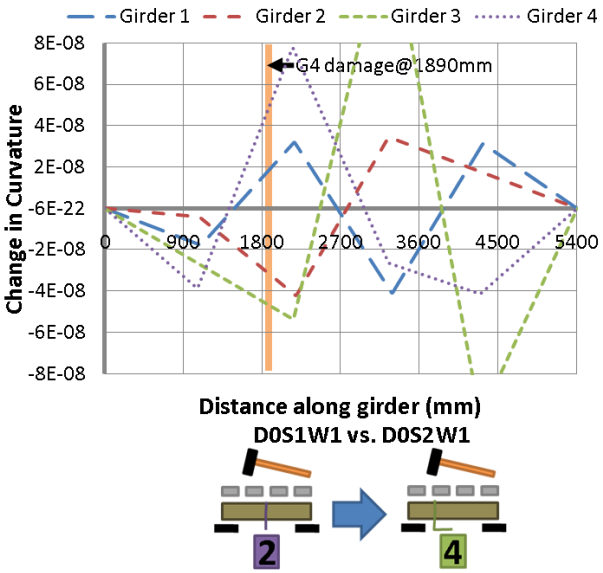

Figure 4.30. Change in curvature – D0S1W1 vs. D0S2W1 (impact)

4.6.3. Substructure and Superstructure Interactions

The final area to be investigated in this part of the study was the interaction of superstructure damage with substructure damage. To apply superstructure damage detection in this study, the substructure movement (B and C) was first removed from the mode shape; the flexural response, A, was then unit-area normalized again. Consequently, this section compares the flexural deformations independent of substructure movement.

In Figure 4.31 and Figure 4.32, the change in mode shape and change in mode shape curvature are plotted, comparing two condition states for which there was a change in substructure condition, as well as in the superstructure condition. The substructure

conditions compared are the rigid base (D0) with the soft foundation case (D4), and the superstructure damage states compare damage to Girder 4 (S2) with a healthy Girder 4 (S1). It is apparent that the results are very similar to those presented in Figure 4.27 and Figure 4.28, for which there was a change in superstructure condition only. Similar results were found for other substructure condition states. In general (for damage to Girder 4), the superstructure damage could be detected regardless of changes to the substructure stiffness, as shown in Appendix F.

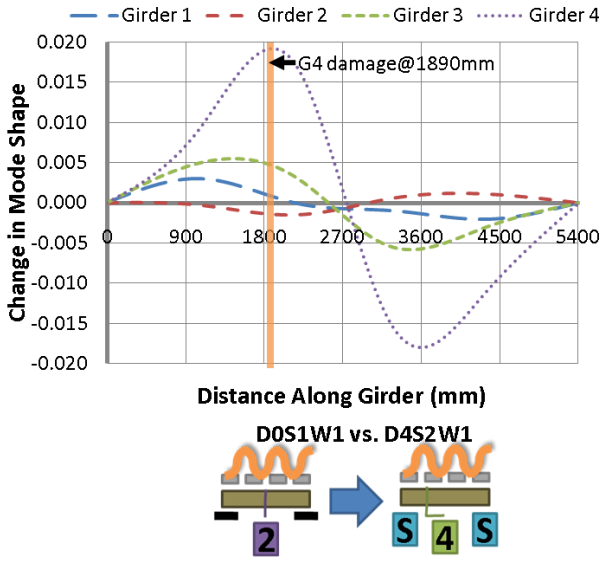

Figure 4.31. Change in mode shape - D0S1W1 vs. D4S2W1 (harmonic)

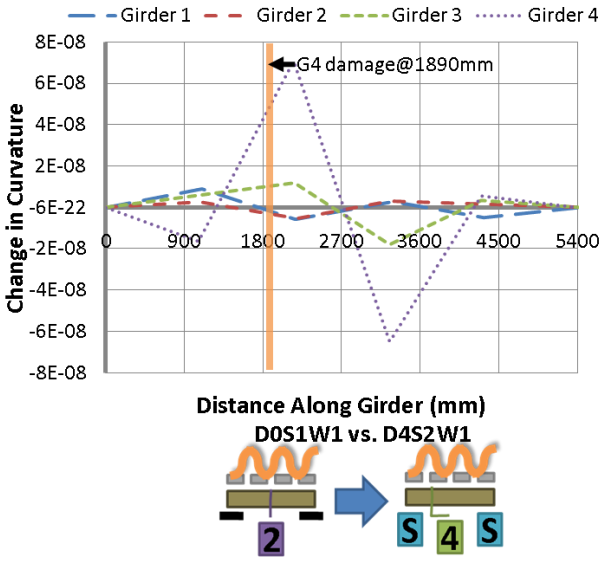

Figure 4.32. Change in curvature – D0S1W1 vs. D4S2W1 (harmonic)

Based on this ability to detect superstructure damage regardless of simultaneous changes to the substructure condition, it can be concluded that the substructure damage does not greatly affect the flexural response of the mode shape once the substructure response components (B and C) have been removed.

Similarly, the superstructure damage considered in this study was not found to influence the results of the substructure components, as shown in Figure 4.33. This figure shows

the mode shape components for three cases of superstructure condition, while the substructure condition remained constant at the “soft-hard” (D5) condition state. Given the same foundation stiffness, there was little change observed in the mode shape components when the superstructure condition states changed. A statistical analysis using a Student’s t-test, provided in Appendix G, further supports this observation considering all remaining substructure cases. It is important to note that the foundation supports were switched out between tests, meaning that the bearing conditions were not exactly the same for the three tests illustrated in Figure 4.33 due to unintended variations in nominally similar test setups.

The observations made from Figure 4.33 may not be the case for larger forms of superstructure deterioration, which should be studied further. Specifically, it is suspected that the foundation will appear relatively stiffer (in the form of minimal substructure movement) when a highly flexible superstructure is present and the mode shape is broken down into components. In other words, only relative movements can be extracted when a normalized mode shape is deconstructed into the three mode shape components. Also, it is possible that larger forms of shear damage, as reported by Peterson (2001), may also produce similar mode shape components to those associated with foundation deterioration.

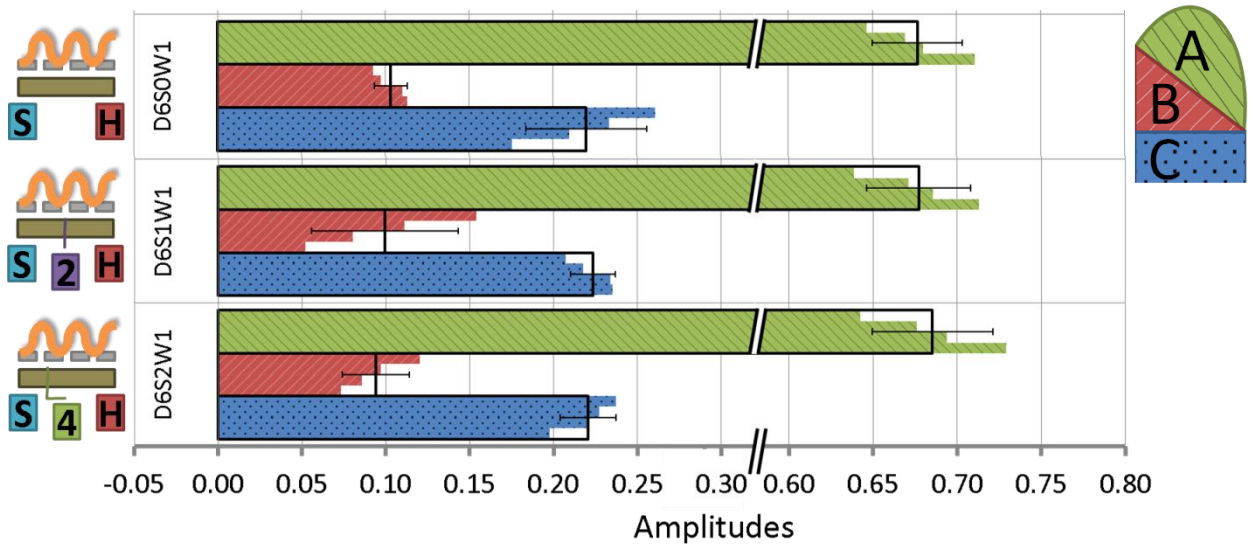

Figure 4.33. Mode shape components for the bridge with a constant foundation case D6, but under various superstructure condition states

As previously shown (Wang et al. 2009), the areas under the change in mode shape (Equation 2.5) and change in curvature (Equation 2.6) plots can be a good indication of Level 1 damage detection (identifying the presence of damage). Figure 4.34 compares the area under the change in mode shape (and change in curvature) for each girder given a specific base case. It should be noted that the plot corresponds to changes in the renormalized superstructure movement, where the substructure movement was removed. Figure 4.34 uses the rigid bridge state as the base case, and compares the area under the change in flexural mode shape to other bridge condition states. Two superstructure condition states are compared (S1 and S2), as well as four substructure condition states (D0, D4, D5, and D6).

A threshold value is defined on Figure 4.34 and Figure 4.35 with a dashed line for the area under the change in mode shape and change in curvature vectors. Values that exceed the threshold indicate that there was a statistically significant change in the

response of the girder as compared to the base case, which suggests that damage has occurred (α=0.0013). The threshold was established to be three standard deviations away from the mean change in area vector when considering an undamaged superstructure state with varying substructure stiffness. More details on the mean, standard deviation and methodology used to establish a threshold are available in Appendix F.

Figure 4.34 shows that damage has been detected on Girder 4 when it was present. Changes in substructure flexibility had little effect on the area under the change in mode shape vector.

Conversely, when the damage to Girder 2 was used in this analysis, the results were once again not as conclusive, as shown in Figure 4.35. The VBDD method was not successful at level 1 damage detection for superstructure damage. Once again, this is likely due to the load redistribution that occurred with the damage to Girder 2.

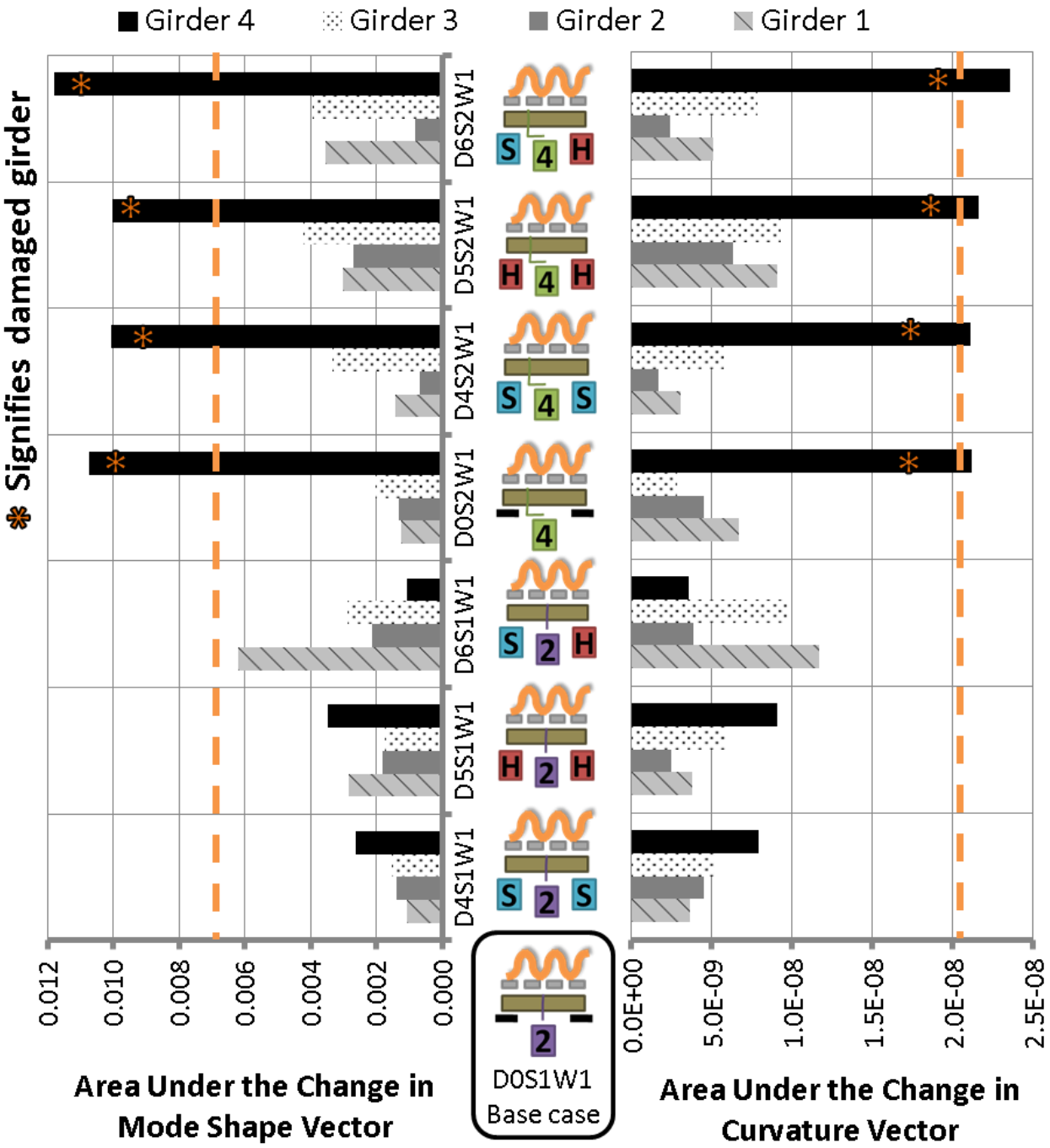

Figure 4.34. Area under the change in mode shape and change in curvature plots when comparing the base case (D0S1W1) to other superstructure and substructure damage states

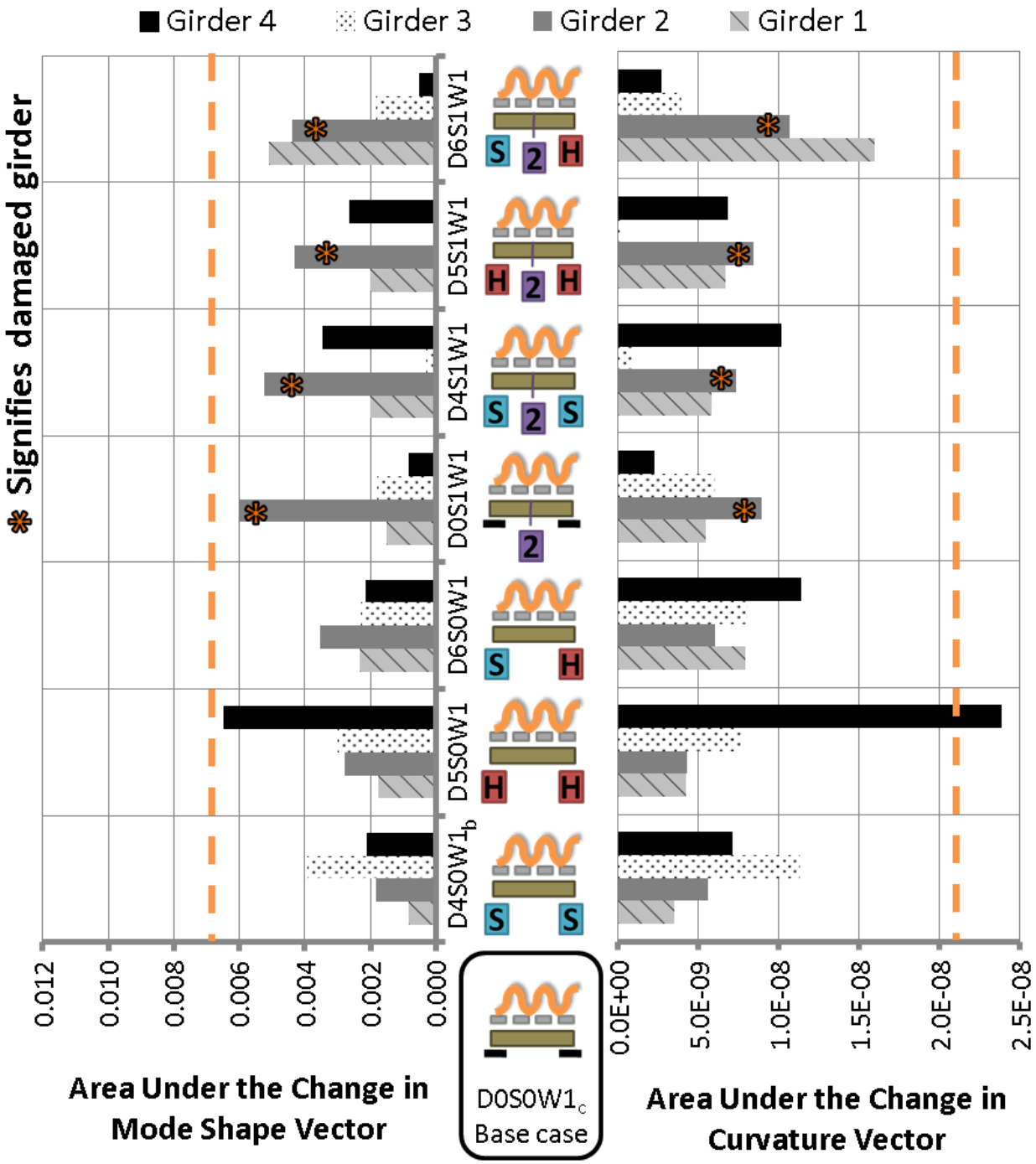

Figure 4.35. Area under the change in mode shape and change in curvature plots when comparing the base case (D0S0W1) to other superstructure and substructure damage states

4.6.4. Summary

Small-scale damage to the superstructure was successfully localized using harmonic excitation, but only when the damage occurred on an external girder. It is likely that the damage would have to be more severe for damage detection to be successful using impact excitation; however, larger damage cases would have to be considered to confirm this.

The results also showed that the superstructure response could be distinguished from the substructure response. The substructure condition did not significantly affect the ability to detect damage to the superstructure. Furthermore, preliminary studies using small-scale superstructure damage indicated that the substructure response was not significantly affected by superstructure damage. However, this may not be the case when significant changes in the superstructure bending stiffness are considered.

4.7. PRACTICAL APPLICATION

4.7.1. Overview

The method of deconstructing a mode shape into superstructure and substructure components appears to have great potential to identify the condition of the substructure of the bridge using a single vibration test. However, in the laboratory, the approach was demonstrated comparing the vibration signatures associated with known condition states. As such, further research is required to gather vibration signatures from a wide range of timber bridges in the field. This section presents some recommendations for practical testing in the field.

In practice, dynamic bridge tests are easier to carry out when impact loading is used for excitation. Additionally, the number of sensors available may be fewer than what was considered for this study. To test the influences of these two factors, the mode shape component method was evaluated using only impact loading and a smaller number of sensors on the timber bridge deck.

4.7.2. Results and Discussion

The timber bridge in the laboratory was intensively instrumented, with the vertical movement of the bridge measured at 22 points. This extent of instrumentation would be very time consuming to implement in the field. Figure 4.36 shows a more limited accelerometer configuration that could be more easily implemented in the field. This configuration includes an accelerometer near the centre of the girder and over both supports for all the girders on the bridge.

Although the hydraulic shaker remained attached at the centre of the bridge for all testing, the excitation for all results presented in this section were obtained using impact loading applied near the centre of the bridge (as described in Section 3.3.2). Impact loading is easy to implement in the field and has already been shown to provide adequate information to apply VBDD methods (Section 4.3.5). Figure 4.37 shows the bridge-normalized first flexural mode shape for the non-uniform foundation case (D3) generated using impact loading and the limited accelerometer configuration.

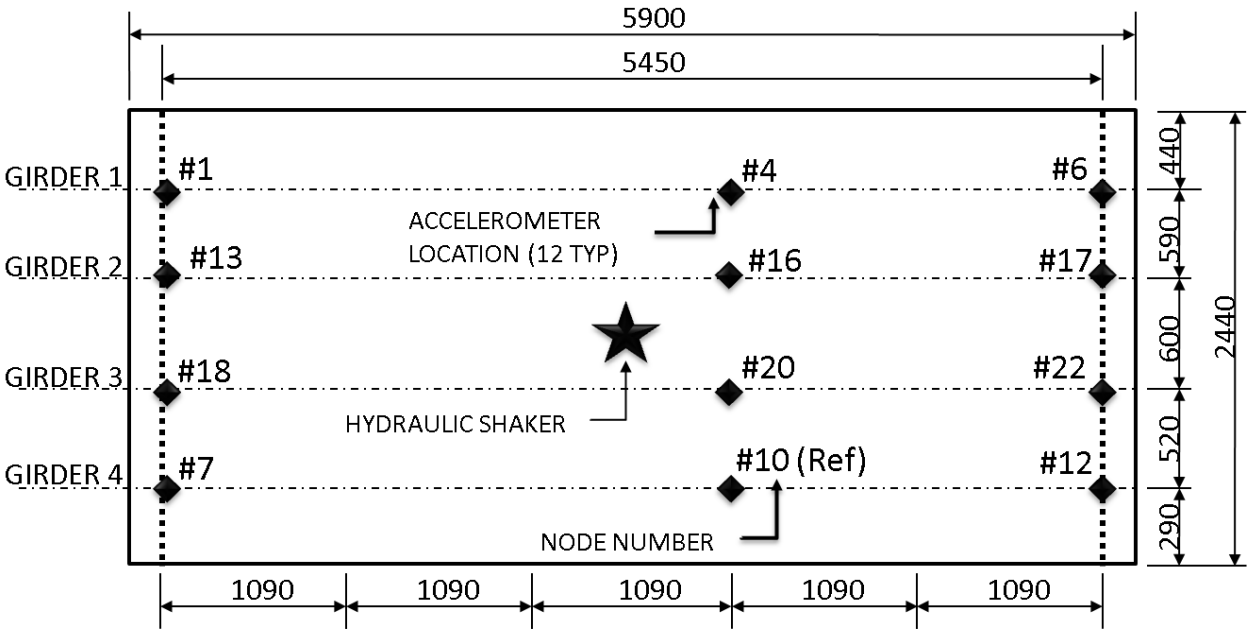

Figure 4.36. Plan view of the bridge, showing accelerometer locations for practical application (dimensions in mm)

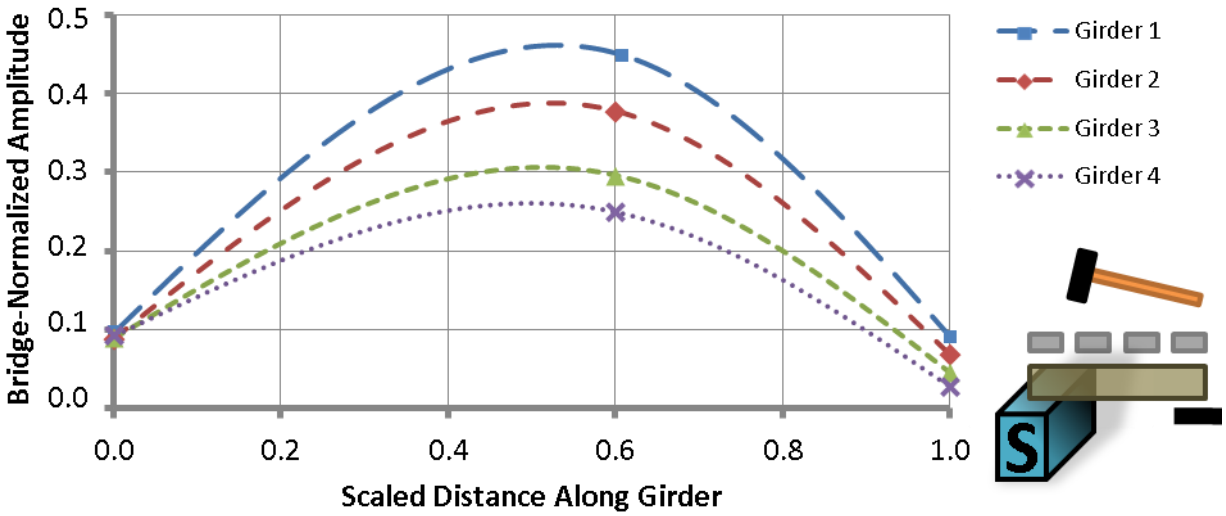

Figure 4.37. First flexural mode shape produced using limited sensors

By using a cubic spline interpolation function (Luong 2009) over each individual girder, the mode shape was interpolated between sensor locations to create a smooth response with zero curvature at supports. The girder mode shapes were then girder-normalized to have a unit-area under each girder. The mode shape components were

then extracted, with the results shown in Figure 4.38. By comparing Figure 4.38 to the more intensively instrumented equivalent shown in Figure 4.22, it is apparent that interpretation of the results was not adversely affected to any significant extent by reducing the number of sensors by nearly half. In both cases (intensive and sparse instrumentation), it is clear that the differential support movement (component B) increased in a relative sense with softening supports and the flexural deformations (component A) decreased with flexible substructure conditions. These conclusions are shown further in Table 4.5 and in a statistical analysis provided in Appendix G.

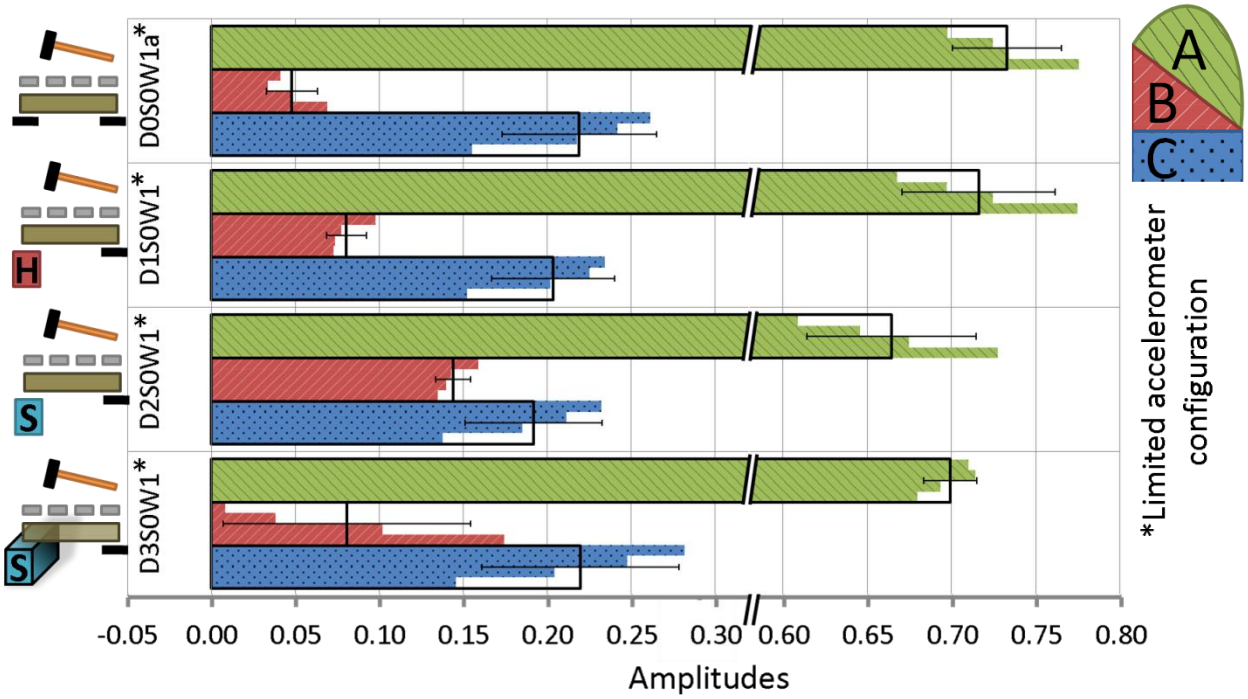

Figure 4.38. Mode shape components for substructure condition states using the limited accelerometer configuration

Table 4.5 presents the change in mode shape components from the base case ($D0S0W1_a$) for three condition states, considering both intensive and sparse instrumentation configurations. The change in the relative contribution of the differential

support movement (ΔB) was not affected by the instrumentation levels, suggesting that intensive instrumentation may not be required. The sparse instrumentation configuration resulted in a change in differential substructure response that was, on average, 1.74% higher than the values produced using intensive instrumentation.

As shown in previous results for detection of substructure damage, flexural deformations (A) are important only in the sense that they provide a basis for evaluating how significant the substructure components are. Although the flexural deformations (A) cannot be totally discounted in identifying damage to the substructure, it seems that a single measurement is enough to quantify the flexural component (A).

Table 4.5. Change in mode shape components relative to the base foundation case (D0S0W1a), for impact loading considering 22 sensors vs. 12 sensors

22 Sensors Impact  D0S0W1a	**Change in mode shape component** ΔA	ΔB	ΔC	**12 Sensors** Impact  D0S0W1a	**Change in mode shape component** ΔA	ΔB	ΔC
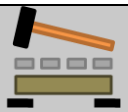 D0S0W1b	0.000	-0.016	0.011	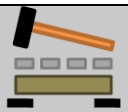 D0S0W1b	0.001	-0.017	0.011
 D1S0W1	-0.017	0.032*	-0.015	 D1S0W1	-0.017	0.032*	-0.016
 D2S0W1	-0.068*	0.094*	-0.025	 D2S0W1	-0.069*	0.096*	-0.027

*Change is statistically significant (α=0.1)

4.7.3. Summary

Limiting the number of sensors had little effect on the ability of the mode shape deconstruction method to infer substructure damage, provided that sensors were placed over the supports to obtain a good measurement of substructure movement. Furthermore, at least one sensor was required on each girder between the supports to quantify the flexural component. In other words, each girder must be instrumented by three sensors to adequately quantify damage using the deconstructed mode shape, one measuring each component.

5. PATTERN RECOGNITION USING NEURAL NETWORKS

5.1. OVERVIEW

This chapter summarizes the limited work that was done using neural networks to aid in pattern recognition using the response signatures gathered during this research program. It is important to note that this chapter is not an extensive investigation of neural networks; rather, the intent was only to provide a brief analysis of the data recovered from this study. This analysis is included to serve as an example of how pattern recognition can be used on deconstructed mode shapes to identify substructure stiffness and infer possible damage.

5.2. BACKGROUND

Artificial neural networks were created to imitate, with a computer, a human's decision-making and learning capabilities. Computers are very good at following rules and doing repetitive calculations, yet their ability to learn and make their own rules is very limited if the logic is not already programmed. Neural networks provide the potential to allow computers to learn and solve complex problems where the pattern cannot easily be described by pre-programmed routines. This is done by modelling a portion of the massive and complex system of neurons that is seen in the human brain to do a very specific task. The end result is an artificial neural network with a broad spectrum of

applications consisting of a highly parallel system that is densely connected, similar to that of the human brain (Dayhoff 1990).

Pattern recognition is just one of the applications that neural networks do extremely well. For pattern recognition, the network is trained with a given set of inputs and the corresponding known outputs so that the network can later recognize patterns without being given the output.

Figure 5.1 illustrates a simple single layer network. In this particular network, the inputs are multiplied by weighting factors, and the results are subsequently added together at the node. The resulting sum is then compared to a threshold value, and a 0 or 1 is returned as an output depending on whether the threshold is exceeded. The weighting factors and thresholds are determined through the training process based on the training data. More complex neural networks would include more layers and nodes.

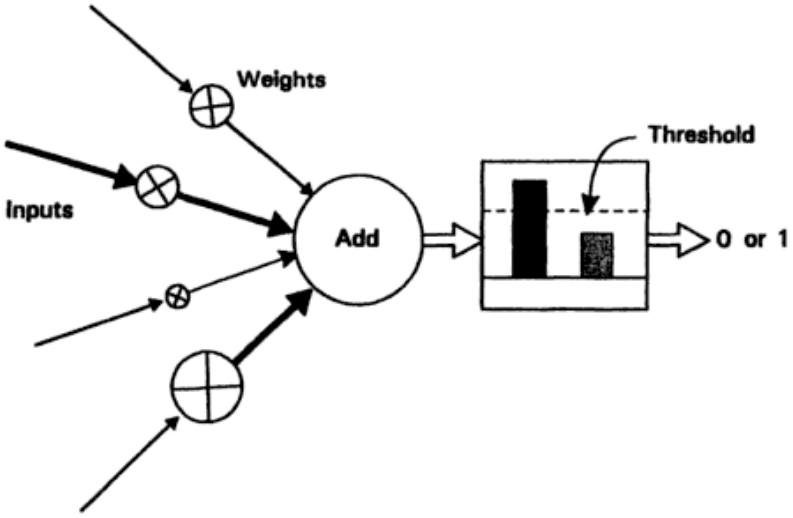

Figure 5.1. A simple artificial neural network (Gurney 1997)

Farrar and Doebling (1999) state that pattern recognition techniques need to be implemented to advance vibration-based damage detection techniques. These techniques could potentially be similar to those that have been practically applied to the monitoring of rotating machinery by the use of databases and statistical pattern recognition. In the current research, neural networks were used as a tool for pattern recognition so that specific bridge deficiencies could be classified using a database of known bridge states. Specifically, the data gathered in this study were used for classifying the condition state of the substructure on the test bridge.

5.3. EXPERIMENTAL PROGRAM

Development and implementation of a neural network is a difficult process that is outside the scope of this research. As an alternative, all neural network analyses for this research program were performed using free software called A.I. Solver Studio (2007) by Perseptio. The A.I. Solver Studio user manual by Perseptio (2007) states,

> *"A.I. Solver Studio is a unique pattern recognition application that deals with finding optimal solutions to classification problems and uses several powerful and proven artificial intelligence techniques including neural networks, genetic programming and genetic algorithms. No special knowledge is required of users as A.I. Solver Studio manages all the complexities of the problem solving internally."*

As suggested, the application excels at classification problems using neural networks for pattern recognition. The program is very simple to use; however, the user has very

little opportunity to understand the architecture and complexity of the developed artificial neural network.

The intent of this chapter was to employ a neural network for its pattern recognition abilities to classify the foundation stiffness based on the mode shape component inputs provided (substructure and superstructure movement). In Table 5.1, the mode shape component inputs produced using impact loading are listed in the six columns on the right; these include the average value and standard deviation of the substructure movement (B and C), as well as those of the superstructure movement (A) over the four bridge girders. For a specific bridge state, the average amplitude of a mode shape component was calculated based on the average of that component from the four girders for the test. Similarly, the standard deviation was calculated based on the amplitudes from the four girders. The desired output was the foundation stiffness, which was classified as “hard” for all setups with rigid or oak supports, or “soft”, for any configuration that included a pine support (signifying a damaged support).

The data in Table 5.1 was used to train the neural network in A.I. Solver Studio. The software had the option to select from multiple complexity levels (trivial to unsolvable) and also allowed for genetic programming within the neural network to aid in the training process. The analysis in this study consisted of a neural network of ‘trivial’ complexity. The genetic programming, “hindsight” and “over-fitting prevention” capabilities available in the software were all disabled. These features were not included because they were either not applicable, or the data set was not large enough to warrant their use.

As suggested in the software user's manual, 20% of the data was withheld from training to be solely used for testing the neural network (Perseptio 2007). Bridge configurations corresponding to the last superstructure condition state (S2) were selected for the verification exercise because this condition state included all four foundation configurations that had previously been used in the training process (see a description of the condition states in Section 3.8.4). The portion of the data used for network verification is shown in Table 5.2.

Table 5.1. Mode shape component data used to train the model

Bridge Configuration	Fdn Stiffness	Average A	Average B	Average C	Std Dev. A	Std Dev. B	Std Dev. C
D0S0W1a	Hard	0.74135	0.04655	0.21210	0.030615	0.01537	0.044001
D1S0W1	Hard	0.72447	0.07809	0.19744	0.043199	0.0114	0.03483
D2S0W1	Soft	0.67296	0.14033	0.18672	0.049607	0.010711	0.040126
D3S0W1	Soft	0.70700	0.07949	0.21351	0.019999	0.073658	0.054731
D0S0W1b	Hard	0.74531	0.03078	0.22391	0.017606	0.045442	0.05713
D0S0W2	Hard	0.74342	0.03941	0.21717	0.009538	0.051387	0.058949
D4S0W1a	Soft	0.66522	0.08011	0.25467	0.026734	0.008399	0.019461
D4S0W2	Soft	0.68493	0.07373	0.24133	0.03003	0.021916	0.012236
D0S0W1c	Hard	0.75414	0.03952	0.20634	0.008655	0.02354	0.030822
D4S0W1b	Soft	0.68679	0.05445	0.25877	0.022491	0.008178	0.030135
D5S0W1	Hard	0.71892	0.05362	0.22746	0.010321	0.01367	0.022385
D6S0W1	Soft	0.69120	0.09895	0.20985	0.020302	0.010073	0.029695
D0S1W1	Hard	0.75823	0.03834	0.20344	0.007341	0.023474	0.028791
D4S1W1	Soft	0.68810	0.04737	0.26453	0.016931	0.005341	0.016583
D5S1W1	Hard	0.72218	0.05648	0.22133	0.009944	0.005653	0.013253
D6S1W1	Soft	0.69468	0.09360	0.21172	0.027986	0.039248	0.012413

Table 5.2. Mode shape component data used to test the model

Bridge Configuration	Fdn Stiffness	Average A	Average B	Average C	Std Dev. A	Std Dev. B	Std Dev. C
D0S2W1	Hard	0.76644	0.04069	0.19286	0.012902	0.01751	0.028322
D4S2W1	Soft	0.68769	0.06069	0.25162	0.027508	0.019835	0.011224
D5S2W1	Hard	0.71294	0.06375	0.22331	0.008128	0.021498	0.025555
D6S2W1	Soft	0.70003	0.08776	0.21221	0.033032	0.017355	0.016601

5.4. RESULTS

The training process was short, requiring only three iterations for convergence to the final network. This suggested that the resulting neural network was relatively simple. All the training data from the four foundation condition states considered (two hard and two soft) converged to the correct solution, as shown in the screenshot (Figure 5.2). Additionally, it is apparent that the neural network predicted the foundation stiffness of the testing data with 100% reliability. This suggests that there was enough difference in the data sets to successfully classify the foundation stiffness as either hard or soft.

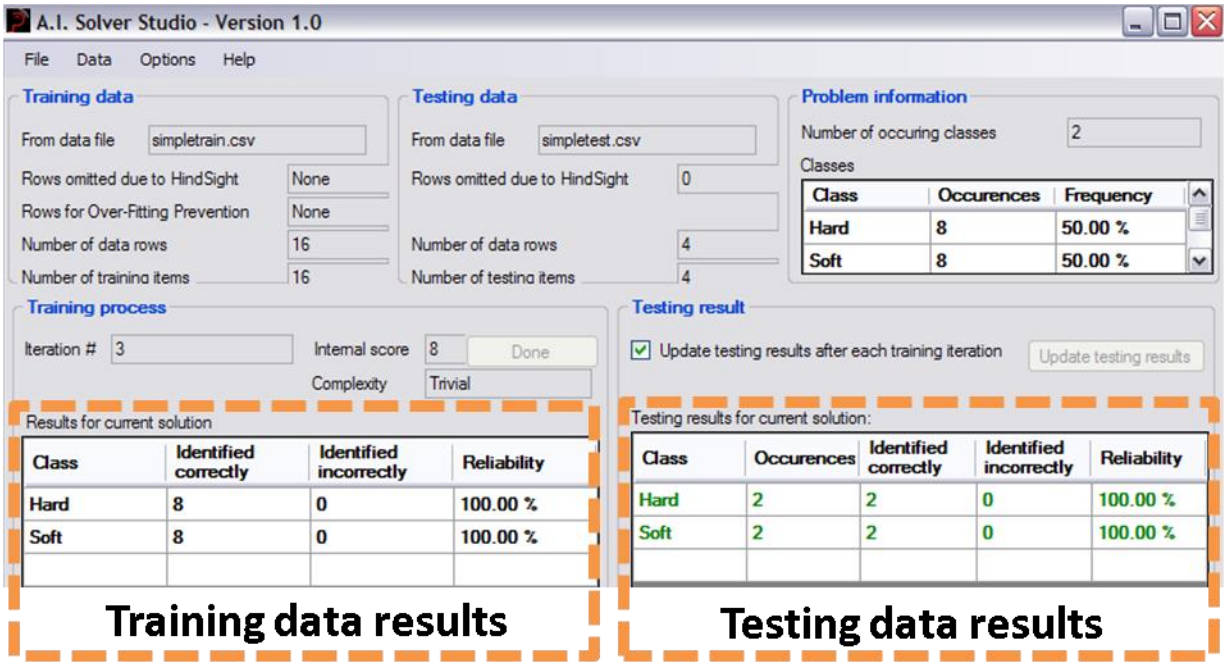

Figure 5.2. A.I. Solver user interface displaying results from both training and testing of the neural network

Figure 5.3 presents a small portion of the data used in the training and testing processes (two of the six columns from Table 5.1 and 5.2 in graphical form). In this

figure, the flexural deformation component (A) is plotted along the x-axis and the uniform support movement component (C) is plotted along the y-axis. To visually distinguish the data sets, data used in the verification process are enclosed with a circle in Figure 5.3, while the training data are represented only by symbols.

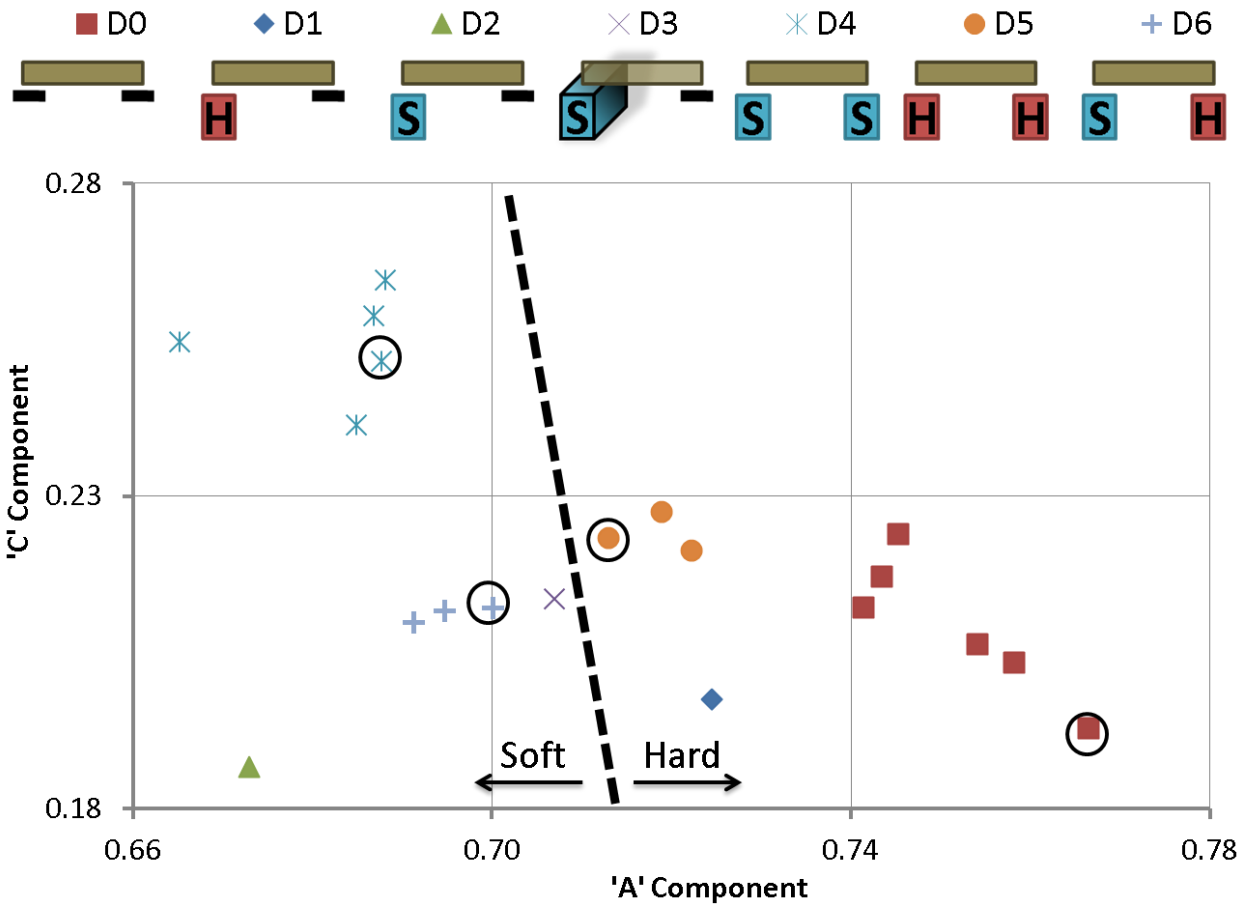

Figure 5.3. Graphical representation of the hard and soft damage cases, and their relationship to mode shape components ‘A’ and ‘C’

Figure 5.3 provides an illustration of one method that the neural network could conceptually use to distinguish between a “hard” and “soft” damage case. For these test results, it is apparent that there is a definite pattern in the organization of the plots, with the training and verification data sets that represent similar substructure stiffness

conditions being closely grouped together and well separated from other data groupings. The fact that there is no overlap observed between condition state data could account for the result that unique, non-ambiguous classifications were possible using this approach. It should be noted that the non-uniform substructure stiffness state (D3) is located very close to the dashed line plotted in Figure 5.3 that defines an approximate boundary separating “hard” and “soft” condition results. As a result, to recognize this bridge state as being “soft” would also require consideration of the standard deviation values shown in Table 5.1. Specifically, the large standard deviation of the differential support movement for the non-uniform support case could indicate a “soft” support, as demonstrated by Figure 4.22 and the F-test on variance in Appendix G.

5.5. CONCLUSION

This chapter summarized the results of a limited study that applied pattern recognition software to classify substructure condition states. Although the study gave promising results, in that all substructure stiffness conditions were accurately classified, it was only intended to provide an indication of the potential of this approach as a starting point for future research. To extend this study to field applications, it is suggested that a wide range of timber bridges be tested dynamically in conjunction with an assessment conducted by an experienced bridge inspector to create an extensive database of response signatures that can be correlated to the bridge state identified by the inspector. Through creating the database of bridges with known condition states, further research can be undertaken to determine the practical use of pattern recognition techniques to classify the bridge state given the response signatures.

6. CONCLUSIONS AND RECOMMENDATIONS

6.1. SUMMARY

Vibration-based damage detection (VBDD) has the potential to serve as an integral part of a routine structural health monitoring program. The study described in this thesis considered the application of VBDD methods as a potential solution to the challenge of properly assessing the large and deteriorating inventory of timber bridge infrastructure in Saskatchewan. VBDD methods offer a quick and economical inspection method that can simultaneously evaluate the entire structure for damage. Typically, deterioration in timber bridges occurs within the substructure at locations not readily accessible to current inspection methods. The focus of this study was to apply VBDD methods to assess substructure stiffness on a simply supported timber bridge in the laboratory.

The variables that were considered were the excitation method, the amount of superimposed mass on the deck, damage to the superstructure and realistic stiffness changes to the substructure. It was found that damage to the superstructure could be assessed based on observed changes in response patterns relative to a baseline case, whereas changes in substructure stiffness could be detected considering the dynamic response using a single vibration test.

6.2. CONCLUSIONS

This research included an experimental program designed to assess the influence of substructure deterioration on the dynamic properties of a simply supported timber bridge. Dynamic testing was carried out on a 5.9 m long by 2.44 m wide segment of a timber deck assembly removed from a decommissioned bridge. The significant observations and conclusions from this study are listed below.

- Decreasing the substructure stiffness of the timber bridge resulted in additional movement over the supports and a reduction in the natural frequency of the bridge assembly.
- Substructure deterioration could be inferred by a simple deconstruction of the first fundamental mode shape without reference to baseline (prior to damage condition) measurements.
    - The first flexural mode could be adequately described using three primary components: flexural deformations resembling the fundamental mode shape of a simply supported beam (component A), rigid body rotation associated with differential support movement (component B), and rigid body motion due to uniform support movement at both ends of the girder (component C). The relative contributions of these three components compared to the response of other substructure bridge states provided valuable information regarding the presence and possible location of support deterioration. More specifically, substructure damage influenced these components as follows:

i. Flexural response: The flexural component (A) was more prominent when the substructure was stiffer, resulting in a relative reduction in contribution of the substructure components.

ii. Differential support movement: This component increased as the difference between the support stiffness at the two ends of the girder increased.

iii. Uniform support movement: This component represented the relative contribution of uniform substructure movement to the fundamental mode shape of the bridge. Uniform support movement was always present (even in stiffest substructure cases) and was likely caused by the compressibility of the timber pile cap and bearing region of the girder. However, an increase in the flexibility of the foundation below the cap also caused a further increase in this component.

- Neither the amount of uniformly distributed superimposed mass placed on the deck nor imposed superstructure damage affected the relative amplitudes of the mode shape components. Therefore, for the range of these variables considered, it can be concluded that superimposed mass and superstructure damage did not influence the effectiveness of substructure damage detection for the method proposed.
- Small-scale superstructure damage was detected using VBDD methods that relied on a comparison to a baseline response using harmonic loading. In this case, the imposed damage caused a 38% reduction in the flexural rigidity of an

outer girder on a bridge consisting of four girders. Damage to the outer girder at 1890 mm from one support was identified and successfully localized. Small-scale damage could not be located for damage to an internal girder (possibly due to the greater degree of load sharing available to the interior girders) or by using impact excitation.

- Simultaneous damage to the superstructure and substructure could be differentiated and successfully detected independently.
- Steps were taken to better understand testing protocols for future research in the field. The main observations in this regard are listed below:
    - Mode shapes gathered from impact loading were adequate for detecting substructure damage, but were not adequate for detecting the small degree of damage to the superstructure that was considered in this research.
    - To apply the substructure damage detection methods described in this research, instrumentation is required at each support, while a single measurement at the mid-span of each girder is sufficient for the relative superstructure response. The superstructure need only be heavily instrumented for the superstructure damage detection methods requiring a baseline response.
- Pattern recognition using neural networks and a database of known bridge condition states may be a feasible method to classify a timber bridge's substructure condition in the field. However, a great deal of field research still needs to be done before this methodology can be implemented in practice.

6.3. RECOMMENDATIONS AND FUTURE RESEARCH

It should be noted that the scope of the present study was limited to the bridge, support condition states and environmental conditions investigated as part of this laboratory investigation. It is recognized that the practical application of this approach in the field will introduce a wide range of additional complexities, including an infinite variety of potential structural health states for both the superstructure and substructure, as well as variable and changing ambient conditions. As such, in order to apply this approach in practice, it is recommended that further research be conducted to investigate the in-situ dynamic response characteristics of actual timber bridges of various sizes and configurations with varying degrees of substructure and superstructure deterioration. Also, additional field research is likely required to better understand the non-linear behaviour of timber bridges given a wide range of bridges with different weights.

It is recommended that the preliminary pattern recognition methods used in this study to characterize the structural condition of timber bridges be applied in the field and investigated further. There is considerable work that is still required to calibrate and validate the method. Primarily, a database of actual bridges must be assembled, covering a wide range of substructure stiffness values, superstructure stiffness values, bridge deck weights and geometries, soil types, moisture conditions, and ambient environmental (temperature, humidity, etc.) conditions.

REFERENCES

Beauregard, C. J., Sparling, B. F., and Wegner, L. D. 2010. Vibration-based damage detection for support softening under a simply supported timber bridge. 2nd International Structures Specialty Conference, CSCE, Winnipeg, Manitoba, Canada, Paper No. ST-071.

Brashaw, B. K., Vatalaro, R., Wang, X., Sarvela, K., and Wacker, J. 2008. Development of flexural vibration inspection techniques to rapidly assess the structural health of rural bridge systems. Report No. CTS 08-22, Intelligent Transportation Systems Institute Center for Transportation Studies, Minneapolis, Minnesota.

Burkett, J. L. 2005. Benchmark studies for structural health monitoring using analytical and experimental models. M.Sc. Thesis, Department of Civil and Environmental Engineering, University of Central Florida, Orlando, USA.

Butterworth, S. 1930. On the theory of filter amplifiers. Experimental Wireless and the Wireless Engineer, **7**: 536-541.

Dayhoff, J. E. 1990. Neural network architectures: an introduction. Van Nostrand Reinhold, New York, N.Y.

Doebling, S. W., Farrar, C. R., and Prime, M. B. 1998. A summary review of vibration-based damage identification methods. Shock and Vibration Digest, **30**(2): 91-105.

Donovan, K. A. 2004. Field tests of timber railroad bridge piles. M.Sc. Thesis, Civil Engineering, Texas A&M University, Texas, USA.

Emerson, R. N., Pollock, D. G., Kainz, J. A., Fridley, K. J., McLean, D. L., and Ross, R. R. 1998. Nondestructive evaluation techniques for timber bridges. 5th World Conference on Timber Engineering, Presses PolyTechniques et Universitaires Romandes, Montreux, Switzerland, pp. 670-677.

Farrar, C. R., and Doebling, S. W. 1999. Damage detection II: field applications to large structures. Modal analysis and testing, Nato science series, J. M. Silva and N. M. Maia, eds., Kluwer Academic Publishers, Dordrecht, Netherlands, 345-378.

Fayyadh, M. M., and Razak, H. A. 2012. Condition assessment of elastic bearing supports using vibration data. Construction and Building Materials, **30**: 616-628.

Fleming, K., Weltman, A., Randolph, M., and Elson, K. (2009). Pile engineering 3rd edition. Taylor & Francis, New York, NY:

Foti, S., and Sabia, D. 2011. Influence of foundation scour on the dynamic response of an existing bridge. Journal of Bridge Engineering, **16**(295): 295-304.

Gurney, K. 1997. An Introduction to neural networks. UCL Press, London, England, U.K.

Li, J., Samali, B., and Crews, K. I. 2004. Determining individual member stiffness of bridge structures using a simple dynamic procedure. Acoustics Australia, **32**(1): 9-12.

Luong, B. 2009. Spline derivative - spline1d.m [MATLAB function]. Available from MATLAB Central: http://www.mathworks.com/matlabcentral/fileexchange/24996-spline-derivative [cited 21 October 2011].

Martenson, A. 2003. Short- and long-term deformations of timber structures. Timber engineering, S. Thelandersson and H. J. Larsen, eds., John Wiley & Sons Ltd, West Sussex, England, 221-240.

Muchmore, F. W. 1986. Designing timber bridges for long life. Transportation Reasearch Record, **1053**: 12-17.

National Instruments. 2005. Labview - TM v.8.0 [computer software]. Austin, Texas.

Ou, F. L., and Weller, C. 1986. An overview of timber bridges. Transportation Research Record, **1053**: 1-12.

Pandey, A. K., and Biswas, M. 1994. Damage detection in structures using changes in flexibility. Journal of Sound and Vibration, **169**(1): 3-17.

Pandey, A. K., Biswas, M., and Samman, M. M. 1991. Damage detection from changes in curvature mode shapes. Journal of Sound and Vibration, **145**(2): 321-332.

Perseptio. 2007. A.I Solver Studio - Version 1.0 [software]. Available from Perseptio: http://www.perseptio.com/Products.aspx [cited 13 October 2011].

Perseptio. 2007. A.I. Solver Studio - user manual. Available from Perseptio: http://www.perseptio.com/AISolverStudioManual.aspx [cited 13 October 2011].

Peterson, S. T., McLean, D. I., and Pollock, D. G. 2003. Application of dynamic system identification to timber bridges. Journal of Structural Engineering, **129**(1): 116-124.

Peterson, S. T., McLean, D. I., Symans, M. D., Pollock, D. G., Cofer, W. F., Emerson, R. N., et al. 2001. Application of dynamic system identification to timber beams II. Journal of Structural Engineering, **127**(4): 426-432.

Pham, T. 2009. The influence of thermal effects on structural health monitoring of attridge drive overpass. M.Sc. Thesis, Department of Civil Engineering, University of Saskatchewan, Saskatoon, Canada.

Poulos, H. G., and Davis, E. H. 1980. Pile foundation analysis and design. Wiley, New York, N.Y.

Ramirez, R. W. 1985. The FFT: fundamentals and concepts. Prentice-Hall, Englewood Cliffs, New Jersey, USA.

Ritter, M. A. 1990. Timber bridges: design, construction, inspection and maintenance. Report No. EM 7700-8, United States Department of Agriculture Forest Service. Washington, DC.

RTA. 2008. Timber bridge manual. Roads and Traffic Authority of NSW, New South Wales, Australia.

Rytter, A. 1993. Vibration-based inspection of civil engineering structures. Ph.D. Dissertation, Department of Building Technology and Structural Engineering, University of Aalborg, Aalborg, Denmark.

Samali, B., Choi, F. C., Li, J., and Crews, K. 2007. Experimental investigations on a laboratory timber bridge using damage index method for plate-like structures. 5th Australian Congress on Applied Mechanics, ACAM, Brisbane, Australia, pp 114-119.

Samali, B., Crews, K. I., Li, J., Bakoss, S. L. and Champion, C. 2003. Assessing the load carrying capacity of timber bridges using dynamic methods. W.A. State Conference, Institute of Public Works Engineering Australia, Perth, Western Australia.

Siddique, A. B. 2008. Structural health monitoring of Attridge overpass. M.Sc. Thesis, Department of Civil and Geological Engineering, University of Saskatchewan, Saskatoon, Canada.

Sohn, H., Farrar, C.R., Hemez, F.M., Shunk, D.D., Stinemates, D.W. and Nadler, B.R. 2004. A review of structural health monitoring literature: 1996–2001. Report No. LA-13976-MS. Los Alamos National Laboratory, Los Alamos, NM.

Sun, Y., Wegner, L. D., and Sparling, B. F. 2007. Vibration-based damage detection of support softening under a timber bridge stringer. 3rd International Conference on Structural Health Monitoring of Intelligent Infrastructure, SHMII, Vancouver, British Columbia, Canada, Paper No. 81.

The Mathworks, Inc. 2008. MATLAB - v.7.7.0 [computer software]. Natick, Massachusetts, USA.

U.S. Army Corps of Engineers. 1990. Engineering design: settlement analysis. Department of the Army, Washington, DC.

Wang, Y., Sparling, B. F., and Wegner, L. D. 2008. Vibration-based damage detection on a multi-girder bridge deck. CSCE 2008 Annual Conference, Quebec City, Quebec, Canada, Paper No. ST-302.

Wang, Y., Wegner, L. D., and Sparling, B. F. 2009. Sensitivity of test procedures for vibration-based damage detection on a multi-girder bridge superstructure. 4th International Conference on Structural Health Monitoring on Intelligent Infrastructure, SHMII, Zurich, Switzerland, Paper No. 446.

Watt, D., Snodgras, L., Engel, K., Fussell, J., Horner, J., and Burn, J. 2008. Saskatchewan bridge management from a spatial perspective. 2008 Annual Conference of the Transportation of Canada, TAC, Toronto, Ontario, Canada, 13pp. (CD-ROM).

Wegner, L. D., Sparling, B. F., and Bagchi, A. 2011. Vibration-based monitoring. Monitoring Technologies for Bridge Management, B. Bakht, A. A. Mufti, and L. D. Wegner, eds., Multi Science Publishing Co Ltd, Brentwood, Essex, U.K., 207-258.

Welch, P. D. 1969. The use of fast Fourier transform for the estimation of power spectra: a method based on time averaging over short, modified periodograms. IEEE Transactions on Audio Electroacoustics, **17**(2): 151-157.

Zhou, Z. 2006. Vibration-based damage detection of simple bridge superstructures. Ph.D. Dissertation, Department of Civil and Geological Engineering, University of Saskatchewan, Saskatoon, Canada.

APPENDIX A. SIGNAL PROCESSING

The following is a more detailed description of the signal processing methods that were used in this thesis (see Section 3.5.3). The raw accelerometer data was processed using a MATLAB routine, which is summarized in this appendix.

Initial MATLAB parameters

Number of data points, ndp=4096

Sampling frequency, hz=500

i. Raw accelerometer data in time domain (impact and harmonic)

Each bridge case consisted of five repeated trials (using all three of the acceleration configurations shown in Table 3.2). In each trial, the response from each of the eight accelerometers was recorded in columns 1 through 8 in the data file. The 9^{th} column was reserved for time.

ii. Apply accelerometer calibration factor

The response of each accelerometer was multiplied by its respective accelerometer calibration factor, as shown in Table A.1. The table shows two of the dates that the accelerometers were calibrated; the changes in the accelerometers deviation from ‘actual’ acceleration stayed relatively constant.

Table A.1. Acceleration calibration factors from different dates

	Accel 1	Accel 2	Accel 3	Accel 4	Accel 5	Accel 6	Accel 7	Accel 8
Feb 10 2011	1.0014	1.0043	1.0011	0.9996	0.9975	0.9991	0.9955	1.0016
Mar 7 2011	1.0011	1.0048	1.0011	0.9995	0.9975	0.9993	0.9955	1.0013

iii. Filter (high-pass and low-pass)

MATLAB command lines:

```
%apply lowpass filter 50hz
    order=2;
    flp=50;
    [z,p,k]=butter(order,flp/(0.5*hz),'low');
    [sosl,gl]=zp2sos(z,p,k);                % Convert to SOS form
    Hd_lp=dfilt.df2tsos(sosl,gl);   % Create a dfilt object
    Qa=filter(Hd_lp,Qa); %implement filter
    Qb=filter(Hd_lp,Qb); %implement filter
    Qc=filter(Hd_lp,Qc); %implement filter
%apply highpass filter 1hz
    fhp=1;
    [a,b,c]=butter(order,fhp/(0.5*hz),'high');
    [sosh,gh]=zp2sos(a,b,c);
    Hd_hp=dfilt.df2tsos(sosh,gh);
    config1=filter(Hd_hp,config1); %implement filter
    config2=filter(Hd_hp,config2); %implement filter
    config3=filter(Hd_hp,config3); %implement filter
```

iv. Moving average

A moving average of five data points was applied to each of the trials to remove random error. The averaging window continually advanced one data point to produce a new filtered data set.

v. Parzen window

MATLAB command lines:

```
%Apply Parzen Window
    w=parzenwin(ndp);
    for i=1:8
       config1(1:ndp,i) = w(1:ndp).*config1(1:ndp,i);
       congig2(1:ndp,i) = w(1:ndp).*config2(1:ndp,i);
       config3(1:ndp,i) = w(1:ndp).*config3(1:ndp,i);
    end
```

vi. Fast-Fourier Transfrom (FFT)

MATLAB command lines:

```
%Apply FFT
    spectrum1 = fft(config1,ndp);
    spectrum2 = fft(config2,ndp);
    spectrum3 = fft(config3,ndp);
```

After the FFT, the magnitude of the spectrum was calculated by taking the square root of the sum of the squares of the real and imaginary components. The phase angles were also extracted at this point.

vii. Scale to the reference accelerometer

The spectral peak at the fundamental frequency of the reference accelerometer for each bridge configuration was scaled to unity, and the remainder of the data were scaled equivalently.

viii. Average frequency spectrum from multiple trials

The magnitudes from five repeated trial were averaged to produce a single spectrum.

ix. Peak picking (first flexural natural frequency and construct mode shape)

The fundamental mode was selected based on the highest peak in the frequency range of interest. The amplitudes of the peaks at the fundamental frequency were then used to describe the amplitude of a specific node on the mode shape.

x. Cubic spline interpolation

A cubic spline was applied along each individual girder, assuming zero curvature at the ends. The routine used was built by Luong (2009).

xi. Normalize mode shape (bridge- and girder-normalized)

Each individual girder mode shape was then scaled to have a unit length and to enclose a unit-area.

APPENDIX B. OBTAINING SUBSTRUCTURE STIFFNESS

This appendix is an extension of Section 3.7.2 and provides further discussion on the resources used to determine the realistic substructure stiffness for the timber bridge in the laboratory.

i. Determining pile stiffness above ground, k_p

Figure 3.11 was used to present the concept that an in-service timber pile features non-linear behaviour. This concept is further presented by Donovan (2004) in Fig. 1.4. Additionally, the data used to create Figure 3.12 can be found in Table 1.1 of Donovan (2004). In the table, both the pile stiffness at low loadings (EA/L for β), and the pile stiffness at high loadings (EA/L for λ) are tabulated.

ii. Determining pile-soil system stiffness below ground, k_s

The data in Table B.1 were calculated using Equation 3.3 and were subsequently used to create Figure 3.13. The soil stiffness values used are listed in U.S Army Corps of Engineers (1990).

Table B.1. Summary of stiffness of pile below ground stiffness, k_s

L, rm =	14	ft,	pile Embedment length
d =	14	in,	pile diameter
υ =	0.33		Poisson's ratio

**Constant soil properties with depth (ρ=1)

Stiffness of Clay	E_s (tsf)	E_s (kPa)	G_s (kPa)	L/d	ζ	k_s (kN/mm)
Very soft	50	4800	1805	12	3.2	15.2
Soft	104	10000	3759	12	3.2	31.7
Medium	209	20000	7519	12	3.2	63.4
	313	30000	11278	12	3.2	95.2
	418	40000	15038	12	3.2	126.9
Stiff	522	50000	18797	12	3.2	158.6
Very dense	627	60000	22556	12	3.2	190.3

APPENDIX C. NORMALIZED MODE SHAPES

This appendix lists all the mode shapes used in this study. All the data listed in the tables were produced using the average of five trials and were subsequently bridge-normalized to enclose a unit-norm ($\phi^T\phi=1$) (Wegner et al. 2011).

The mode shape amplitude for each of the four girders is listed in the tables as G1Y for Girder 1, G2Y for Girder 2, G3Y for Girder 3 and G4Y for Girder 4. The position along the girders is listed as G1X, G2X, G3X and G4X.

Table C.1. Unit-norm mode shape for D0S0W1$_a$ from harmonic and impact excitation

D0S0W1$_a$

G1X (mm)	G1Y	G2X (mm)	G2Y	G3X (mm)	G3Y	G4X (mm)	G4Y
0	0.08015	0	0.06586	0	0.06384	0	0.06280
1100	0.23383	1080	0.21556			1060	0.19764
2170	0.32149	2190	0.30523	2160	0.29006	2150	0.28920
3290	0.31495	3250	0.29147	3250	0.27972	3250	0.28835
4330	0.21906			4300	0.19129	4300	0.19169
5410	0.06309	5410	0.05283	5410	0.04436	5410	0.03361

G1X (mm)	G1Y	G2X (mm)	G2Y	G3X (mm)	G3Y	G4X (mm)	G4Y
0	0.08008	0	0.06617	0	0.06145	0	0.05942
1100	0.23455	1080	0.21742			1060	0.19345
2170	0.32445	2190	0.30890	2160	0.28771	2150	0.28761
3290	0.31867	3250	0.29771	3250	0.27261	3250	0.28551
4330	0.21936			4300	0.19199	4300	0.18926
5410	0.06091	5410	0.05182	5410	0.04263	5410	0.03144

Table C.2. Unit-norm mode shape for D1S0W1 from harmonic and impact excitation

D1S0W1

G1X (mm)	G1Y	G2X (mm)	G2Y	G3X (mm)	G3Y	G4X (mm)	G4Y
0	0.10114	0	0.08277	0	0.07458	0	0.06638
1100	0.23384	1080	0.21961			1060	0.20923
2170	0.30643	2190	0.29886	2160	0.29492	2150	0.30547
3290	0.29368	3250	0.28219	3250	0.28189	3250	0.30251
4330	0.20034			4300	0.19186	4300	0.20172
5410	0.05396	5410	0.04861	5410	0.04281	5410	0.03407

G1X (mm)	G1Y	G2X (mm)	G2Y	G3X (mm)	G3Y	G4X (mm)	G4Y
0	0.09598	0	0.07947	0	0.07111	0	0.06323
1100	0.23393	1080	0.21786			1060	0.20591
2170	0.31238	2190	0.30016	2160	0.29383	2150	0.30234
3290	0.29867	3250	0.28550	3250	0.28155	3250	0.29915
4330	0.20434			4300	0.19133	4300	0.19974
5410	0.05231	5410	0.04705	5410	0.04116	5410	0.03232

Table C.3. Unit-norm mode shape for D2S0W1 from harmonic and impact excitation

D2S0W1

G1X (mm)	G1Y	G2X (mm)	G2Y	G3X (mm)	G3Y	G4X (mm)	G4Y
0	0.11436	0	0.10572	0	0.10526	0	0.10371
1100	0.21139	1080	0.21912			1060	0.24941
2170	0.26020	2190	0.28043	2160	0.30839	2150	0.34351
3290	0.24526	3250	0.26142	3250	0.28752	3250	0.33076
4330	0.16537			4300	0.19265	4300	0.21799
5410	0.04710	5410	0.04399	5410	0.04084	5410	0.03456

G1X (mm)	G1Y	G2X (mm)	G2Y	G3X (mm)	G3Y	G4X (mm)	G4Y
0	0.10867	0	0.10049	0	0.09906	0	0.09721
1100	0.21379	1080	0.21697			1060	0.24377
2170	0.26904	2190	0.28148	2160	0.30601	2150	0.34051
3290	0.25567	3250	0.26764	3250	0.28575	3250	0.32749
4330	0.17121			4300	0.19249	4300	0.21585
5410	0.04589	5410	0.04274	5410	0.03949	5410	0.03288

Table C.4. Unit-norm mode shape for D3S0W1 from harmonic and impact excitation

D3S0W1

G1X (mm)	G1Y	G2X (mm)	G2Y	G3X (mm)	G3Y	G4X (mm)	G4Y
0	0.07887	0	0.07461	0	0.08071	0	0.08861
1100	0.26095	1080	0.22834			1060	0.17179
2170	0.36821	2190	0.32010	2160	0.26413	2150	0.22729
3290	0.36444	3250	0.30423	3250	0.25107	3250	0.21936
4330	0.25843			4300	0.17053	4300	0.14069
5410	0.08295	5410	0.05905	5410	0.03902	5410	0.02364

G1X (mm)	G1Y	G2X (mm)	G2Y	G3X (mm)	G3Y	G4X (mm)	G4Y
0	0.08049	0	0.07329	0	0.07361	0	0.07646
1100	0.26767	1080	0.23175			1060	0.15662
2170	0.37981	2190	0.32754	2160	0.25811	2150	0.21155
3290	0.37230	3250	0.31271	3250	0.24491	3250	0.20656
4330	0.26162			4300	0.16833	4300	0.13232
5410	0.07592	5410	0.05596	5410	0.03684	5410	0.02253

Table C.5. Unit-norm mode shape for D0S0W1$_b$ from harmonic and impact excitation

D0S0W1$_b$

G1X (mm)	G1Y	G2X (mm)	G2Y	G3X (mm)	G3Y	G4X (mm)	G4Y
0	0.06735	0	0.06002	0	0.06452	0	0.06855
1100	0.23723	1080	0.21393			1060	0.18906
2170	0.33883	2190	0.30833	2160	0.28076	2150	0.26830
3290	0.33934	3250	0.29690	3250	0.27088	3250	0.26416
4330	0.24447			4300	0.18539	4300	0.17322
5410	0.08513	5410	0.06312	5410	0.04430	5410	0.02700

G1X (mm)	G1Y	G2X (mm)	G2Y	G3X (mm)	G3Y	G4X (mm)	G4Y
0	0.07473	0	0.05535	0	0.05680	0	0.05851
1100	0.26147	1080	0.20544			1060	0.17384
2170	0.37323	2190	0.29833	2160	0.26626	2150	0.24917
3290	0.37089	3250	0.28350	3250	0.25877	3250	0.24661
4330	0.26040			4300	0.17587	4300	0.16278
5410	0.07812	5410	0.05709	5410	0.04030	5410	0.02637

Table C.6. Unit-norm mode shape for D0S0W2 from harmonic and impact excitation

D0S0W2

G1X (mm)	G1Y	G2X (mm)	G2Y	G3X (mm)	G3Y	G4X (mm)	G4Y
0	0.06597	0	0.06182	0	0.06252	0	0.06652
1100	0.24014	1080	0.22042			1060	0.18400
2170	0.34167	2190	0.31969	2160	0.28014	2150	0.26255
3290	0.33893	3250	0.30618	3250	0.26950	3250	0.25188
4330	0.23953			4300	0.18522	4300	0.16907
5410	0.07494	5410	0.06165	5410	0.04363	5410	0.02744

G1X (mm)	G1Y	G2X (mm)	G2Y	G3X (mm)	G3Y	G4X (mm)	G4Y
0	0.07605	0	0.05390	0	0.05625	0	0.06498
1100	0.26839	1080	0.19673			1060	0.18542
2170	0.38369	2190	0.28810	2160	0.26134	2150	0.25358
3290	0.37368	3250	0.29269	3250	0.23568	3250	0.23831
4330	0.26436			4300	0.17249	4300	0.16747
5410	0.07471	5410	0.05411	5410	0.03908	5410	0.02496

Table C.7. Unit-norm mode shape for D4S0W1$_a$ from harmonic and impact excitation

D4S0W1$_a$

G1X (mm)	G1Y	G2X (mm)	G2Y	G3X (mm)	G3Y	G4X (mm)	G4Y
0	0.11393	0	0.09773	0	0.08966	0	0.08101
1100	0.24337	1080	0.22295			1060	0.20706
2170	0.31411	2190	0.29521	2160	0.28612	2150	0.28990
3290	0.30160	3250	0.27847	3250	0.27344	3250	0.28646
4330	0.21086			4300	0.19113	4300	0.19836
5410	0.06728	5410	0.05976	5410	0.05572	5410	0.04946

G1X (mm)	G1Y	G2X (mm)	G2Y	G3X (mm)	G3Y	G4X (mm)	G4Y
0	0.11144	0	0.09550	0	0.08535	0	0.07343
1100	0.25222	1080	0.22726			1060	0.19155
2170	0.33182	2190	0.30517	2160	0.28301	2150	0.27031
3290	0.32059	3250	0.28455	3250	0.26526	3250	0.26820
4330	0.22189			4300	0.18758	4300	0.18484
5410	0.06638	5410	0.05904	5410	0.05371	5410	0.04506

Table C.8. Unit-norm mode shape for D4S0W2 from harmonic and impact excitation

D4S0W2

G1X (mm)	G1Y	G2X (mm)	G2Y	G3X (mm)	G3Y	G4X (mm)	G4Y
0	0.10659	0	0.09088	0	0.08375	0	0.07570
1100	0.23824	1080	0.22168			1060	0.21071
2170	0.30911	2190	0.29765	2160	0.29024	2150	0.30068
3290	0.29591	3250	0.28122	3250	0.27723	3250	0.28723
4330	0.20385			4300	0.19307	4300	0.20435
5410	0.05940	5410	0.05653	5410	0.05395	5410	0.04814

G1X (mm)	G1Y	G2X (mm)	G2Y	G3X (mm)	G3Y	G4X (mm)	G4Y
0	0.12455	0	0.09226	0	0.07004	0	0.05382
1100	0.28962	1080	0.22781			1060	0.15676
2170	0.38224	2190	0.30801	2160	0.25150	2150	0.22517
3290	0.36084	3250	0.29165	3250	0.23797	3250	0.23093
4330	0.25037			4300	0.16934	4300	0.15817
5410	0.06816	5410	0.05578	5410	0.04620	5410	0.03746

Table C.9. Unit-norm mode shape for D0S0W1$_c$ from harmonic and impact excitation


D0S0W1$_c$

G1X (mm)	G1Y	G2X (mm)	G2Y	G3X (mm)	G3Y	G4X (mm)	G4Y
0	0.07602	0	0.06207	0	0.06148	0	0.05985
1100	0.24737	1080	0.21622			1060	0.18433
2170	0.34625	2190	0.30866	2160	0.28012	2150	0.26731
3290	0.33950	3250	0.29521	3250	0.27061	3250	0.26412
4330	0.23478			4300	0.18455	4300	0.17831
5410	0.06382	5410	0.05115	5410	0.04256	5410	0.03354

G1X (mm)	G1Y	G2X (mm)	G2Y	G3X (mm)	G3Y	G4X (mm)	G4Y
0	0.07300	0	0.05967	0	0.05716	0	0.05481
1100	0.25411	1080	0.21912			1060	0.17139
2170	0.36178	2190	0.31696	2160	0.27463	2150	0.24769
3290	0.35374	3250	0.30400	3250	0.26263	3250	0.24453
4330	0.24419			4300	0.18037	4300	0.16590
5410	0.06170	5410	0.04996	5410	0.03996	5410	0.02938

Table C.10. Unit-norm mode shape for D4S0W1$_b$ from harmonic and impact excitation

D4S0W1$_b$

G1X (mm)	G1Y	G2X (mm)	G2Y	G3X (mm)	G3Y	G4X (mm)	G4Y
0	0.09985	0	0.08621	0	0.08076	0	0.07339
1100	0.24296	1080	0.22059			1060	0.19833
2170	0.32507	2190	0.30079	2160	0.28158	2150	0.28045
3290	0.31582	3250	0.28543	3250	0.27084	3250	0.27804
4330	0.22328			4300	0.19077	4300	0.19202
5410	0.07400	5410	0.06288	5410	0.05491	5410	0.04630
G1X (mm)	G1Y	G2X (mm)	G2Y	G3X (mm)	G3Y	G4X (mm)	G4Y
0	0.09656	0	0.08306	0	0.07611	0	0.06680
1100	0.24882	1080	0.22357			1060	0.18486
2170	0.33862	2190	0.30925	2160	0.27854	2150	0.26159
3290	0.33027	3250	0.29618	3250	0.26804	3250	0.26018
4330	0.23152			4300	0.18703	4300	0.18079
5410	0.07236	5410	0.06160	5410	0.05255	5410	0.04191

Table C.11. Unit-norm mode shape for D5S0W1 from harmonic and impact excitation

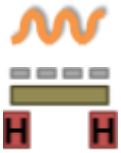

D5S0W1

G1X (mm)	G1Y	G2X (mm)	G2Y	G3X (mm)	G3Y	G4X (mm)	G4Y
0	0.09038	0	0.07433	0	0.07223	0	0.06978
1100	0.24905	1080	0.21844			1060	0.19094
2170	0.33852	2190	0.30344	2160	0.28141	2150	0.27298
3290	0.32901	3250	0.28994	3250	0.27084	3250	0.27027
4330	0.22645			4300	0.18612	4300	0.18519
5410	0.06316	5410	0.05136	5410	0.04719	5410	0.04304
G1X (mm)	G1Y	G2X (mm)	G2Y	G3X (mm)	G3Y	G4X (mm)	G4Y
0	0.08979	0	0.07291	0	0.06626	0	0.06001
1100	0.26210	1080	0.22421			1060	0.16846
2170	0.36334	2190	0.31639	2160	0.26999	2150	0.24099
3290	0.35220	3250	0.30359	3250	0.25708	3250	0.23967
4330	0.24407			4300	0.17899	4300	0.16233
5410	0.06745	5410	0.05335	5410	0.04323	5410	0.03521

Table C.12. Unit-norm mode shape for D6S0W1 from harmonic and impact excitation

D6S0W1

G1X (mm)	G1Y	G2X (mm)	G2Y	G3X (mm)	G3Y	G4X (mm)	G4Y
0	0.11194	0	0.09479	0	0.08763	0	0.07945
1100	0.25606	1080	0.22863			1060	0.19567
2170	0.33702	2190	0.30610	2160	0.27958	2150	0.27072
3290	0.32215	3250	0.28605	3250	0.26474	3250	0.26461
4330	0.22312			4300	0.18078	4300	0.17740
5410	0.06546	5410	0.05166	5410	0.04273	5410	0.03474
G1X (mm)	G1Y	G2X (mm)	G2Y	G3X (mm)	G3Y	G4X (mm)	G4Y
0	0.10844	0	0.09253	0	0.08291	0	0.07153
1100	0.26164	1080	0.23167			1060	0.18016
2170	0.35049	2190	0.31489	2160	0.27600	2150	0.25049
3290	0.33588	3250	0.29855	3250	0.26278	3250	0.24530
4330	0.23077			4300	0.17724	4300	0.16501
5410	0.06243	5410	0.05060	5410	0.04093	5410	0.03134

Table C.13. Unit-norm mode shape for D0S1W1 from harmonic and impact excitation

D0S1W1

G1X (mm)	G1Y	G2X (mm)	G2Y	G3X (mm)	G3Y	G4X (mm)	G4Y
0	0.07199	0	0.05945	0	0.06098	0	0.06166
1100	0.24218	1080	0.21301			1060	0.18969
2170	0.34068	2190	0.30549	2160	0.28383	2150	0.27443
3290	0.33538	3250	0.29452	3250	0.27450	3250	0.27092
4330	0.23103			4300	0.18592	4300	0.18282
5410	0.06184	5410	0.04915	5410	0.04216	5410	0.03390

G1X (mm)	G1Y	G2X (mm)	G2Y	G3X (mm)	G3Y	G4X (mm)	G4Y
0	0.06906	0	0.05804	0	0.05712	0	0.05699
1100	0.24591	1080	0.21751			1060	0.17965
2170	0.35012	2190	0.31702	2160	0.28118	2150	0.25879
3290	0.34451	3250	0.30449	3250	0.26729	3250	0.25502
4330	0.23571			4300	0.18441	4300	0.17416
5410	0.05892	5410	0.04857	5410	0.04018	5410	0.03080

Table C.14. Unit-norm mode shape for D4S1W1 from harmonic and impact excitation

D4S1W1

G1X (mm)	G1Y	G2X (mm)	G2Y	G3X (mm)	G3Y	G4X (mm)	G4Y
0	0.09704	0	0.08336	0	0.07978	0	0.07466
1100	0.23629	1080	0.21923			1060	0.20153
2170	0.31620	2190	0.30091	2160	0.28676	2150	0.28473
3290	0.30776	3250	0.28852	3250	0.27719	3250	0.28186
4330	0.21647			4300	0.19465	4300	0.19762
5410	0.07084	5410	0.06388	5410	0.05912	5410	0.05221

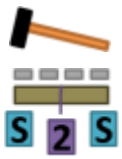

G1X (mm)	G1Y	G2X (mm)	G2Y	G3X (mm)	G3Y	G4X (mm)	G4Y
0	0.09300	0	0.08037	0	0.07449	0	0.06842
1100	0.23925	1080	0.22139			1060	0.19235
2170	0.32545	2190	0.30725	2160	0.28328	2150	0.27308
3290	0.31610	3250	0.29982	3250	0.27722	3250	0.27118
4330	0.22120			4300	0.19287	4300	0.19023
5410	0.06704	5410	0.06171	5410	0.05566	5410	0.04851

Table C.15. Unit-norm mode shape for D5S1W1 from harmonic and impact excitation

D5S1W1

G1X (mm)	G1Y	G2X (mm)	G2Y	G3X (mm)	G3Y	G4X (mm)	G4Y
0	0.09038	0	0.07433	0	0.07223	0	0.06978
1100	0.24905	1080	0.21844			1060	0.19094
2170	0.33852	2190	0.30344	2160	0.28141	2150	0.27298
3290	0.32901	3250	0.28994	3250	0.27084	3250	0.27027
4330	0.22645			4300	0.18612	4300	0.18519
5410	0.06316	5410	0.05136	5410	0.04719	5410	0.04304

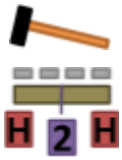

G1X (mm)	G1Y	G2X (mm)	G2Y	G3X (mm)	G3Y	G4X (mm)	G4Y
0	0.08789	0	0.07248	0	0.06743	0	0.06326
1100	0.25135	1080	0.22247			1060	0.18296
2170	0.34514	2190	0.31375	2160	0.28005	2150	0.26217
3290	0.33528	3250	0.29417	3250	0.26909	3250	0.26023
4330	0.22910			4300	0.18575	4300	0.17882
5410	0.05915	5410	0.05035	5410	0.04489	5410	0.03889

Table C.16. Unit-norm mode shape for D6S1W1 from harmonic and impact excitation

D6S1W1

G1X (mm)	G1Y	G2X (mm)	G2Y	G3X (mm)	G3Y	G4X (mm)	G4Y
0	0.11633	0	0.09526	0	0.08473	0	0.07485
1100	0.24016	1080	0.22463			1060	0.20960
2170	0.30443	2190	0.29806	2160	0.29409	2150	0.30021
3290	0.28664	3250	0.28040	3250	0.28077	3250	0.29759
4330	0.19144			4300	0.19321	4300	0.20646
5410	0.04680	5410	0.04714	5410	0.05020	5410	0.05183

G1X (mm)	G1Y	G2X (mm)	G2Y	G3X (mm)	G3Y	G4X (mm)	G4Y
0	0.10957	0	0.09139	0	0.07979	0	0.06992
1100	0.23789	1080	0.22543			1060	0.20484
2170	0.30762	2190	0.30363	2160	0.29285	2150	0.29561
3290	0.29351	3250	0.28804	3250	0.28088	3250	0.29313
4330	0.19486			4300	0.19355	4300	0.20272
5410	0.04443	5410	0.04590	5410	0.04752	5410	0.04746

Table C.17. Unit-norm mode shape for D0S2W1 from harmonic and impact excitation

D0S2W1

G1X (mm)	G1Y	G2X (mm)	G2Y	G3X (mm)	G3Y	G4X (mm)	G4Y
0	0.07738	0	0.06118	0	0.05760	0	0.05433
1100	0.25226	1080	0.21759			1060	0.17827
2170	0.35349	2190	0.31285	2160	0.27799	2150	0.26101
3290	0.34604	3250	0.30102	3250	0.26820	3250	0.25336
4330	0.23802			4300	0.18074	4300	0.16910
5410	0.06176	5410	0.04895	5410	0.03940	5410	0.02914

G1X (mm)	G1Y	G2X (mm)	G2Y	G3X (mm)	G3Y	G4X (mm)	G4Y
0	0.07634	0	0.05810	0	0.05258	0	0.04732
1100	0.26350	1080	0.21768			1060	0.16034
2170	0.37465	2190	0.31834	2160	0.26855	2150	0.23559
3290	0.36558	3250	0.30977	3250	0.26034	3250	0.22871
4330	0.25031			4300	0.17435	4300	0.15326
5410	0.05911	5410	0.04695	5410	0.03672	5410	0.02565

Table C.18. Unit-norm mode shape for D4S2W1 from harmonic and impact excitation

D4S2W1

G1X (mm)	G1Y	G2X (mm)	G2Y	G3X (mm)	G3Y	G4X (mm)	G4Y
0	0.10851	0	0.08854	0	0.07887	0	0.06853
1100	0.24432	1080	0.22244			1060	0.19859
2170	0.31937	2190	0.30121	2160	0.28682	2150	0.28564
3290	0.30747	3250	0.28766	3250	0.27566	3250	0.27921
4330	0.21310			4300	0.19151	4300	0.19417
5410	0.06463	5410	0.05899	5410	0.05550	5410	0.05020

G1X (mm)	G1Y	G2X (mm)	G2Y	G3X (mm)	G3Y	G4X (mm)	G4Y
0	0.10696	0	0.08751	0	0.07428	0	0.06124
1100	0.25274	1080	0.22716			1060	0.18351
2170	0.33539	2190	0.31148	2160	0.28180	2150	0.26335
3290	0.32341	3250	0.29979	3250	0.26675	3250	0.26197
4330	0.22256			4300	0.18764	4300	0.18125
5410	0.06357	5410	0.05854	5410	0.05325	5410	0.04541

Table C.19. Unit-norm mode shape for D5S2W1 from harmonic and impact excitation

D5S2W1

G1X (mm)	G1Y	G2X (mm)	G2Y	G3X (mm)	G3Y	G4X (mm)	G4Y
0	0.09629	0	0.07805	0	0.07374	0	0.06875
1100	0.26721	1080	0.22469			1060	0.17153
2170	0.36504	2190	0.31242	2160	0.26915	2150	0.24010
3290	0.35480	3250	0.29807	3250	0.25803	3250	0.23201
4330	0.24713			4300	0.17428	4300	0.15555
5410	0.07286	5410	0.05534	5410	0.04400	5410	0.03357

G1X (mm)	G1Y	G2X (mm)	G2Y	G3X (mm)	G3Y	G4X (mm)	G4Y
0	0.09397	0	0.07609	0	0.06892	0	0.06056
1100	0.27042	1080	0.22855			1060	0.15899
2170	0.37448	2190	0.32205	2160	0.26433	2150	0.22601
3290	0.36171	3250	0.31242	3250	0.24577	3250	0.21809
4330	0.25167			4300	0.17273	4300	0.14651
5410	0.06894	5410	0.05406	5410	0.04176	5410	0.03101

Table C.20. Unit-norm mode shape for D6S2W1 from harmonic and impact excitation

D6S2W1

G1X (mm)	G1Y	G2X (mm)	G2Y	G3X (mm)	G3Y	G4X (mm)	G4Y
0	0.11336	0	0.09258	0	0.08221	0	0.07206
1100	0.24671	1080	0.22595			1060	0.20319
2170	0.31871	2190	0.30279	2160	0.28909	2150	0.29044
3290	0.30348	3250	0.28636	3250	0.27497	3250	0.28078
4330	0.20660			4300	0.18718	4300	0.19092
5410	0.05630	5410	0.04999	5410	0.04620	5410	0.04143

G1X (mm)	G1Y	G2X (mm)	G2Y	G3X (mm)	G3Y	G4X (mm)	G4Y
0	0.10990	0	0.08982	0	0.07698	0	0.06520
1100	0.25193	1080	0.22818			1060	0.19166
2170	0.33117	2190	0.31098	2160	0.28534	2150	0.27454
3290	0.31572	3250	0.29560	3250	0.27055	3250	0.26766
4330	0.21495			4300	0.18515	4300	0.18163
5410	0.05564	5410	0.04946	5410	0.04383	5410	0.03744

APPENDIX D. MODE SHAPE COMPONENTS

In this appendix, the average mode shape component values are listed in the tables. The figures are plotted in the same manner as the bar chart described in Figure 4.20. The results from harmonic excitation and impact excitation are both presented in this appendix.

It should be noted, that in cases with negative differential substructure movement (where the right support had a greater amplitude than the left support), the average mode shape components (A, B and C) were scaled to add to unity.

Table D.1. Summary of average mode shape components from harmonic excitation

Damage Case	Mode Shape Component (Harmonic) A	B	C
 D0S0W1$_a$	0.73390	0.04564	0.22046
 D1S0W1	0.71215	0.08287	0.20499
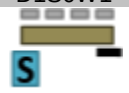 D2S0W1	0.65496	0.15115	0.19388
 D3S0W1	0.69354	0.08284	0.22362
 D0S0W1$_b$	0.74175	0.02947	0.22878
 D0S0W2	0.74056	0.03372	0.22572
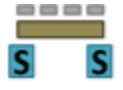 D4S0W1$_a$	0.65167	0.08494	0.26340
 D4S0W2	0.67350	0.07860	0.24790

Damage Case	Mode Shape Component (Harmonic) A	B	C
 D0S0W1$_c$	0.74153	0.04103	0.21744
 D4S0W1$_b$	0.67195	0.05848	0.26957
 D5S0W1	0.70588	0.05657	0.23755
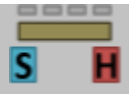 D6S0W1	0.67669	0.10335	0.21996
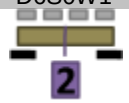 D0S1W1	0.74683	0.04009	0.21308
 D4S1W1	0.67069	0.05038	0.27893
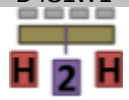 D5S1W1	0.70758	0.05882	0.23361
 D6S1W1	0.67704	0.09943	0.22352
 D0S2W1	0.75329	0.04291	0.20380
 D4S2W1	0.67477	0.06457	0.26066
 D5S2W1	0.69866	0.06780	0.23354
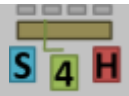 D6S2W1	0.68528	0.09402	0.22070

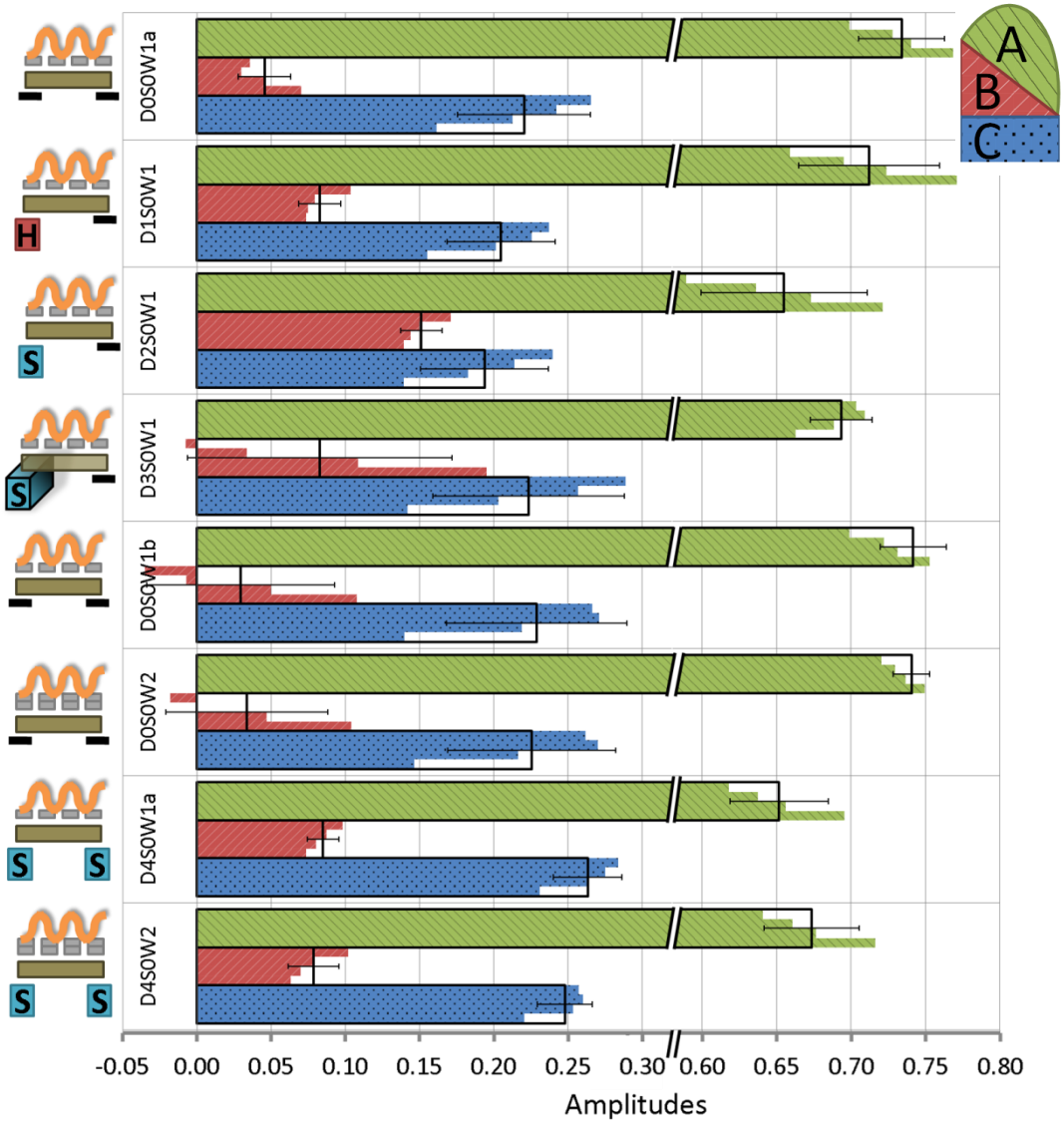

Figure D.1. Mode shape component amplitudes from harmonic excitation I

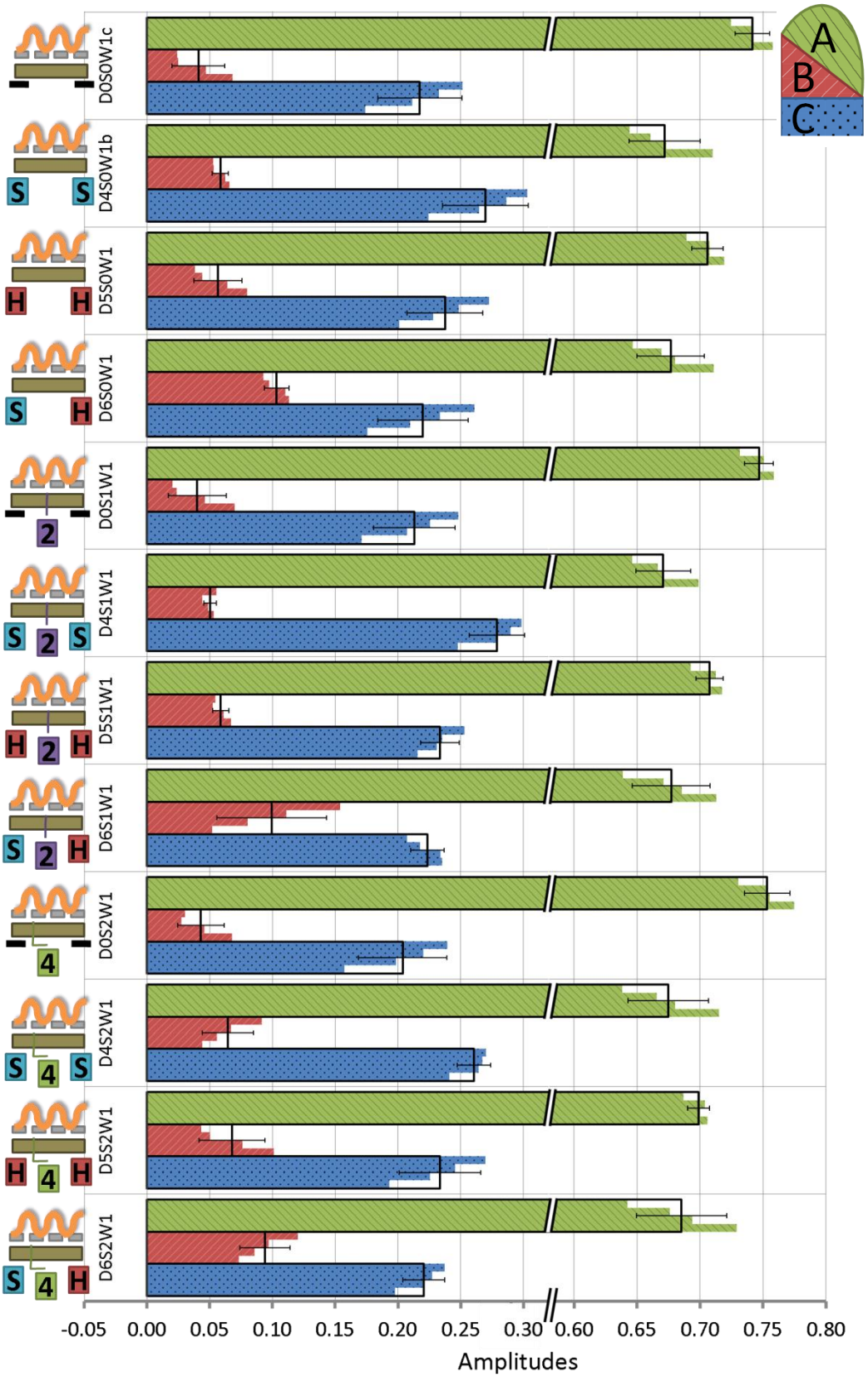

Figure D.2. Mode shape component amplitudes from harmonic excitation II

Table D.2. Summary of average mode shape components from impact excitation

Damage Case	Mode Shape Component (Impact) A	B	C
 D0S0W1$_a$	0.74135	0.04655	0.21210
 D1S0W1	0.72447	0.07809	0.19744
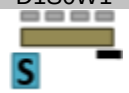 D2S0W1	0.67296	0.14033	0.18672
 D3S0W1	0.70700	0.07949	0.21351
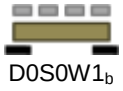 D0S0W1$_b$	0.74531	0.03078	0.22391
 D0S0W2	0.74342	0.03941	0.21717
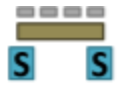 D4S0W1$_a$	0.66522	0.08011	0.25467
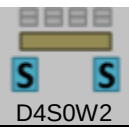 D4S0W2	0.68493	0.07373	0.24133

Damage Case	Mode Shape Component (Impact) A	B	C
 D0S0W1$_c$	0.75414	0.03952	0.20634
 D4S0W1$_b$	0.68679	0.05445	0.25877
 D5S0W1	0.71892	0.05362	0.22746
 D6S0W1	0.69120	0.09895	0.20985
 D0S1W1	0.75823	0.03834	0.20344
 D4S1W1	0.68810	0.04737	0.26453
 D5S1W1	0.72218	0.05648	0.22133
 D6S1W1	0.69468	0.09360	0.21172
 D0S2W1	0.76644	0.04069	0.19286
 D4S2W1	0.68769	0.06069	0.25162
 D5S2W1	0.71294	0.06375	0.22331
 D6S2W1	0.70003	0.08776	0.21221

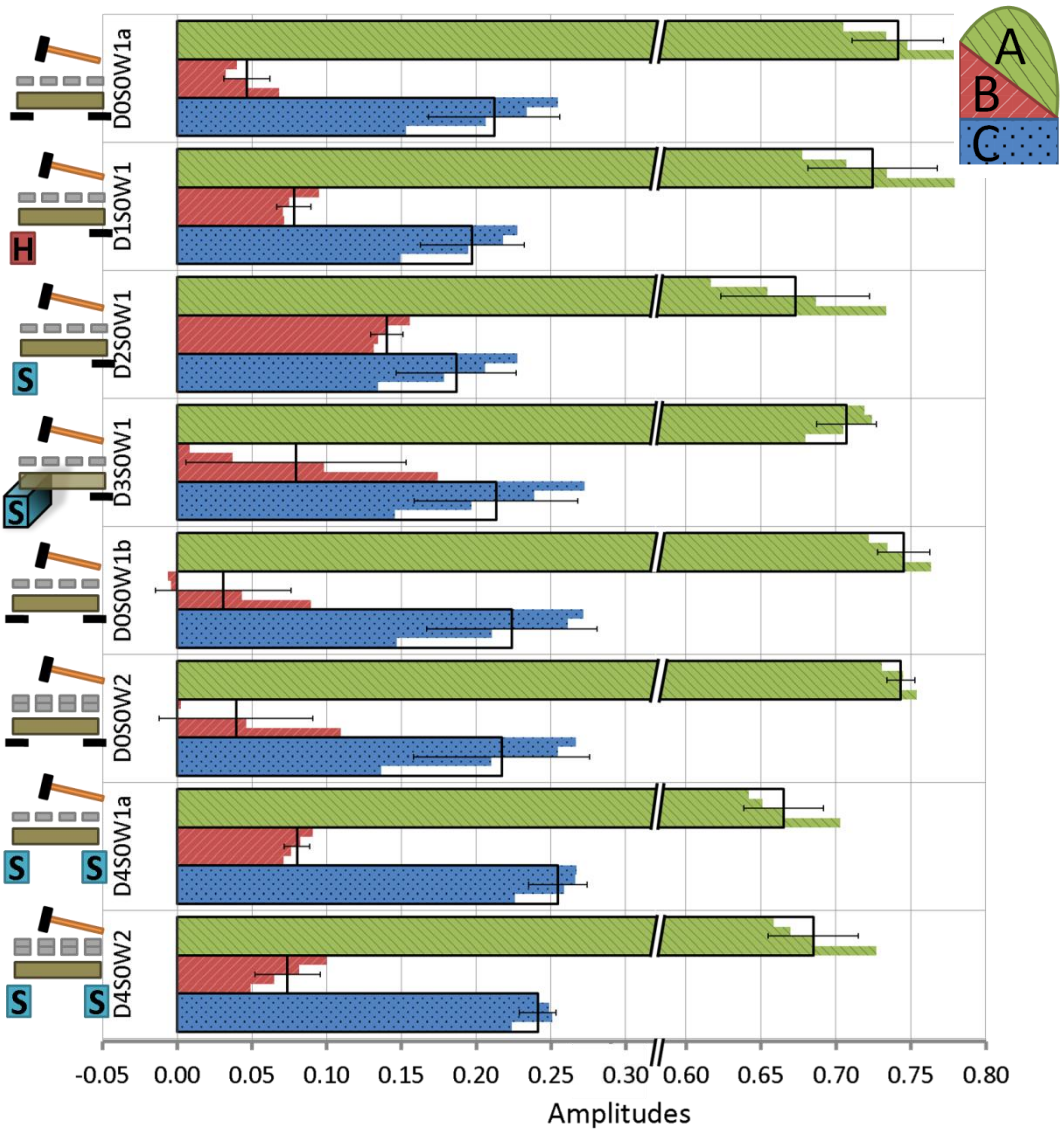

Figure D.3. Mode shape component amplitudes from impact excitation I

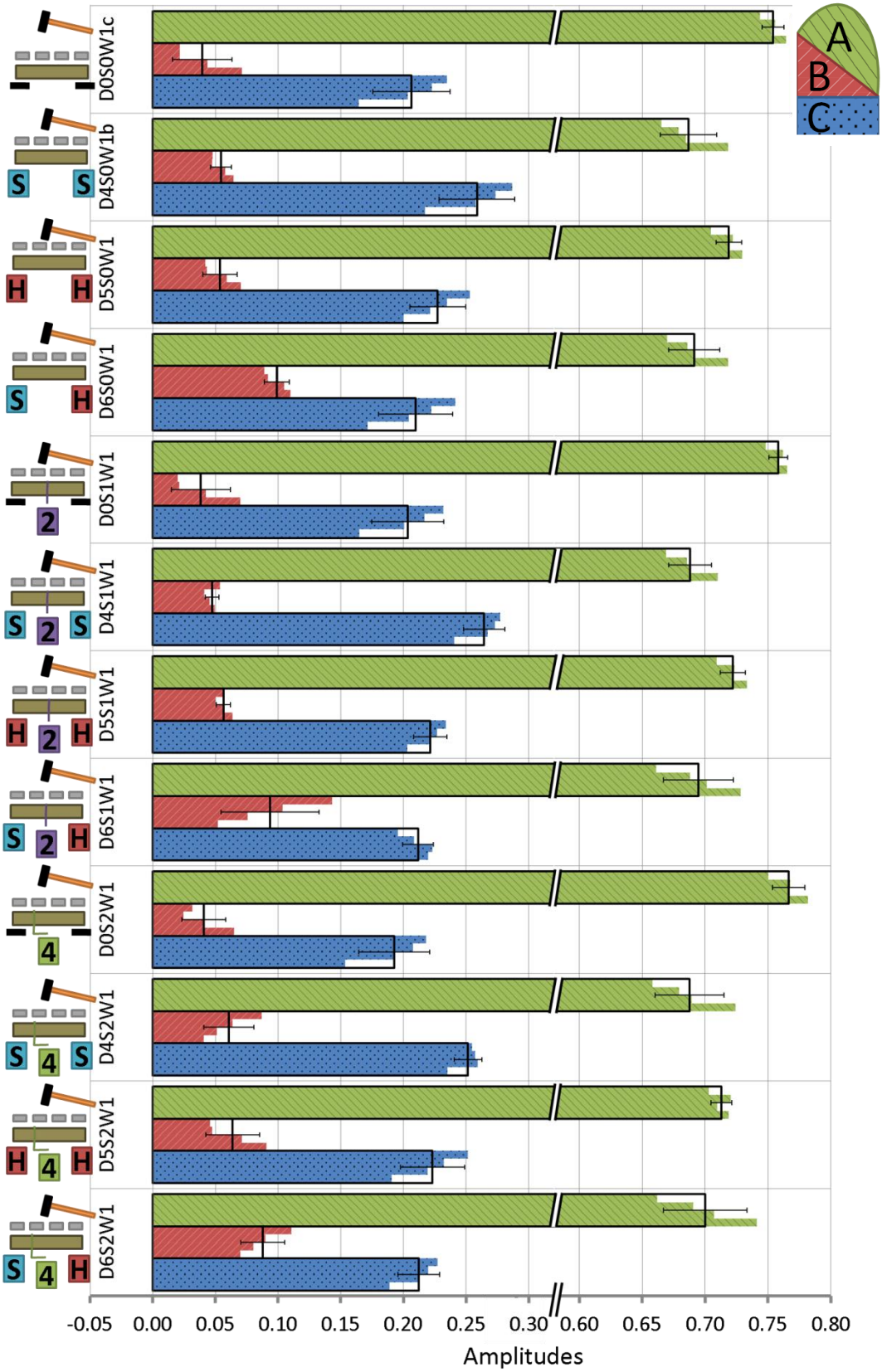

Figure D.4. Mode shape component amplitudes from impact excitation II

APPENDIX E. NATURAL FREQUENCIES

This appendix lists all the fundamental natural frequencies for the bridge states considered in this thesis. Table E.1 lists the natural frequencies produced using harmonic excitation, as well as impact loading. As stated in Section 3.5.2, harmonic excitation produced more precise results (±0.05 Hz) than impact loading (±0.12 Hz).

Table E.1. Summary of all natural frequencies for timber bridge condition states

Damage Case	Natural frequency (Hz) Harmonic ±0.05Hz	Natural frequency (Hz) Impact ±0.12Hz
 D0S0W1$_a$	15.91	15.99
 D1S0W1	15.82	15.99
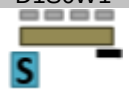 D2S0W1	15.33	15.50
 D3S0W1	15.65	15.87
 D0S0W1$_b$	15.85	16.08
 D0S0W2	15.02	15.30
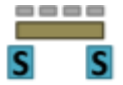 D4S0W1$_a$	15.22	15.45
 D4S0W2	14.61	14.77

Damage Case	Natural frequency (Hz) Harmonic ±0.05Hz	Natural frequency (Hz) Impact ±0.12Hz
 D0S0W1$_c$	16.00	16.24
 D4S0W1$_b$	15.44	15.63
 D5S0W1	15.77	15.99
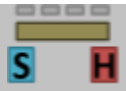 D6S0W1	15.44	15.69
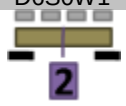 D0S1W1	15.97	16.11
 D4S1W1	15.24	15.50
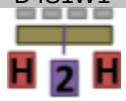 D5S1W1	15.60	15.76
 D6S1W1	15.26	15.50
 D0S2W1	15.96	16.11
 D4S2W1	15.22	15.38
 D5S2W1	15.46	15.75
 D6S2W1	15.35	15.50

APPENDIX F. VIBRATION-BASED DAMAGE DETECTION

The figures in this appendix include all the plots comparing an undamaged superstructure bridge state to a damaged superstructure bridge state by considering change in mode shape and change in curvature. Additionally, the figures consider a full range of substructure states. In general, the substructure condition state had little effect in the ability to detect superstructure damage. This conclusion is especially evident when considering damage to Girder 4 (Figure F.9 to F.16).

Additionally, Table F.1 and Table F.2 provide the data used to establish the threshold explained in Section 4.6.3 (Figure 4.34 Figure 4.35). In these tables, the mean and standard deviation of the area under the change in mode shape vector (and area under the change in curvature vector) were used when considering similar superstructure bridge states to establish a threshold using a normal distribution (Z=3).

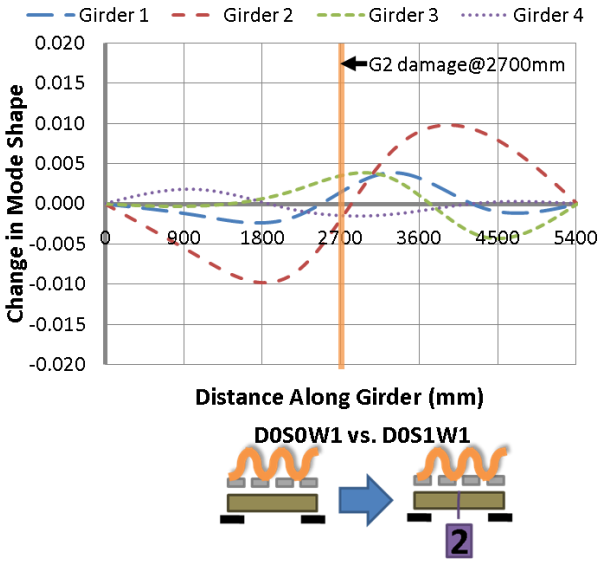

Figure F.1. Change in mode shape - $D0S0W1_c$ vs. D0S1W1 (harmonic)

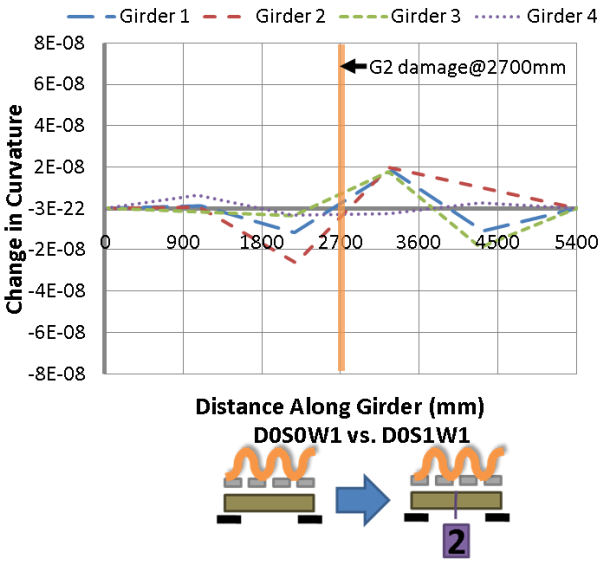

Figure F.2. Change in curvature – $D0S0W1_c$ vs. D0S1W1 (harmonic)

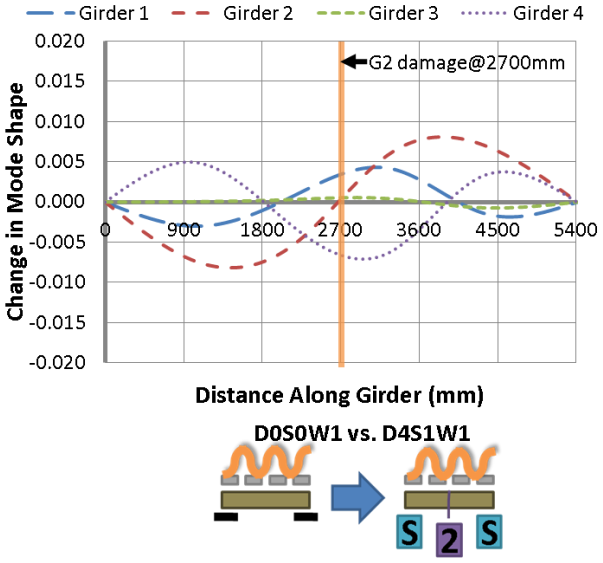

Figure F.3. Change in mode shape - $D0S0W1_c$ vs. D4S1W1 (harmonic)

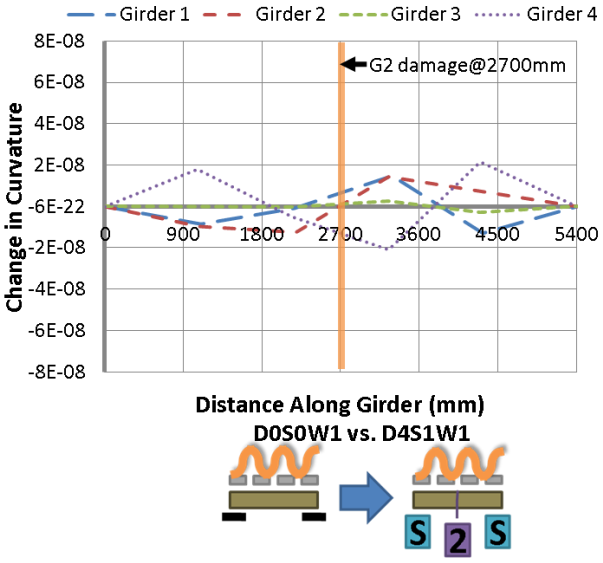

Figure F.4. Change in curvature – $D0S0W1_c$ vs. D4S1W1 (harmonic)

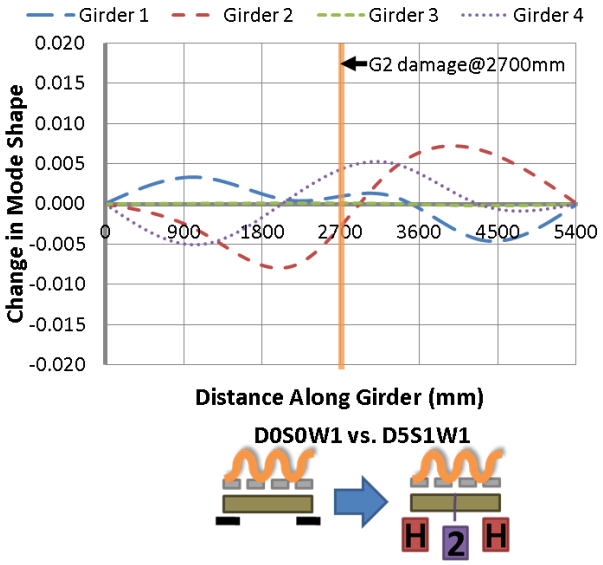

Figure F.5. Change in mode shape - D0S0W1$_c$ vs. D5S1W1 (harmonic)

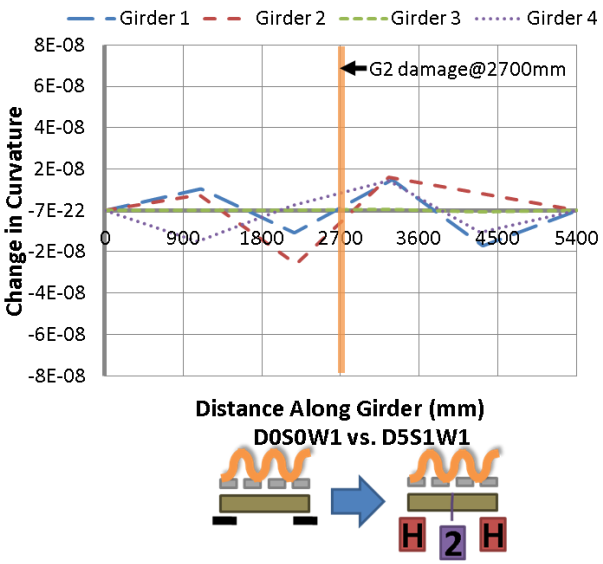

Figure F.6. Change in curvature – D0S0W1$_c$ vs. D5S1W1 (harmonic)

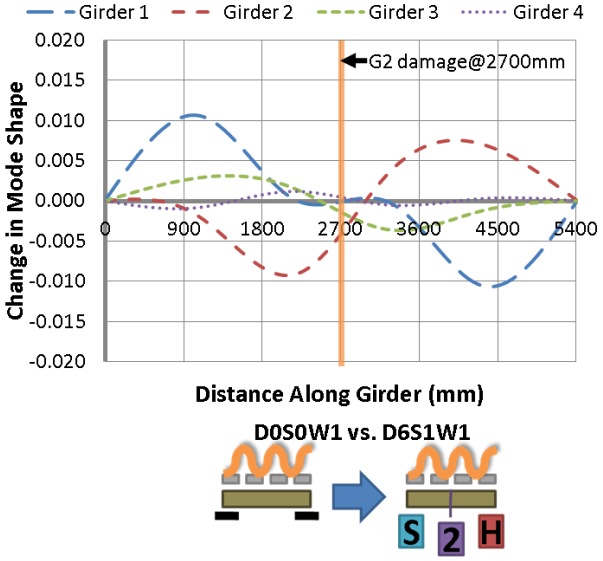

Figure F.7. Change in mode shape - D0S0W1$_c$ vs. D6S1W1 (harmonic)

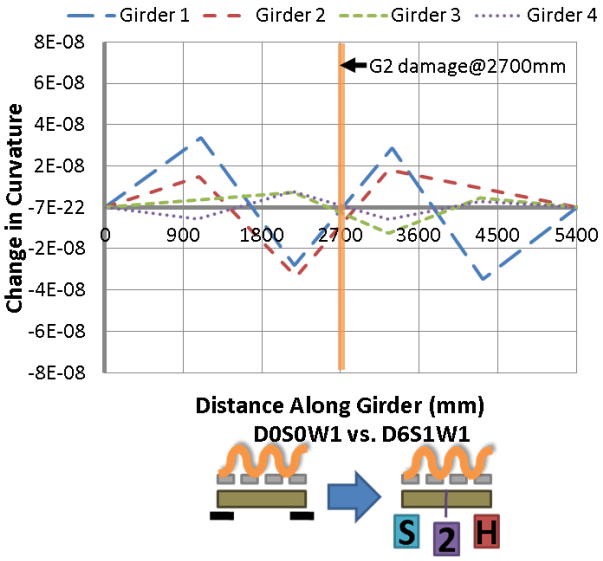

Figure F.8. Change in curvature – D0S0W1$_c$ vs. D6S1W1 (harmonic)

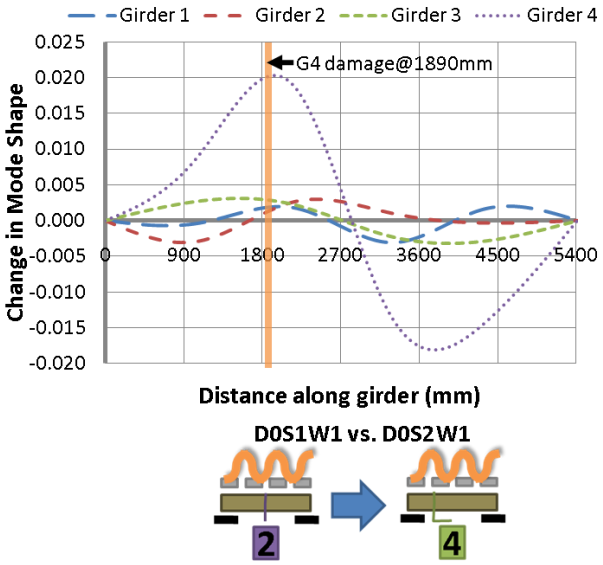

Figure F.9. Change in mode shape - D0S1W1 vs. D0S2W1 (harmonic)

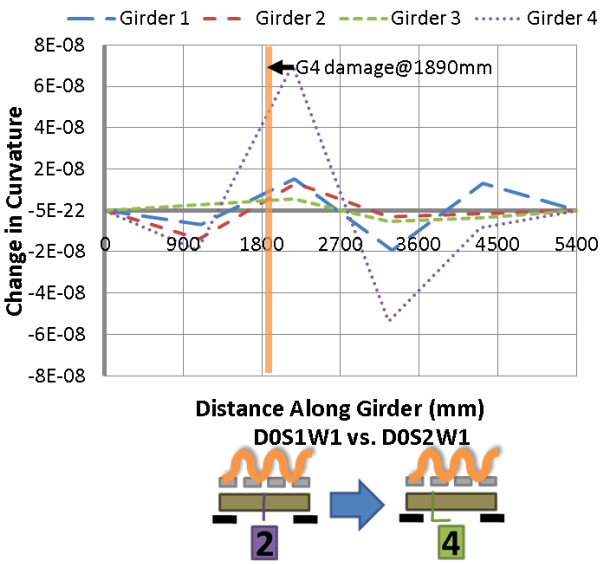

Figure F.10. Change in curvature – D0S1W1 vs. D0S2W1 (harmonic)

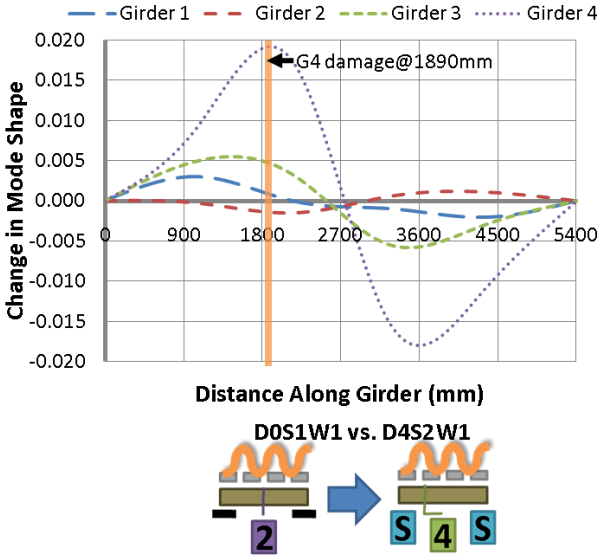

Figure F.11. Change in mode shape - D0S1W1 vs. D4S2W1 (harmonic)

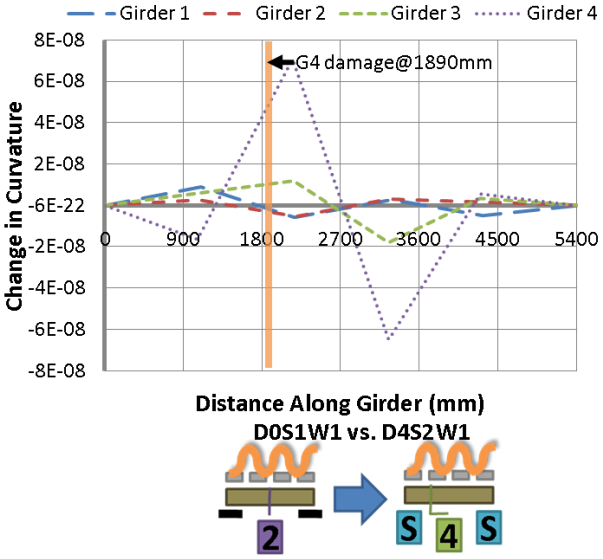

Figure F.12. Change in curvature – D0S1W1 vs. D4S2W1 (harmonic)

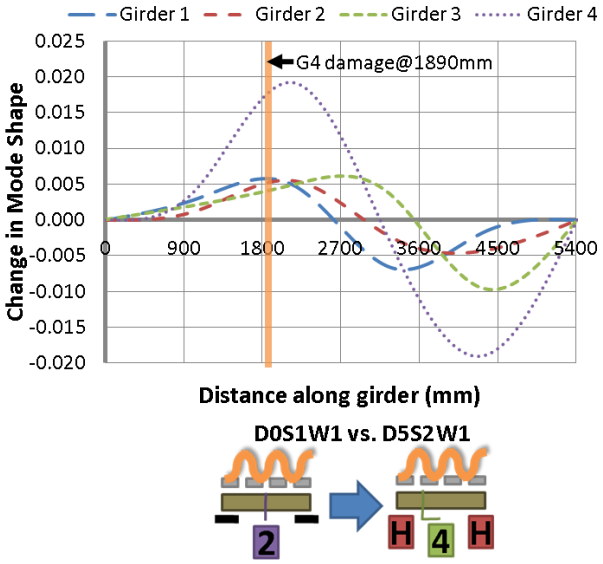

Figure F.13. Change in mode shape - D0S1W1 vs. D5S2W1 (harmonic)

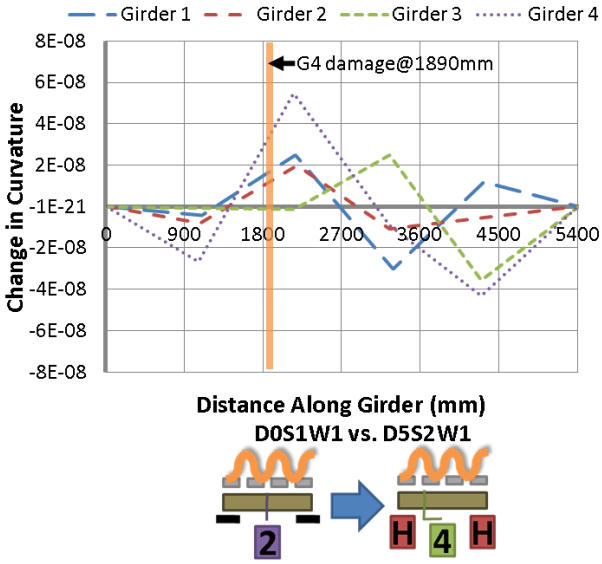

Figure F.14. Change in curvature – D0S1W1 vs. D5S2W1 (harmonic)

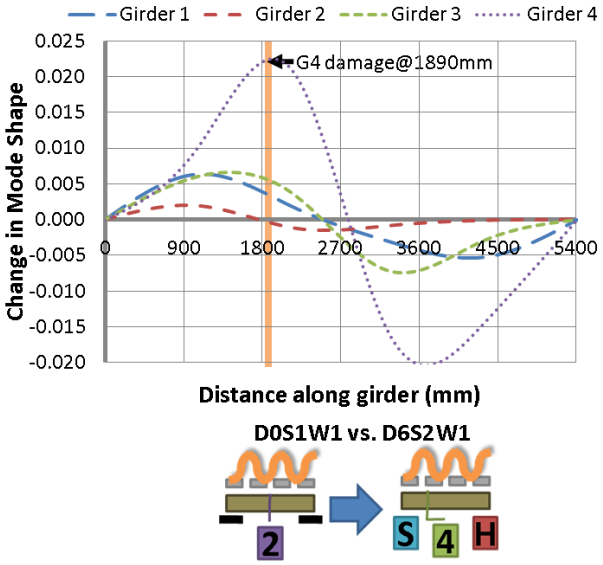

Figure F.15. Change in mode shape - D0S1W1 vs. D6S2W1 (harmonic)

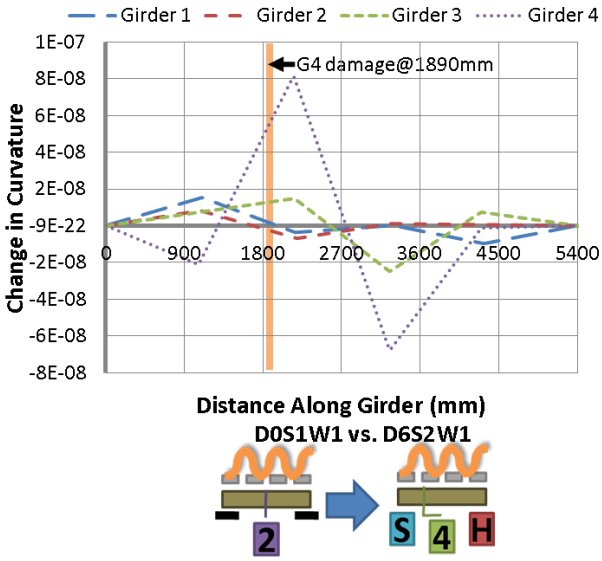

Figure F.16. Change in curvature – D0S1W1 vs. D6S2W1 (harmonic)

Table F.1. Area under the change in mode shape plots when comparing similar superstructure states to establish a threshold

Bridge States	Girder 1	Girder 2	Girder 3	Girder 4
D0S0W1 vs. D4S0W1	0.0008	0.0018	0.0039	0.0021
D0S0W1 vs. D5S0W1	0.0017	0.0028	0.0030	0.0065
D0S0W1 vs. D6S0W1	0.0023	0.0035	0.0023	0.0021
D0S1W1 vs. D4S1W1	0.0011	0.0014	0.0015	0.0026
D0S1W1 vs. D5S1W1	0.0028	0.0018	0.0017	0.0035
D0S1W1 vs. D6S1W1	0.0062	0.0021	0.0029	0.0011

Average	St. Dev.	α	Z (norm dist.)	**Threshold**
0.0026	1.4E-03	0.0013	3.0	**0.0068**

Table F.2. Area under the change in curvature plots when comparing similar superstructure states to establish a threshold

Bridge States	Girder 1	Girder 2	Girder 3	Girder 4
D0S0W1 vs. D4S0W1	3.51E-09	5.61E-09	1.13E-08	7.12E-09
D0S0W1 vs. D5S0W1	4.24E-09	4.27E-09	7.71E-09	2.39E-08
D0S0W1 vs. D6S0W1	7.94E-09	6.06E-09	8.07E-09	1.14E-08
D0S1W1 vs. D4S1W1	3.63E-09	4.51E-09	5.13E-09	7.90E-09
D0S1W1 vs. D5S1W1	3.76E-09	2.48E-09	5.86E-09	9.04E-09
D0S1W1 vs. D6S1W1	1.17E-08	3.83E-09	9.73E-09	3.58E-09

Average	St. Dev.	α	Z (norm dist.)	**Threshold**
7.18E-09	4.49E-09	0.0013	3	**2.06E-08**

APPENDIX G. STATISTICAL ANALYSIS

The statistical analysis was completed using Microsoft Excel 2007 with a two-sample t-test assuming unequal variance (heteroscedastic t-test). The heteroscedastic t-test was selected because of the distinct nature of the bridge cases considered; the superstructure and substructure were both changing. In addition, the heteroscedastic t-test accounts for unequal variances, which was observed throughout testing.

The two-sample F-test on variance was used to assess whether two bridge states had equal variances by considering mode shape components. This test considered a two-tailed probability with a hypothesis that the variances were not significantly different.

The means and standard deviations used to produce Tables G.1 to G.8 and G.10 are presented in Table 5.1 Table 5.2 (for impact loadings). Table G.9 did not consider individual girder responses and used the average mode shape components over the four girders to describe a single bridge state. Other similar substructure condition states were used to acquire a mean and standard deviation as indicated below:

- D0 (rigid-rigid)→ D0S0W1$_c$, D0S1W1, and D0S2W1
- D4 (soft-soft)→ D4S0W1$_b$, D4S1W1, and D4S2W1
- D5 (hard-hard)→ D5S0W1, D5S1W1, and D5S2W1
- D6 (soft-hard)→ D6S0W1, D6S1W1, and D6S2W1

i. Detection of Substructure Damage to a Single Support

Table G.1. T-test results considering bridge states with varying substructure stiffness under a single support

H_0: There is no difference in foundation stiffness
H_1: There is a difference in foundation stiffness (**if p<0.1, reject H_0**)

Bridge State		P-Values (damage to a single support)			
Impact / Harmonic		D0S0W1$_{(a)}$	D1S0W1	D2S0W1	D3S0W1
D0S0W1$_{(a)}$	A	1	0.550	**0.066**	0.117
	B		**0.019**	**0.000**	0.441
	C		0.621	0.427	0.969
D1S0W1	A	0.468	1	0.169	0.501
	B	**0.018**		**0.000**	0.972
	C	0.611		0.701	0.641
D2S0W1	A	**0.059**	0.171	1	0.273
	B	**0.000**	**0.000**		0.197
	C	0.425	0.707		0.462
D3S0W1	A	**0.057**	0.457	0.297	1
	B	0.472	0.995	0.222	
	C	0.955	0.652	0.488	

Excel function:

=ttest(array1,array2, 2 tails, heteroscedastic t-test)

- array1 → Girder 1; Girder 2; Girder 3; Girder 4
  - Bridge state 1 using mode shape component (A,B or C)
- array2 → Girder 1; Girder 2; Girder 3; Girder 4
  - Bridge state 2 using mode shape component (A,B or C)

ii. Detection of Local Substructure Damage

Table G.2. F-test on variance results considering bridge states with varying substructure stiffness under a single support

H_0: Both foundations have a uniform stiffness
H_1: One of the foundations has a non-uniform stiffness (**if p<0.1, reject H_0**)

Bridge State		P-Values (damage to a single support)			
Impact / Harmonic		D0S0W1(a)	D1S0W1	D2S0W1	D3S0W1
D0S0W1(a)	A	1	0.586	0.449	0.503
	B		0.636	0.568	**0.029**
	C		0.710	0.883	0.729
D1S0W1	A	0.440	1	0.826	0.238
	B	0.715		0.921	**0.012**
	C	0.736		0.822	0.477
D2S0W1	A	0.308	0.791	1	0.170
	B	0.702	0.986		**0.010**
	C	0.951	0.783		0.623
D3S0W1	A	0.602	0.210	0.139	1
	B	**0.025**	**0.013**	**0.012**	
	C	0.566	0.370	0.526	

Excel function:

=ftest(array1,array2)

- array1 → Girder 1; Girder 2; Girder 3; Girder 4
  - Bridge state 1 using mode shape component (A,B or C)
- array2 → Girder 1; Girder 2; Girder 3; Girder 4
  - Bridge state 2 using mode shape component (A,B or C)

iii. Substructure Damage Detection on Both Supports

Table G.3. T-test results considering bridge states with varying substructure stiffness under both supports

H_0: There is no difference in foundation stiffness
H_1: There is a difference in foundation stiffness (**if p<0.1, reject H_0**)

Bridge State		P-Values (damage to both supports)			
Impact / Harmonic		D0S0W1(c)	D4S0W1(b)	D5S0W1	D6S0W1
D0S0W1(c)	A	1	**0.006**	**0.002**	**0.004**
	B		0.302	0.350	**0.009**
	C		**0.051**	0.314	0.875
D4S0W1(b)	A	**0.009**	1	**0.057**	0.781
	B	0.196		0.921	**0.001**
	C	**0.071**		0.150	**0.060**
D5S0W1	A	**0.009**	**0.090**	1	**0.065**
	B	0.315	0.859		**0.002**
	C	0.407	0.211		0.383
D6S0W1	A	**0.010**	0.816	0.116	1
	B	**0.005**	**0.001**	**0.009**	
	C	0.922	**0.093**	0.485	

Excel function:

=ttest(array1,array2, 2 tails, heteroscedastic t-test)

- array1 → Girder 1; Girder 2; Girder 3; Girder 4
  - Bridge state 1 using mode shape component (A,B or C)
- array2 → Girder 1; Girder 2; Girder 3; Girder 4
  - Bridge state 2 using mode shape component (A,B or C)

iv. Influence of Superimposed mass

Table G.4. T-test results considering bridge states with varying substructure stiffness and superimposed mass

H_0: There is no difference in foundation stiffness
H_1: There is a difference in foundation stiffness (**if p<0.1, reject H_0**)

Bridge State		P-Values (influence of superimposed mass)			
Impact / Harmonic		D0S0W1(b)	D0S0W2	D4S0W1(a)	D4S0W2
D0S0W1(b)	A	1	0.868	**0.005**	**0.024**
	B		0.807	0.116	0.157
	C		0.895	0.355	0.567
D0S0W2	A	0.567	1	**0.006**	**0.025**
	B	0.917		0.211	0.286
	C	0.995		0.299	0.476
D4S0W1(a)	A	**0.012**	**0.011**	1	0.365
	B	0.174	0.154		0.617
	C	0.294	0.265		0.298
D4S0W2	A	**0.040**	**0.026**	0.379	1
	B	0.215	0.197	0.554	
	C	0.498	0.467	0.337	

Excel function:

=ttest(array1,array2, 2 tails, heteroscedastic t-test)

- array1 → Girder 1; Girder 2; Girder 3; Girder 4
  - Bridge state 1 using mode shape component (A,B or C)
- array2 → Girder 1; Girder 2; Girder 3; Girder 4
  - Bridge state 2 using mode shape component (A,B or C)

v. Superstructure Damage Detection

Table G.5. T-test results considering bridge states with similar substructure stiffness (D0) and varying superstructure states

H_0: There is no difference in foundation stiffness
H_1: There is a difference in foundation stiffness (**if p<0.1, reject H_0**)

Bridge State		P-Values		
Impact / Harmonic		D0S0W1(c)	D0S1W1	D0S2W1
D0S0W1(c)	A	1	0.499	0.171
	B		0.945	0.939
	C		0.895	0.544
D0S1W1	A	0.574	1	0.321
	B	0.954		0.878
	C	0.858		0.619
D0S2W1	A	0.344	0.572	1
	B	0.898	0.856	
	C	0.594	0.712	

Table G.6. T-test results considering bridge states with similar substructure stiffness (D4) and varying superstructure states

H_0: There is no difference in foundation stiffness
H_1: There is a difference in foundation stiffness (**if p<0.1, reject H_0**)

Bridge State		P-Values		
Impact / Harmonic		D4S0W1(b)	D4S1W1	D4S2W1
D4S0W1(b)	A	1	0.929	0.961
	B		0.205	0.592
	C		0.752	0.681
D4S1W1	A	0.946	1	0.981
	B	**0.096**		0.275
	C	0.664		0.251
D4S2W1	A	0.899	0.841	1
	B	0.602	0.260	
	C	0.652	0.217	

Table G.7. T-test results considering bridge states with similar substructure stiffness (D5) and varying superstructure states

H_0: There is no difference in foundation stiffness H_1: There is a difference in foundation stiffness (**if p<0.1, reject H_0**)				
Bridge State		P-Values		
Impact / Harmonic		D5S0W1	D5S1W1	D5S2W1
D5S0W1	A	1	0.665	0.399
	B		0.718	0.462
	C		0.658	0.815
D5S1W1	A	0.844	1	0.202
	B	0.835		0.555
	C	0.827		0.897
D5S2W1	A	0.382	0.247	1
	B	0.517	0.551	
	C	0.863	0.997	

Table G.8. T-test results considering bridge states with similar substructure stiffness (D0) and varying superstructure states

H_0: There is no difference in foundation stiffness H_1: There is a difference in foundation stiffness (**if p<0.1, reject H_0**)				
Bridge State		P-Values		
Impact / Harmonic		D6S0W1	D6S1W1	D6S2W1
D6S0W1	A	1	0.848	0.668
	B		0.807	0.317
	C		0.913	0.895
D6S1W1	A	0.987	1	0.813
	B	0.871		0.798
	C	0.863		0.964
D6S2W1	A	0.717	0.740	1
	B	0.446	0.832	
	C	0.972	0.801	

For Table G.5 to G.8 the Excel function used was the same as previous student's t-tests.

Since the above four tables show no significant difference between superstructure states, the mode shape components from the four girders were averaged together. The following table compares substructure response, while using the average girder response to produce three similar substructure states.

Table G.9. T-test results considering bridge states with varying substructure stiffness and varying superstructure states

H_0: There is no difference in foundation stiffness
H_1: There is a difference in foundation stiffness (**if p<0.1, reject H_0**)

Bridge State		P-Values (damage to both supports)			
Impact / Harmonic		D0W1 S0/S1/S2	D4W1 S0/S1/S2	D5W1 S0/S1/S2	D6W1 S0/S1/S2
D0W1 S0/S1/S2	Avg A	1	**0.002**	**0.001**	**0.000**
	Avg B		**0.058**	**0.021**	**0.003**
	Avg C		**0.001**	**0.017**	0.123
D4W1 S0/S1/S2	Avg A	**0.001**	1	**0.007**	**0.091**
	Avg B	**0.052**		0.485	**0.002**
	Avg C	**0.001**		**0.004**	**0.005**
D5W1 S0/S1/S2	Avg A	**0.001**	**0.003**	1	**0.004**
	Avg B	**0.024**	0.577		**0.001**
	Avg C	**0.020**	**0.017**		**0.011**
D6W1 S0/S1/S2	Avg A	**0.000**	0.109	**0.003**	1
	Avg B	**0.001**	**0.002**	**0.001**	
	Avg C	0.123	**0.009**	**0.002**	

Excel function:

=ttest(array1,array2, 2 tails, heteroscedastic t-test)

- array1 → S0;S1;S2
  - Bridge state 1 using averaged mode shape component (A,B or C) of the four girders
- array2 → S0;S1;S2
  - Bridge state 2 using averaged mode shape component (A,B or C) of the four girders

vi. Practical Application

Table G.10. T-test results considering bridge states with varying substructure stiffness under a single support using the limited accelerometer configuration

H_0: There is no difference in foundation stiffness
H_1: There is a difference in foundation stiffness (**if p<0.1, reject H_0**)

		P-Values (for reduced sensors)			
Impact / Harmonic		D0S0W1(a)	D1S0W1	D2S0W1	D3S0W1
D0S0W1(a)	A	1	0.570	**0.068**	0.129
	B		**0.017**	**0.000**	0.441
	C		0.616	0.408	0.985
D1S0W1	A	N/A	1	0.177	0.528
	B			**0.000**	0.992
	C			0.683	0.656
D2S0W1	A	N/A	N/A	1	0.260
	B				0.184
	C				0.464
D3S0W1	A	N/A	N/A	N/A	1
	B				
	C				

Excel function:

=ttest(array1,array2, 2 tails, heteroscedastic t-test)

- array1 → Girder 1; Girder 2; Girder 3; Girder 4
  - Bridge state 1 using mode shape component (A,B or C)
- array2 → Girder 1; Girder 2; Girder 3; Girder 4
  - Bridge state 2 using mode shape component (A,B or C)